THE EFFECT OF GEOMETRY AND SURFACE MORPHOLOGY ON THE OPTICAL PROPERTIES OF METAL-DIELECTRIC SYSTEMS

by

KEISUKE HASEGAWA

A DISSERTATION

Presented to the Department of Physics
and the Graduate School of the University of Oregon
in partial fulfillment of the requirements
for the degree of
Doctor of Philosophy

September 2008

University of Oregon Graduate School

Confirmation of Approval and Acceptance of Dissertation prepared by:

Keisuke Hasegawa

Title:

"The Effect of Geometry and Surface Morphology on the Optical Properties of Metal-Dielectric Systems"

This dissertation has been accepted and approved in partial fulfillment of the requirements for the Doctor of Philosophy degree in the Department of Physics by:

Hailin Wang, Chairperson, Physics
Miriam Deutsch, Advisor, Physics
Jens Noeckel, Member, Physics
John Toner, Member, Physics
Mark Lonergan, Outside Member, Chemistry

and Richard Linton, Vice President for Research and Graduate Studies/Dean of the Graduate School for the University of Oregon.

September 6, 2008

Original approval signatures are on file with the Graduate School and the University of Oregon Libraries.

An Abstract of the Dissertation of

Keisuke Hasegawa for the degree of Doctor of Philosophy

in the Department of Physics to be taken September 2008

Title: THE EFFECT OF GEOMETRY AND SURFACE MORPHOLOGY ON THE OPTICAL PROPERTIES OF METAL-DIELECTRIC SYSTEMS

Approved: _____

Dr. Miriam Deutsch

We analyze the effect of geometry and surface morphology on the optical properties of metal-dielectric systems. Using both analytical and numerical modeling, we study how surface curvature affects the propagation of surface plasmon polaritons (SPPs) along a metal-dielectric interface. We provide an intuitive explanation for how the curvature causes the phase front to distort, causing the SPPs to radiate their energy away from the metal-dielectric interface. We quantify the propagation efficiency as functions of the radius of curvature, and show that it depends nonmonotonically on the bend radius. We also show how the surface morphology influences the transmittance and the reflectance of light from disordered metal-dielectric nanocomposite films. The films consist of semicontinuous silver films of

various surface coverage that are chemically deposited onto glass substrates. They exhibit a large and broadband reflection asymmetry in the visible spectral range. In order to investigate how the surface morphology affects the asymmetry, we anneal the samples at various temperatures to induce changes in the morphology, and observe changes in the reflection spectra. Our study indicates that the surface roughness and the metal surface coverage are the key geometric parameters affecting the reflection spectra, and reveals that the large asymmetry is due to the different surface roughness light encounters when incident from different side of the film. Additionally, we analyze how thin metal and dielectric layers affect the optical properties of metal-dielectric systems. Using the concept of dispersion engineering, we show that a metal-dielectric-metal microsphere—a metal sphere coated with a thin dielectric shell, followed by a metal shell—support a band of surface plasmon resonances (SPRs) with nearly identical frequencies. A large number of modes belonging to this band can be excited simultaneously by a plane wave, and hence enhancing the absorption cross-section. We also find that the enhanced absorption is accompanied by a plasmon assisted transparency due to an avoided crossing of dominant SPR bands. We demonstrate numerically that both the enhanced absorption and the plasmon assisted transparency are tunable over the entire visible range. We also present an experimental study of light scattering from silica spheres coated with thin semicontinuous silver shells, and attempt to describe their optical response using a modified scaling theory. This dissertation includes previously published co-authored materials.

CURRICULUM VITAE

NAME OF AUTHOR: Keisuke Hasegawa

PLACE OF BIRTH: Nagoya, Aichi, Japan

DATE OF BIRTH: November 2, 1977

GRADUATE AND UNDERGRADUATE SCHOOLS ATTENDED:

University of Oregon, Eugene, Oregon
California Institute of Technology, Pasadena, California
Reed College, Portland, Oregon

DEGREES AWARDED:

Doctor of Philosophy in Physics, 2007, University of Oregon
Bachelor of Arts in Physics, 2001, Reed College College

AREAS OF SPECIAL INTEREST:

Plasmonics, Metamaterials, Science Education

PROFESSIONAL EXPERIENCE:

Graduate Research Assistant,
University of Oregon, 2002 - 2008
Graduate Teaching Fellow,
University of Oregon, 2002 - 2008
Teaching Assistant,
California Institute of Technology, 2001 - 2002

GRANTS, AWARDS AND HONORS:

Clarence and Lucille Dunbar Scholarship (to an outstanding student in the fields of biology, chemistry, computer and information science, human physiology, geological sciences, mathematics, physics, or psychology), University of Oregon, Eugene, Oregon, 2007 - 2008

Phi Beta Kappa Award (to an outstanding student), Reed College, Portland, Oregon, 2001

PUBLICATIONS:

A. Chen, K. Hasegawa, M. Deutsch, V. A. Podolskiy, "Metamaterial coatings for broadband asymmetric mirrors" Opt. Lett. **32**, 1770 (2007).

K. Hasegawa, J. U. Nöckel, M. Deustch, "Curvature-induced radiation of surface plasmon polaritons propagating around bends," Phys. Rev. A **75**, 063816 (2007).

C. A. Rohde, K. Hasegawa, M. Deutsch, "Plasmon assisted transparency in metal-dielectric microspheres," Opt. Lett. **32**, 415 (2007).

C. A. Rohde, K. Hasegawa, M. Deutsch, "Extinction properties and left-handedness of spherical layered metallodielectric resonators," in *CLEO/QELS and PhAST*, Technical Digest (CD) (Optical Society of America, 2006), paper QMC6.

K. Hasegawa, C. A. Rohde, M. Deustch, "Enhanced surface plasmon resonance absorption in metal-dielectric-metal layered microspheres," Opt. Lett. **31**, 1136 (2006).

M. Deustch, K. Hasegawa, C. Rohde, "Plasmon-enhanced absorption and transmission in spherical Bragg resonators," Proc. SPIE **6123**, 612307 (2006).

C. A. Rohde, K. Hasegawa, M. Deustch, "Coherent light scattering from semicontinuous silver nanoshells near the percolation threshold," Phys. Rev. Lett. **96**, 045503 (2006).

C. Rohde, K. Hasegawa, M. Deustch, "Coherent light scattering in percolative metallodielectric nanoshells," in *CLEO/IQEC and PhAST*, Technical Digest (CD) (Optical Society of America, 2005), paper JThA4.

C. Rohde, A. Chen, K. Hasegawa, M. Deustch, "Percolative metal nanoshells for metallodielectric photonic crystals," in *NPIS*, Technical Digest (CD) (Optical Society of America, 2005), paper NWB3.

M. Deustch, K. Hasegawa, J. U. Nöckel, "Surface plasmon polariton propagation around bends at a metal-dielectric interface," Proc. SPIE **5728**, 184 (2005).

C. A. Rohde, K. Hasegawa, A. Chen, M. Deustch, "Percolation-enhanced supercontinuum and second-harmonic generation from metal nanoshells," Mater. Res. Soc. Symp. Proc. **846**, 364 (2005).

K. Hasegawa, J. U. Nöckel, M. Deustch, "Surface plasmon polariton propagation around bends at a metal-dielectric interface," in *CLEO/IQEC and PhAST*, Technical Digest (CD) (Optical Society of America, 2004), paper IWA30.

K. Hasegawa, J. U. Nöckel, M. Deustch, "Surface plasmon polariton propagation around bends at a metal-dielectric interface," Appl. Phys. Lett. **84**, 1835 (2004).

ACKNOWLEDGEMENTS

First of all, I must thank my advisor, Miriam Deutsch, for giving me the opportunity to conduct research for the past six years. I am particularly grateful to her for allowing me to pursue topics that I found interesting even when they were theoretical in nature. If the purpose of graduate school is to train to be independent, then I believe she gave me the room to grow as an independent researcher.

A number of other people were instrumental in my research. Professor Jens Nöckel offered me his theoretical and numerical expertise, which were essential to developing the theory of surface plasmon polariton propagation around bends. My lab mates—especially Chuck Rohde—assisted me in my research and it has always been a pleasure to work with Chuck. I feel very lucky that I had such a great research partner.

I would also like to thank the professors at Reed College, especially Nick Wheeler, Johnny Powell, and David Griffith, who taught me not just to do physics, but also to enjoy physics; and Bonnie Grimm and other staff members of the physics office and the Oregon Center for Optics for their ongoing assistance. There is a traditional phrase in Japan that goes *en no shita no chikara mochi*, which roughly translates to "the hidden/unseen strength holding up the roof." It refers to a person who works hard for others without being recognized for his or her effort. The physics staff and the Reed professors were that "hidden strength" for me.

Being a graduate student is not just about conducting research, and I received tremendous help from my friends and family. For that, I thank Shannon for being my loudest cheerleader; Brian for pulling me when I was too tired to pedal; Libby for being a great listener whenever I had difficulties; Sarah for showing me that there is so much more outside the Willamette Hall; Sacha and Caryn for making me feel grounded; Cybelle and Delilah for always making me feel special; the McCoy family for welcoming me into their life; Shinichi and Masashi for looking out for me from afar; and my family for their lovingkindness.

Lastly, I thank Beck—my best friend—for being my biggest advocate and the toughest critic. *And if I sing you are my voice,*

TABLE OF CONTENTS

Chapter Page

LIST OF FIGURES

Figure Page

CHAPTER I

INTRODUCTION

Surface Plasmon Polaritons

In 1956 Walter H. Brattain, a physics graduate of the University of Oregon, began his Nobel lecture with the following words[1]:

> I would like to start by emphasizing the importance of surfaces. It is at a surface where many of our most interesting and useful phenomena occur. We live for example on the surface of a planet. It is at a surface where the catalysis of chemical reactions occur. It is essentially at a surface of a plant that sunlight is converted to a sugar. In electronics, most if not all active circuit elements involve non-equilibrium phenomena occurring at surfaces. Much of biology is concerned with reactions at a surface. If surfaces are so important, what do we know about them? What is a surface! What properties does a surface have that a physicist can measure?

The science of surfaces is indeed a fascinating subject of research; studies of surface phenomena often reveal crucial aspects of the underlying physics behind the phenomena and frequently lead to new technological applications. For example, Dr. Brattain's invention of the transistor, for which he received the Nobel Prize, originated from his attempt to understand the electronic phenomena at the surface of semiconductors.

Interesting and useful phenomena also occur at the surface of metals. It is commonly known that metal surfaces are highly reflective. When light is

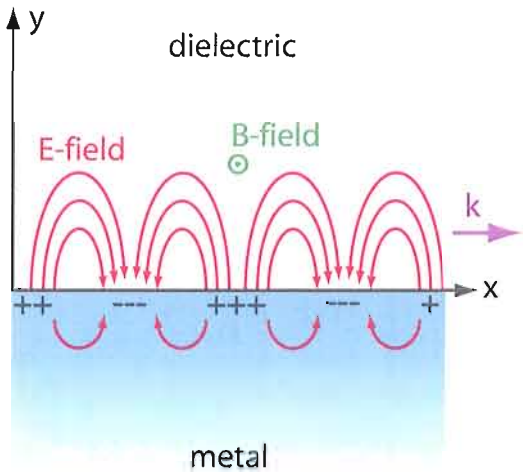

FIGURE 1. A schematic diagram of SPPs. The TM-polarized electromagnetic field is coupled to the free electrons of the metal near the surface, and oscillates coherently with the charge density.

incident on smooth metal surfaces, its interactions with the free electrons generate electromagnetic (EM) waves that decay exponentially into the metal. Unlike propagative waves, these evanescent waves cannot transmit energy through the medium. Without anywhere else to go, the light is reflected back into the surrounding medium giving the surface its "shiny" appearance. However, under certain circumstances, the light becomes trapped at the surface and produces surface waves known as surface plasmon polaritons.

Surface plasmon polaritons, or SPPs, are coupled oscillations of free electrons and EM waves that are confined near metal-dielectric interfaces. When propagating along a flat interface as shown schematically in Fig. 1, the EM field peaks at the interface and decays exponentially into the two adjoining media. The electromagnetic field of

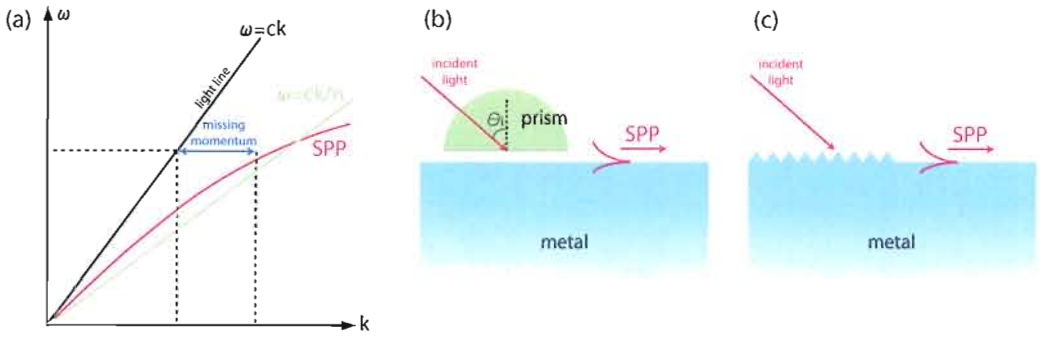

FIGURE 2. (a) The dispersion relations for SPPs. Since it is on the right of the light line, SPPs cannot be excited directly by the incident light. Two common methods of exciting SPPs use a prism (b) or a periodic corrugation (c) to provide the missing momentum.

the SPPs is transverse magnetic (TM) with its magnetic field given by

$$\vec{B} = \hat{z} B_0 e^{ikx - i\omega t} \begin{cases} \exp(-\gamma_o y) & y \geq 0 \\ \exp(\gamma_i y) & y < 0 \end{cases}, \tag{I.1}$$

where

$$k = \frac{\omega}{c} \sqrt{\frac{\epsilon_i \epsilon_o}{\epsilon_i + \epsilon_o}} \tag{I.2}$$

and $\gamma_{o,i} = \pm\omega\epsilon_{o,i}\sqrt{-1/(\epsilon_i + \epsilon_0)}/c$. The optical response of the metal is described by its dielectric function $\epsilon_i(\omega)$ with a negative real part, while that of the dielectric medium is given by a positive permittivity ϵ_o. Since ϵ of metal is generally complex, the wavenumber k of SPPs are also complex. As is shown in Fig. 2(a), the dispersion relations of SPPs lie outside the light line, rendering a direct excitation by a free-propagating light impossible. Two common methods of exciting SPPs use a prism or a periodic corrugation to provide the missing momentum as depicted in Fig. 2(b) and (c)[2]. In the prism coupling, also known as the attenuated total reflection (ATR) coupling, the wavenumber of the incident light becomes $k_i = n\omega/c$ instead of $k_i = \omega/c$.

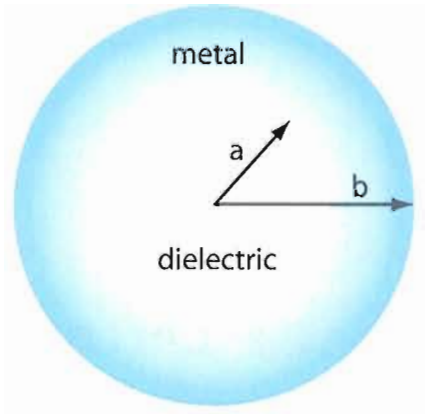

FIGURE 3. A schematic diagram of the nanoshell. Its resonant frequencies can be tune by varying the ratio of its inner and outer radius.

As a result, a part of SPP dispersion relation would now be inside the light cone of the prism and SPPs, and SPPs are resonantly excited when the in-plane momentum of the incident light matches that of SPPs:

$$n\frac{\omega}{c}\sin\theta_i = \mathrm{Re}\left[\frac{\omega}{c}\sqrt{\frac{\epsilon_i\epsilon_o}{\epsilon_i+\epsilon_o}}\right].$$

Once excited, SPPs are tightly confined near the surface and propagate along the interface and travel a distance determined by the dissipation in the media. According to Eq. (I.1), SPPs propagate along the metal surface with a complex wavenumber k. Therefore, as they propagate, the field intensity decays exponentially. The propagation length is given by $L_{spp} \equiv 1/\mathrm{Im}[2k]$. The degree of the surface confinement of the electromagnetic intensity is determined by $\delta_{o,i} \equiv 1/\mathrm{Re}[2\gamma_{o,i}]$. In the visible range, SPPs on a silver-air interface travel tens of microns, and have $\delta_o \approx 150\mathrm{nm}$ and $\delta_i \approx 10\mathrm{nm}$, well below the diffraction limit of $\lambda/2$.

SPPs can also be excited on non-planar metal-dielectric interfaces. Nanoscopic metal particles, for example, support SPPs that are localized in space. Unlike the extended SPPs on flat interfaces, the localized modes can be excited directly by a plane wave, and they exhibit resonant behaviors. These surface plasmon resonances (SPRs) are highly sensitive to the dielectric environment and the geometry of the nanoparticles. By adjusting the shape and size of the metal particles, it is possible to geometrically tune the resonances over a broad frequency range[3–5]. For instance, resonant frequencies of nanoscale core-shell particles, called nanoshells (Fig. 3), can be tuned from near-UV to mid-infrared frequency by varying the ratio of the inner and outer shell radius[6, 7]. By increasing the number of metal-dielectric interfaces, it is also possible to tune multiple resonance frequencies simultaneously[8] or even engineer the entire dispersion relations[9, 10].

Emergence of Plasmonics and Plasmon-based Metamaterials

Scientists have known about the existence of surface waves at metal-dielectric interfaces for over 50 years[11]. However, the study of SPPs has intensified only in the last several years. The growing interest in plasmonics, a subfield of photonics which investigates the nature of SPPs of metal-dielectric systems, is primarily application driven. Much of ongoing research is aimed at developing novel plasmon-based optical devices and materials by utilizing the unique properties of SPPs—specifically, their subwavelength confinement and geometric tunability.

One of the main areas of research in plasmonics is waveguiding and manipulation. While today's conventional photonic elements are capable of fast data transfer and processing, their size scales are limited by the diffraction limit. On the other hand, the surface confinement of SPPs can be well below the diffraction limit as shown in the previous section. Therefore, SPPs may lead to a miniaturization of photonic devices. Thus far, efficiencies of various plasmonic waveguides and other plasmonic elements have been studied. Many of the waveguides are based on triple layered structures, both dielectric-metal-dielectric and metal-dielectric-metal, to guide SPPs through metal strips or dielectric gaps[12–16]. Metallic nanowires, nanopatterned metallic films, ordered arrays of metal nanoparticles, and other complex structures have also been shown to guide SPPs[17–22]. Other fundamental circuit elements such as mirrors, beamsplitters, interferometer, Y-splitters, ring resonators, modulators, and switches have been demonstrated[23–28]. A major limitation of surface plasmon waveguiding and manipulation is the attenuation of SPPs through the dissipation of the metal. However, studies have shown that a gain medium may be used to compensate for the energy loss[29–33].

Another area of active research is plasmon-based optical sensing. When SPPs are excited by a propagating wave, their electromagnetic field at the metal-dielectric interface can be greatly enhanced over that of the incident light. This near-field enhancement is due to the evanescent field profile of SPPs, and it can be exploited to perform highly sensitive chemical and biological sensing. The plasmon-based

optical sensing was initially performed with SPPs on a flat, chemically functionalized metal surface under the ATR coupling, as shown in Fig. 2(b)[34, 35]. The surface functionalization allows a specific chemical or biological agent to bind to the metal surface, which modifies the refractive index or the dielectric permittivity ϵ_o. This in turn alters the dispersion relations of SPPs via Eq. I.2. Thus, a measurement of the incident angle θ_i at which SPPs are resonantly excited reveals the presence or the absence of the target agent. Such prism-based sensors are capable of detecting a refractive index change less than 3×10^{-7}[36], and are already commercially available from a number of companies, including Biacore, Nomadics, and DKK-TOA Corporation. Sensitive detection of chemical and biological agents can also be accomplished with a variety of other metal-dielectric systems. In nanoparticle-based sensing, a shift in SPR frequencies is often monitored as a way to detect a small change in the dielectric environment. Studies have shown that ordered and disordered arrays of nanoparticles can be used for protein detection[37–40]. DNA and antigen sensing with functionalized gold nanoparticles and nanoshells have also been reported[41, 42]. Furthermore, localized SPRs of nanoshells have been shown to enhance Raman scattering of molecules absorbed on surface by a factor of 10^{12}[43], and can be used for chemical identification. Additionally, nanoshell-based cancer imaging and treatment of cancer have been demonstrated[44, 45].

Plasmonic metamaterial engineering is yet another active area of research. Metamaterials are a class of artificial materials designed to produce tailored

electromagnetic responses. Unlike photonic crystals whose periodicity is comparable to the wavelength λ, metamaterials consists of building blocks whose dimensions are significantly smaller than λ. Therefore, it is generally possible to consider a metamaterial as a homogeneous medium with an effective permittivity ϵ_{eff} and permeability μ_{eff}. This is analogous to assigning ϵ and μ to a conventional material to describe the collective response of its constituent atoms. The macroscopic optical properties of a metamaterial are typically derived from the electromagnetic response of its microscopic constituents. As a result, the geometric tunability of SPRs is an ideal tool for metamaterial engineering. In recent years, a number of plasmonic metamaterials that exhibit optical properties not readily observed in nature have been studied. Of those, metamaterials with simultaneously negative permittivity and permeability, also called left-handed materials (LHMs), are perhaps most intensely investigated. In LHMs, the index of refraction is negative. This leads to unusual optical phenomena such as negative refraction, perfect lensing, reversed Doppler shift, and inverse Cherenkov radiation[46–48]. To date, several left-handed metamaterials composed of plasmonic elements—such as split ring resonators[49], paired parallel nanorods[50], H-shaped metal wires[51], double metal pillars[52], and cut-wire structures[53]—have been demonstrated. Studies have also shown that metamaterials may lead to optical cloaking[54–57].

Although significant progress has been made in various applied aspects of plasmonics, our present understanding of the fundamental nature of SPPs is still

far from complete. In particular, how the general features of metal surfaces, such as curvature and roughness, affect fundamental SPP behaviors are not well understood. Acquiring this knowledge is critical as it would provide a set of conceptually intuitive tools for controlling and manipulating SPPs. With such tools, we are better able to design new plasmonic devices, which would outperform existing plasmonic devices. In this dissertation, we show, both theoretically and experimentally, the effect of geometry and surface morphology on SPPs and the optical properties of metal-dielectric systems.

Outline of this Dissertation

In Chapter 2, we present a theoretical study of the propagation of SPPs on curved metal-dielectric interfaces. First we qualitatively describe the origin of curvature-induced radiation of SPPs propagating around bends and its effect on the SPP propagation efficiency. We then develop an analytical model for quantifying the transmission efficiency, and show that the problem is analogous to the scattering from a one-dimensional (1D) finite potential well/barrier. Subsequently, a numerical analysis of the bend propagation is presented, and its results are compared with the analytical results. We further show that it is possible to enhance the transmittance by introducing a plasmonic resonator at bends. The material in this chapter was previously published with J. U. Nöckel and M. Deutsch in Ref. [58] and [59].

The effect of surface roughness on SPPs and the scattering of light from random metal-dielectric systems is explored in Chapter 3. The chapter begins by reviewing the effective medium theories of disordered media, which ignore the effect of surface roughness. We present a theoretical and experimental investigation of thin, random metal-dielectric films which act as double-sided metamaterial mirrors exhibiting a large, broadband reflectance asymmetry. We show that the asymmetry cannot be described by any effective medium theory, which ignores the effect of surface roughness. The study of the broadband asymmetric mirrors was previously published with A. Chen, V. A. Podolskiy, and M. Deutsch in Ref. [60]. We next investigate the origin of the broadband reflection asymmetry by observing how changes in surface morphology induced by annealing affect the reflectance spectra, and show that the reflection asymmetry is due to the different surface roughness light encounters when incident from different sides of the film.

In Chapter 4, we present a study of SPRs in layered metal-dielectric particles. We focus on two types of systems: metal-dielectric-metal (MDM) spheres, consisting of metal cores, surrounded by a thin layer of dielectric shell, followed by a metal shell; and percolative nanoshells, made of dielectric cores surrounded by a layer of semicontinuous metal film. In the first part of the chapter, we discuss the geometric tunability of the MDM sphere's dispersion relations. In particular, we derive a simple geometric condition for which the system supports a band of SPRs whose resonant frequencies are nearly identical. We demonstrate numerically that these SPRs can be

excited simultaneously by a plane wave, and enhance the absorption cross section of the system. We also show that the system also exhibits a tunable optical resonance. The material in the first part of the chapter previously published with C. Rohde and M. Deutsch in Ref. [9] and [10]. The second part of the chapter present a study of the scattering of light from percolative nanoshells. Our experiment indicates that such nanoshells support cluster-localized SPRs that are coherently driven due to the spherical geometry. We present a modified scaling theory to model the dynamics of the SPRs. This material was previously published with C. Rohde and M. Deutsch in Ref. [61]. We close the dissertation with concluding remarks in Chapter 5.

CHAPTER II

SURFACE PLASMON POLARITON PROPAGATION ON CURVED METAL SURFACES

This chapter introduces a theoretical study of the propagation and the curvature-induced radiation of SPPs propagating around bends. The material in this chapter was previously published with J. U. Nöckel and M. Deutsch in Ref. [59], which, in turn, was based on our earlier work in Ref. [58]. My specific contribution was to develop the analytical and numerical models under the guidance of J. U. Nöckel and M. Deutsch

Introduction

The propagation of SPPs on curved metal surfaces is an important, yet often misunderstood topic. As discussed in Chapter I, when SPPs travel on flat metal surfaces, the propagation distance is only limited by the dissipation in the metal. However, when traveling on curved surfaces, SPPs also experience radiation loss, degree of which depends on the radius of curvature, much like light traveling through bent optical fibers. This additional loss mechanism can significantly alter the propagation length of SPPs. Yet there is a general misconception among some scientists that SPPs can travel on curved metal surfaces efficiently. For example,

in *Physical Review Focus*, Don Monroe writes "[SPP] travels only along the surface and ... turns corners like a sports car"[62]. In fact, as shown in this chapter, in many instances of practical interest where tight (and preferably subwavelength) turns are desirable, SPPs lose most of their energy through radiation, and thus, do not travel efficiently around bends.

As the need for integration of compact lightwave devices is growing, it is necessary that we develop a quantitative theory of curvature-induced radiative energy loss in SPPs propagating at curved metal-dielectric interfaces. This enables the determination of SPP propagation efficiencies when the radius of curvature is smaller than or comparable to the signal wavelength[58, 59, 63, 64]. Careful analysis of the relations between the propagation efficiency and the interface curvature is essential when designing plasmonic devices, as it should set a limit on the radius of curvature and, subsequently, on feature size in plasmonic-circuits. Several recent studies have addressed surface plasmon waveguiding around bends. However, these studies are primarily focused on *in-plane* guiding[13, 14, 65, 66] or on using multiple-interface geometries such as metal-dielectric-metal waveguides[67] or long-range SPP waveguides[68]. To date, SPP guiding on a single bent interface remains largely unknown.

This chapter presents a theoretical analysis of the propagation and curvature-induced radiation of SPPs traveling around bends at metal-dielectric interfaces. First, we introduce the geometry of our system, followed by a simple qualitative analysis

describing the radiative nature of SPP propagation around bends. This enables us to develop a more rigorous analytical approach for calculating losses and propagation efficiencies, which we present in the subsequent section. A numerical analysis is also described, and its results are compared with the analytical results. Moreover, a novel resonator-based method for enhancing the transmittance is also described and analyzed. Conclusions are presented in the last section.

Geometry of the Curved Metal-Dielectric Interface

The geometry of our study is shown in Fig. 4(a). The system consists of a curved metal-dielectric interface occupying region II in space, matching smoothly to planar and semi-infinite interfaces in regions I and III. The axes x_1 and x_2 define the boundaries between the three regions, and the system is infinite in the z direction. The rounded edge is characterized by a permittivity ϵ_i, with a fixed radius R and a finite bend angle θ. The surrounding space is characterized by a permittivity ϵ_o. Propagating SPPs of frequency ω are incident from region I onto the boundary at x_1, and their counterclockwise transmission through region II into region III is analyzed. We initially consider the case of SPPs propagation around a *metallic corner* with $\mathrm{Re}[\epsilon_i] < 0$ and $\epsilon_o > 0$, depicted schematically in Fig. 4(b). This is essentially a segment of an infinitely long metal cylinder. We then analyze the complementary reverse geometry shown in Fig. 4(c), in which SPPs propagate around an open *dielectric void*.

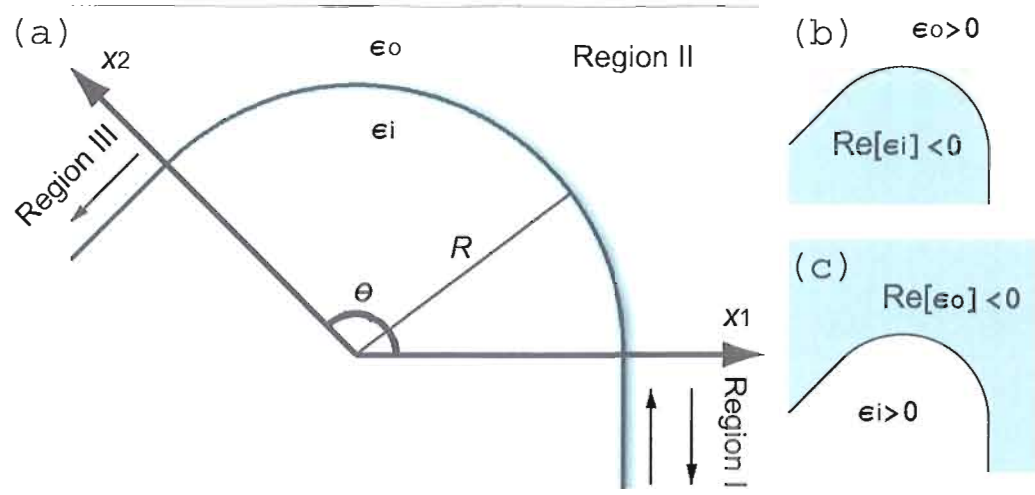

FIGURE 4. (a) The geometry of the curved metal-dielectric interface. A rounded edge, characterized by a permittivity ϵ_i, has a bend angle θ and a finite bend radius R. The bend is confined to the region of space shown, with center of curvature at the origin. The rest of space is occupied by a medium with ϵ_o. Axes x_1 and x_2 extend along the boundaries between regions I and II and regions II and III, respectively. In the $x_1 - x_2$ plane, regions I and III are semi-infinite. The system is also infinite in extent along the entire z axis. Arrows indicate incident and reflected fields in region I, and transmitted field in region III. In addition, (a) shows the intensity of SPPs in greyscale. The intensity distribution is calculated for SPPs traveling around a metallic corner (b), using the single-mode approximation developed in the text. We also consider the complementary configuration, in which SPPs propagate around a dielectric void (c).

Curvature-induced Radiation: Qualitative Analysis

The generalized dispersion relation of SPPs propagating at a metal-dielectric (i.e. *anisotropic*) interface is

$$\epsilon_{o,i}\frac{\omega^2}{c^2} = k_{\|}^2 + k_{\perp o,i}^2 \tag{II.1}$$

where $k_{\|}$ and $k_{\perp o,i}$ are the components of the k-vector parallel and perpendicular to the interface, respectively. For a surface-guided mode, we require $k_{\|} > \sqrt{\epsilon_o}\omega/c$ such

that $k_{\perp o,i}$ becomes imaginary, hence non-radiative. Rewriting this simple expression yields $\omega/k_{\|} < c\sqrt{\epsilon_o}$. Simply stated, the phase velocity in the direction parallel to the interface, $v_{\|} \equiv \omega/k_{\|}$, cannot exceed the speed of light, $c/\sqrt{\epsilon_o}$, in order to sustain non-radiative guiding.

When propagating around a bend, $v_{\|}$ acquires a radial dependence, with EM fields more distant from the interface traveling at greater phase velocities. Thus, there exists a threshold radius, $r^{\star}$, where the parallel phase velocity reaches the speed of light. Beyond $r^{\star}$ the EM field of the SPP becomes radiative. As a result, SPPs can be guided along curved interfaces with negligible radiation loss as long as the fields are confined near the metal-dielectric interface and do not extend beyond $r^{\star}$. This claim is verified analytically in the next section.

Transmission Efficiency: Quantitative Analysis

In order to quantify the degree of radiation loss and the propagation efficiency of SPPs around the bend we now exploit known solutions of Maxwell's equations describing angular propagation of EM waves at the surface of an infinitely long metal cylinder. These solutions are applicable in region II. The magnetic field is hence given by

$$\vec{B} = \hat{z}e^{-i\omega t}\sum_{\{n\}}\begin{cases}\left[A_n^{+}e^{+in\phi} + A_n^{-}e^{-in\phi}\right]J_n(k_i r) & r \leq R \\ \left[B_n^{+}e^{+in\phi} + B_n^{-}e^{-in\phi}\right]H_n^{(1)}(k_o r) & r > R\end{cases}, \qquad \text{(II.2)}$$

where $k_{i,o} = \omega\sqrt{\epsilon_{i,o}}/c$, J_n is the Bessel function, and $H_n^{(1)}$ is the Hankel function of

the first kind. The set of mode indices $\{n\}$, denoting radial excitations, is determined by the metal boundary matching equation

$$0 = \frac{1}{k_i}\frac{J_n'(k_iR)}{J_n(k_iR)} - \frac{1}{k_o}\frac{H_n^{(1)'}(k_oR)}{H_n^{(1)}(k_oR)}, \tag{II.3}$$

where the prime denotes differentiation with respect to the argument. Since region II comprises only a segment of a full cylinder (i.e. $\theta < 2\pi$,) periodic boundary conditions need not be satisfied, and n is therefore not constrained to integer values. In fact, since we choose the frequency ω to be real-valued, one finds n to have a non-vanishing imaginary part as well. The latter is a consequence of radiation loss and absorption in the bend.

The azimuthal dependence of the SPP wave is given by the standard expression $\exp[\pm in\phi]$, where ϕ is the measured from the x_1 axis. Thus only solutions with $\mathrm{Im}[n] \geq 0$ are admissible, describing attenuated propagation. Away from the interface in the dielectric region, where $k_o r \gg \mathrm{Re}[n]$ is satisfied, we may use the asymptotic form of the Hankel function: $H_n^{(1)}(k_o r) \approx \sqrt{2/\pi k_o r}\exp[i(k_o r - (2n+1)\pi/4)]$. Each mode can now be written as

$$\vec{B}_n \sim \hat{z}e^{\pm in\phi}\frac{e^{i(k_o r - \omega t)}}{\sqrt{r}} \tag{II.4}$$

thus recovering the expected free propagating cylindrical wave form.

In general, Eq. (II.3) cannot be solved algebraically, and it is necessary to employ a numerical method to find the set $\{n\}$. One convenient numerical approach employs

graphical plotting of the right-hand side of Eq. (II.3) as functions of both Re[n] and Im[n], and identifying its zeros in the complex n-plane.

In principle, the set of solutions denoted by $\{n\}$ is infinite. In practice, we find that a single mode of this set dominates the propagation problem we are analyzing in this work. The set $\{n\}$ contains a *fundamental mode* (i.e. the surface plasmon mode), which we label with mode index $m \in \{n\}$. The EM field of this mode is concentrated near the metal-dielectric interface. The solid line in Fig. 5 shows the dispersion relation of this fundamental mode. In the limit of large momentum, it asymptotically approaches $\omega_{sp} \equiv \omega_p/\sqrt{1+\epsilon_o}$, the conventional limit for surface plasmon modes. Also shown in Fig. 5 are the dispersion relations of modes in the set $\{n\}$ with higher radial excitation values (dashed lines). We see that these modes do not approach ω_{sp} asymptotically. Compared to the fundamental, these modes are also found to be less confined to the interface. As the radial excitation number increases even further, the modes corresponding to these values of n all lie to the right of the three non-fundamental modes shown in Fig. 5. As expected from the fundamental mode, Im[m] is the smallest of the set $\{n\}$ since the confinement of this mode to the interface is maximal, hence its radiation losses are the lowest. This is generally true for metals such as gold and silver, where the absorption losses are relatively low. If the metal is highly absorptive modes with stronger field confinement may have larger Im[n], since they experience greater absorption loss.

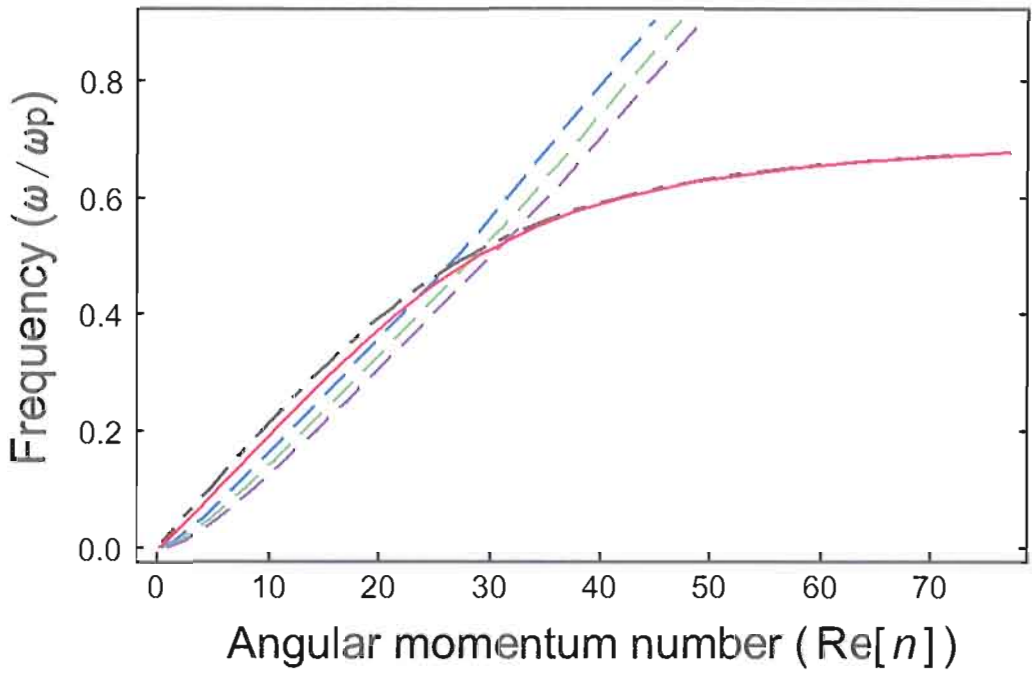

FIGURE 5. Dispersion relations of transverse-magnetic modes on a metal cylinder with $R = 2\mu$m. The dispersion relation for the fundamental mode (solid line) closely follows that of SPPs on a flat metal-dielectric interface (dash-dotted line). The horizontal scale of the latter is normalized by the factor R, so that the curve is a plot of ω as function of kR, instead of k. Dispersion relations of modes with higher radial excitations are also shown (dashed lines). These modes are less confined to the interface and do not approach $\omega_p/\sqrt{2}$ asymptotically. Higher radial excitation modes with even weaker surface confinement exist (not shown), all lying to the right of the three dashed lines shown.

As shown in Fig. 5, away from ω_{sp} the fundamental mode has the smallest angular momentum ($\approx kR$) at a given frequency. To understand this, we consider the following: The angular momentum is $\vec{L} = \int (\vec{r} \times \vec{S}/c^2) dr^3$, where $\vec{S}$ is the Poynting vector. Compared to other modes, the fundamental mode is more strongly confined near the surface. Since $\vec{S}$ for this mode is significant only at $r \simeq R$, the integrand is minimal (as long as $\vec{S}$ of the fundamental mode is not disproportionately large.) However, as the frequency approaches ω_{sp}, $\vec{S}$ increases asymptotically, which

overcompensates for the smaller value of $\vec{r}$. This is seen in Fig. 5 as a crossover of the fundamental mode and the other depicted modes, such that at $\omega \sim \omega_{sp}$ its angular momentum is higher than that of the less confined modes.

The radiative nature of the SPP solutions described by Eq. (II.2) is also consistent with the qualitative analysis presented in the previous section. This can be verified by analyzing the nature of the Hankel function $H_n^{(1)}$. The Hankel function is non-oscillatory (depicting non-radiative fields) while its argument is smaller than the order $\mathrm{Re}[n]$. When the argument exceeds $\mathrm{Re}[n]$, $H_n^{(1)}$ starts to approach its oscillatory (radiating) form, as shown by the asymptotic expression leading to Eq. (II.4). The non-oscillatory–to–oscillatory transition occurs when the argument and the order are approximately equal. We are thus led to conclude that each mode of Eq. (II.2) undergoes a non-radiative–to–radiative transition at a radius given by $k_o r \approx \mathrm{Re}[n]$.

The transition radius described above coincides with the previously introduced threshold radius, $r^\star$. By definition, at $r = r_n^\star$ we require $v_\parallel = c/\sqrt{\epsilon_o}$, where the mode index n is added to $r^\star$ since each mode with index n has a different threshold radius $r_n^\star$ in region II. The phase flow in the parallel direction is characterized by $\exp(i\mathrm{Re}[n]\phi)$, and its associated wavenumber and phase velocity are $k_\parallel = \mathrm{Re}[n]/r$ and $v_\parallel = \omega/k_\parallel = \omega r/\mathrm{Re}[n]$, respectively. We thus obtain

$$r_n^\star = \frac{\mathrm{Re}[n]}{k_o}, \tag{II.5}$$

verifying that the threshold radius is indeed the non-radiative–to–radiating-SPP transition radius. From this it follows that the fundamental mode m, with lowest

angular momentum (for $\omega < \omega_{sp}$,) also has the smallest threshold radius for radiation:

$$r_m^\star = \frac{\mathrm{Re}[m]}{k_o} \approx \mathrm{Re}\left[\sqrt{\frac{\epsilon_i}{\epsilon_i + \epsilon_o}}\right] R. \tag{II.6}$$

The approximation above follows from $\mathrm{Re}[m] \approx kR$, where $k = \omega\sqrt{\epsilon_i\epsilon_o/(\epsilon_i + \epsilon_o)}/c$ is the wavenumber of SPPs propagating at a flat metal-dielectric interface. The validity of this approximation is confirmed in Fig. 5, where it is shown that the dispersion relation of the fundamental mode is very close to that of SPPs at a flat interface.

The above analysis implies that when the majority of the SPP field is confined to a region with $r < r_m^\star$, we should expect a negligible radiation loss during propagation. On the dielectric side of the interface the SPP field decays as $\exp\{-\mathrm{Re}[\gamma_o(r - R)]\}$, with the decay coefficient is given by $\gamma_o = \omega\epsilon_o\sqrt{-1/(\epsilon_i + \epsilon_0)}/c$. We see that the field confinement in the dielectric is therefore characterized by $\mathrm{Re}[\gamma_o]$. Thus, we conclude that the radiation loss is insignificant if $G > 1$, where G is the exponent evaluated at $r = r_m^\star$:

$$G\left(\epsilon_i, \epsilon_o, \omega R/c\right) \equiv \mathrm{Re}[\gamma_o](r_m^\star - R). \tag{II.7}$$

In Fig. 6 we plot $\mathrm{Im}[m]$ as function of G. The metal is assumed lossless (i.e. $\mathrm{Im}[\epsilon_i] = 0$), therefore $\mathrm{Im}[m]$ is related solely to radiative loss. We find that $\mathrm{Im}[m]$ is a monotonically decreasing function of G, as expected from the arguments above. Moreover, when $G = 1$ $\mathrm{Im}[m] = 1.24 \sim 1$, confirming again that $G = 1$ is a very good approximation of the threshold where SPP propagation changes from significantly radiative ($\mathrm{Im}[m] \gtrsim 1$) to mostly non-radiative ($\mathrm{Im}[m] \lesssim 1$).

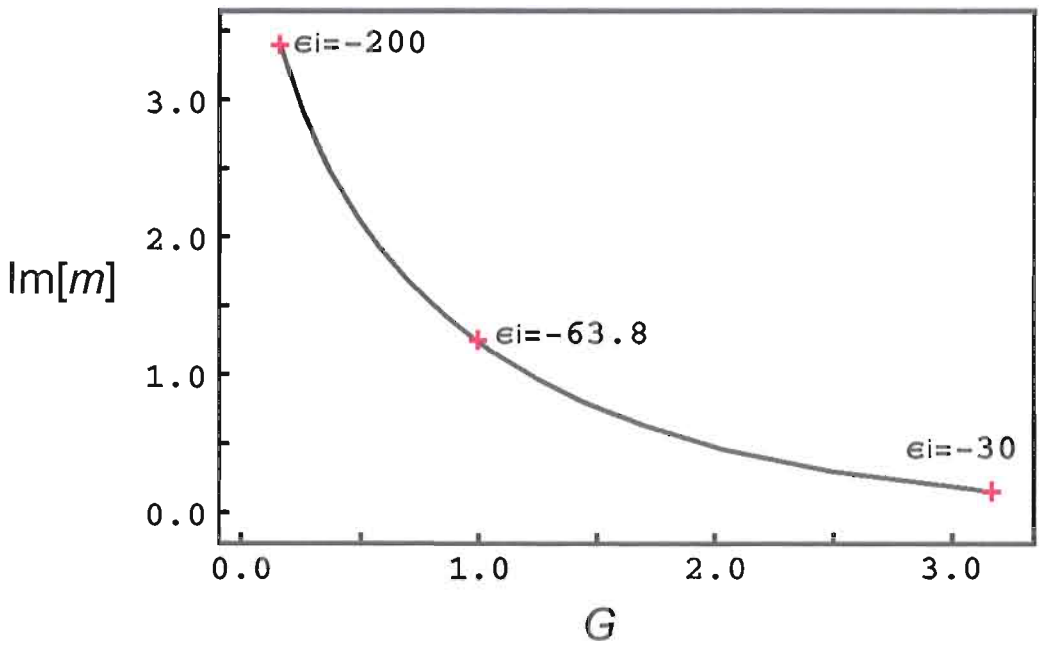

FIGURE 6. Plot of the radiative loss as a function of the field confinement for $\omega R/c = 1000$ and $\epsilon_o = 1$. The permittivity ϵ_i is real and varies from $\epsilon_i = -30$ to -200.

To quantify the radiation loss and propagation efficiency around the bend it is now necessary to consider the coupling of these metal-cylinder modes to planar-interface SPP modes (i.e. propagating modes in regions I and III). The magnetic field of the SPP incident from Region I is given by

$$\vec{B} = \hat{z}A\exp\big(iky_1 - i\omega t\big)\begin{cases} \exp\big[+\gamma_o(x_1 - R)\big] & x_1 < 0 \\ \exp\big[-\gamma_i(x_1 - R)\big] & x_1 \geq 0 \end{cases} \tag{II.8}$$

with A the amplitude and $\gamma_i = -\omega\epsilon_i\sqrt{-1/(\epsilon_i + \epsilon_0)}/c$. Similar expressions hold for the SPPs reflected into region I and the fields transmitted into region III.

Calculating exact values of the transmission and reflection coefficients is often impractical, since it requires matching an infinite number of modes in Eq. (II.2)

to planar SPP modes in regions I and III. The mode matching must be carried out along the entire spatial extent of the x_1 and x_2 axes at the boundaries. However, in certain cases it is possible to derive relatively simple approximate expressions for the required field coefficients. This is because although each mode of region II has an EM field profile normal to the surface which does not exactly match the field profile of the incident planar SPP, *the fundamental mode of region II minimizes this spatial mismatch.* Non-fundamental modes are characterized by EM fields which are less confined to the surface, therefore their field profiles deviate more strongly from those of the planar SPPs whose fields are always strongly bound at the metal-dielectric interface.

In the short wavelength limit, it is possible to show that incident SPP and the fundamental mode have *identical* field profiles near the interface. In this limit, the field distribution of the fundamental mode in the radial direction can be obtained by taking the appropriate limit of the Bessel equation

$$r^2\frac{d^2f}{dr^2} + r\frac{df}{dr} + (k_{o,i}^2 r^2 - m^2)f = 0$$

to which $J_m(k_i r)$ and $H_m^{(1)}(k_o r)$ are solutions, respectively. As $\omega R/c \to \infty$, the curvature of the metal surface becomes insignificant and m approaches kR. With $r = R + x$, in the limit $x \ll R$ the Bessel equation reduces to $R^2 d^2f/dx^2 + (k_{i,o}^2 - k^2)R^2 f = 0$, to which the solutions are exponentials. Thus, noting that $\gamma_{i,o}^2 = k^2 - k_{i,o}^2$, $J_m(k_i r) \sim \exp(\gamma_i r)$ and $H_m^{(1)}(k_o r) \sim \exp(-\gamma_o r)$ which is identical to the behavior of the SPP fields in regions I and III near the interface. Far from the interface

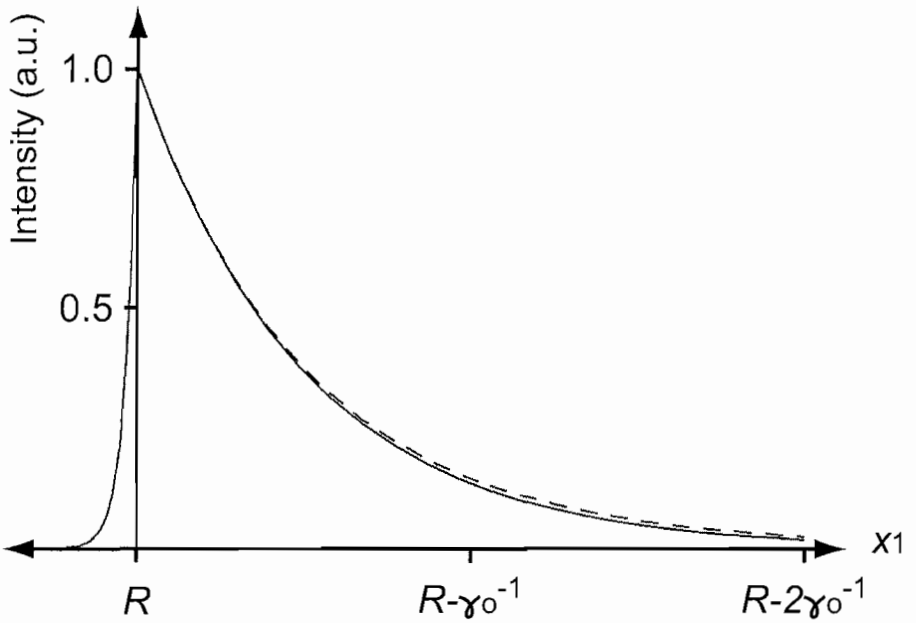

FIGURE 7. Comparison of intensity profiles of SPPs in region I (solid line) and the fundamental mode in region II (dashed line), calculated for $\omega R/c = 800$. The profile mismatch is barely visible, indicating that SPPs in region I couple predominately to the fundamental mode in region II.

where the condition $x \ll R$ no longer holds, $J_m(k_i r)$ and $H_m^{(1)}(k_o r)$ no longer exhibit exponentially decaying behaviors. However, due to the exponential decay near the interface, their values are small far from the interface, making the mismatch negligible along the entire x_1 and x_2 axes. This is illustrated in Fig. 7, where we show that the intensity profiles of the fundamental mode and the planar SPP are well matched in the short wavelength limit.

We are thus led to conclude that in the short wavelength limit planar SPPs couple predominately to the fundamental mode, and neglect their coupling to all other non-fundamental modes. For this reason, under this single-mode approximation, it is necessary to consider only a small number of modes: the incident and reflected SPPs

in region I, the clockwise and counterclockwise propagating fundamental mode in region II, and the transmitted SPP in region III. These modes are matched at a single point on at each axis, at a distance R from the origin, via the standard Maxwell boundary conditions. Our analysis above ensures that the boundary conditions are then approximately satisfied over the entire extent of the axes. The problem of quantifying the propagation efficiency has now essentially become one dimensional (1D), and it is mathematically analogous to scattering from a 1D finite potential well[69]. However, since the allowed m values are always complex, bound-state solutions in this type of well do not exist. This distinguishes SPPs at curved surfaces from waveguide bends enclosed on all sides by infinite potential walls[70].

Applying the appropriate boundary conditions to the fields at the x_1 and x_2 boundaries results in expressions for the transmittance T and reflectance R:

$$\mathsf{T} = \left| \frac{4mkR}{-e^{im\theta}(m-kR)^2 + e^{-im\theta}(m+kR)^2} \right|^2 \tag{II.9}$$

$$\mathsf{R} = \left| \frac{2\sin(m\theta)(m^2-k^2R^2)}{-e^{im\theta}(m-kR)^2 + e^{-im\theta}(m+kR)^2} \right|^2 . \tag{II.10}$$

In the presence of significant absorption or radiation loss, such that $\mathrm{Im}[m]\theta \gg 1$, these expressions become

$$\mathsf{T} \approx 16 \frac{|mkR|^2}{|m+kR|^4} e^{-2\mathrm{Im}[m]\theta} \tag{II.11}$$

$$\mathsf{R} \approx \left| \frac{m-kR}{m+kR} \right|^2 . \tag{II.12}$$

As $\omega R/c \to \infty$, these expressions become exact.

In general, conservation of energy is expressed by $1 = \mathsf{T} + \mathsf{R} + \mathsf{P} + \mathsf{A}$, where P and A are the radiation and absorption loss coefficient, respectively. For a metal characterized by a real permittivity, the absorption loss vanishes, and the radiation loss can be easily calculated using the above expressions for T and R. For a lossy metal, radiation losses must be calculated independently in order to extract the absorption loss from the expression above. The radiation loss is obtained by integrating the Poynting vector for unit incident flux in region II at $r \to \infty$:

$$\mathsf{P} \equiv \int_{\phi_0}^{\theta+\phi_0} \vec{S} \cdot \hat{r} r d\phi. \tag{II.13}$$

The lower integration limit is set to ϕ_0 instead of 0, since the energy radiated from the surface at $\phi = 0$ propagates at an angle ϕ_0 into the far field. Likewise, the upper integration limit is $\theta + \phi_0$ instead of θ. In the short-wavelength limit only the amplitude of the forward-propagating mode is significant, therefore the radiation losses are well approximated by integrating only the counterclockwise propagating mode. A stationary phase approximation is used to obtain an expression for ϕ_0, using the position-dependent phase $\Phi = k_o r + \mathrm{Re}[m]\phi$. The change in angle as the wave propagates a radial distance δr is $\delta\phi = \mathrm{Re}[m]/(k_o r^2)\delta r$, giving $\phi_o = \int_R^\infty \mathrm{Re}[m]/(k_o r^2) dr = \mathrm{Re}[m]/k_o R$.

Calculations were carried out using typical values of silver ($\epsilon_i = -15 + i0.5$) in air ($\epsilon_o = 1$) with $\omega R/c = 800$ and $\theta = 90°$. Assuming that the metal is lossless ($\epsilon_i = -15$), we find that most of the incident SPP energy is transmitted with $\mathsf{T} = 0.997$, $\mathsf{R} = 1.19 \times 10^{-8}$, and $\mathsf{P} \approx 0.003$. When the absorption loss is accounted for the

results change drastically to $\mathsf{T} = 0.0516$, $\mathsf{R} = 1.18 \times 10^{-6}$, and $\mathsf{P} \approx 0.00282$. This result implies that absorption is the dominant loss mechanism when $R \gg \lambda$ even for metals such as silver with relatively low losses. Surprisingly, we find that the overall absorption and radiation losses of SPPs propagating at a non-planar interface may be *lower* than the absorption loss of SPPs traveling the equivalent arc distance on a flat surface. This counterintuitive result comes from the fact that the field inside the metal in region II travels an arclength less than θR due to the curvature. As a result, SPP fields sample less of the metal volume when propagating on the curved interface than when propagating on a flat surface, resulting in the reduced absorption.

In order to evaluate the accuracy of our results, it is necessary to quantify the validity of the single-mode approximation. As discussed earlier, the single mode approximation is only appropriate when the field profile of the fundamental mode (represented by the solution to the Bessel equation) well approximates the exponentially decaying behavior of the planar SPP. Thus, evaluating the mismatch between the Hankel function and the decaying exponential gives a measure of whether the approximation is appropriate or not. We define the *normalized mismatch* as

$$\Delta^2 \equiv \frac{\int_R^{R+\eta\gamma_o^{-1}} \left|\exp[-\gamma_o(r-R)] - \frac{H_m^{(1)}(k_o r)}{H_m^{(1)}(k_o R)}\right|^2 dr}{\int_R^{R+\eta\gamma_o^{-1}} \left|\exp[-\gamma_o(r-R)]\right|^2 dr}, \tag{II.14}$$

where $\eta = O(1)$. The expression in the numerator quantifies the field mismatch near the interface. The condition $\Delta \ll 1$ constitutes a criterion for the validity of our approximation. For example, when $\eta = 3$, $\epsilon_i = -15$, and $\epsilon_o = 1$, $\Delta^2 = 0.002$ for $\omega R/c = 800$, rendering our result applicable. On the other hand, for $\omega R/c = 100$

we obtain $\Delta^2 = 0.3$, indicating that the approximation is less reliable now, hence the coupling to non-fundamental modes can no longer be neglected.

When the single-mode approximation is not appropriate, it is still possible to derive a physical quantity from the above analysis. As discussed previously, the mode index m associated with the fundamental mode has the smallest imaginary part compared to the mode indices of non-fundamental modes. Since the wave depends on n as $\exp[\pm in\phi]$, modes with large $\mathrm{Im}[n]$ decay rapidly. Thus, the transmission in the presence of coupling to nonfundamental modes does not exceed the upper bound of

$$\mathsf{T}_u = \exp(-2\mathrm{Im}[m]\theta). \tag{II.15}$$

Here we neglect reflections at the x_1 and x_2 boundaries, thus excluding interference effects. Figure 8(a) is a plot of T_u as function of R. A peak is clearly visible, moving to higher values of R as the wavelength increases. To the right of the peak, at large radii of curvature absorption losses in the metal dominate, and the maximum transmittance decreases with increasing radius. To the left of the peak radiation due to the high curvature is the dominant loss mechanism, leading to a rapid drop in T_u. At very high curvature ($R \leq 10\mu$m) there is a change in trend, and T_u starts to *increase* with decreasing R. When calculating the radiation loss per arclength, we find that for this range of radii it increases slower than elsewhere, allowing T_u to increase even as R attains very small values.

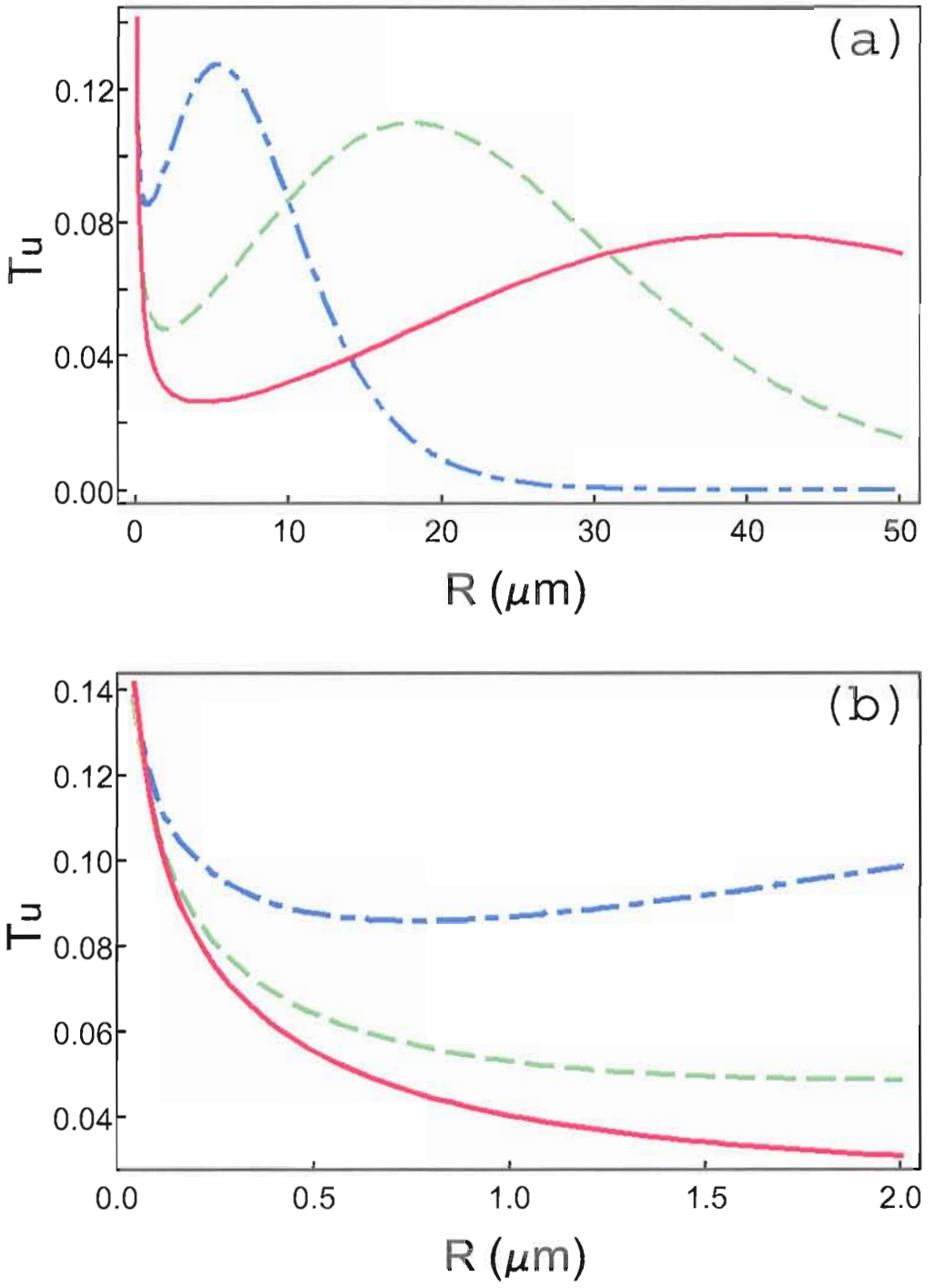

FIGURE 8. (a) The upper bound for the transmittance, T_u, plotted for a silver-air interface with bend angle $\theta = 90°$, as function of bend radius R for wavelengths $\lambda = 500$nm (dashed-dotted line), $\lambda = 600$nm (dashed line), and $\lambda = 700$nm (solid line). (b) Magnified view of the upper bound in the diffraction-dominated regime.

The behavior of the transmittance for very high curvature is a consequence of diffraction of the incident SPPs. In general, diffraction is associated with the finite wavelength of light, and the diffraction coefficient approaches zero in the limit of small wavelength[71]. For SPPs propagating around bends, a decrease in the radius of curvature is equivalent to an increase in the effective wavelength, λ/R. For this reason, SPP diffraction around a corner increases as R decreases, resulting in greater transmittance for smaller R. Since the diffraction is only significant at sharp corners, the transmittance becomes weakly dependent on the dispersion of the metal at small radii of curvature. Hence, as shown in Fig. 8(b), the upper bound at different wavelengths converges to a single value as R approaches zero.

From the discussion above, it is clear that the nonmonotonic behavior of the transmittance is a result of three competing mechanisms: absorption, radiation, and diffraction. Depending on the radius of curvature, one of the three mechanisms becomes dominant, creating three distinct regimes in Fig. 8(a). However, it is not possible to evaluate the potential discrepancies between the upper bound model plotted here and the analytical results, since our analytical approach is not valid at high curvatures. To examine the transmittance for such cases, we turn to a numerical study using the finite-difference time-domain method (FDTD).

Comparison between Analytical Results and FDTD Calculations

We apply here numerical FDTD calculations to study the propagation of SPPs about bends, and compare with our analytical results. Previously, the method of lines has been used to study the diffraction and the propagation of SPPs at a sharp bend with $R = 0$[72]. Our present numerical study examines how the transmission efficiency depends on the radius of curvature of the bend. The dielectric function in our simulations is given by the Debye model

$$\epsilon(\omega) = \epsilon_\infty + \frac{\epsilon_s - \epsilon_\infty}{1 - i\omega\tau} + i\frac{4\pi\sigma}{\omega}. \tag{II.16}$$

With the choice of parameters $\epsilon_\infty = 3.90838$, $\epsilon_s = -25658.4$, $\tau = 1.20973 \times 10^{-14}$sec, and $\sigma = 1.68931 \times 10^{17}\text{sec}^{-1}$ the Debye model closely matches experimentally obtained values for silver[73] in the wavelength range 400–1200nm. We implement a nonuniform orthogonal grid, with mesh size in the range $\lambda/300$–$\lambda/40$. Dispersive perfectly matched layers[74] are used as absorbing boundary conditions throughout our study. The wavelength in vacuum is fixed at $\lambda = 630$nm. A trial simulation of SPP propagation at a planar metal–air interface indicates that the simulated SPPs are well characterized by the effective dielectric constant $\epsilon_s = -14.0 + i0.9$, which is reasonably close to $\epsilon = -15.7 + i1.1$ calculated using the Debye model. A detailed discussion of the FDTD methods employed to simulate the SPP propagation is presented in Appendix A.

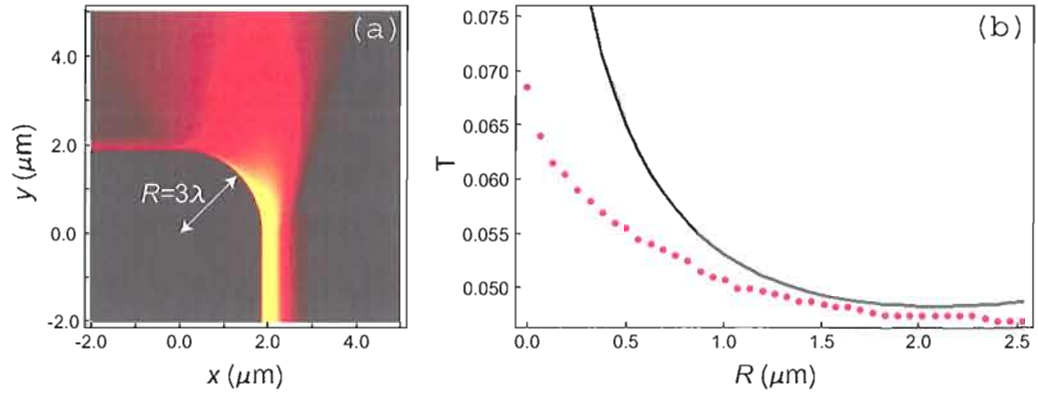

FIGURE 9. (a) FDTD simulation of SPP propagation around curved metal bends for $\lambda = 630$nm. The SPPs are incident from the bottom and propagate counterclockwise around the bend. (b) Analytical result for the transmittance upper bound (black trace) compared to numerical simulations for various values of R (red points). The upper bound values are clearly higher than the simulation results, confirming the consistency of our analytical method.

Ninety-Degree Bend

A series of FDTD simulations were performed to analyze propagation about the 90° rounded edge shown in Fig. 9(a). The transmittance, T, is extracted for various radii of curvature. As shown in Fig. 9(b), the transmittance *increases* with decreasing radius, peaking at $R = 0$ with $\mathsf{T} \approx 0.07$. Hence, the numerical approach confirms the diffraction-dominated small-radius behavior of T predicted from our earlier analysis of T_u in Fig. 8. Interestingly, our simulations reveal that the actual transmittance is reasonably well described by the upper bound (calculated now using ϵ_s) even for $R \leq \lambda$. Moreover, for $R > \lambda$ the discrepancy between the simulation and the analytical upper bound is less than 0.01. This mismatch is expected to decrease even further with decreasing curvature because the coupling to the fundamental mode increases as

$\lambda/R \rightarrow 0$. We therefore conclude that the calculated upper bound is a good estimate for the transmittance for all $R \geq \lambda$.

Bend with Negative Curvature

The analytical formalism developed above may also be used to analyze the *reversed geometry*, where the metal occupies the outer space, and the SPPs propagate around a dielectric void in it as shown in Fig. 4(c). In this complementary picture the planar SPP modes are now matched to the solutions of a *hollow cylindrical void* in the metal. However, care must be taken when choosing the appropriate solutions in region II for the mode matching. For a dielectric cylinder surrounded by metal, the radial solutions in the dielectric are the Bessel functions. These functions, except for the one confined to the interface, have field nodes. Since the existence of nodes implies that photons are exchanged between opposing points on the cylindrical interface, these solutions are unphysical in an open geometry such as our system. Therefore, the only solution represented by the Bessel function in region II is the surface confined mode, which lacks any nodes.

As before, the surface confined mode corresponds to the fundamental (SPP) mode, which minimizes the field mismatch with the incident planar SPP under the single-mode approximation. Since the fundamental mode is represented by the Bessel function, Eq. (II.3) remains unchanged and the expressions for the transmittance and the reflectance are valid for this reversed geometry. Our calculations have shown that this problem is now appropriately analogous to the finite potential barrier model.

We also find that the absorption loss in region II is now greater than the absorption of planar SPPs. From the argument above, it also follows that in the single-mode approximation SPP propagation around a bend is *nonradiative*. For this reason, SPP transmission through the reversed geometry becomes highly efficient when material losses and reflections at the boundaries are negligible.

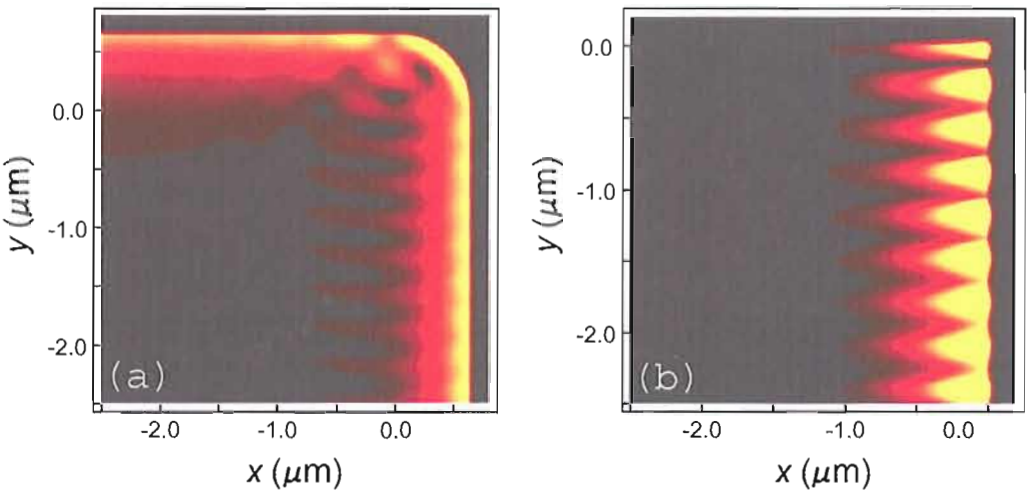

FIGURE 10. FDTD simulation of SPPs propagating around negative curvature bends for (a) $R = \lambda = 630$nm and (b) $R = 0$ when SPPs, incident from the bottom, propagate around a circular dielectric void. The radiation loss is significantly reduced compared to the propagation around a metallic bend.

Our simulations show that efficient propagation is indeed possible. For example, we find that when $R = \lambda$ the transmittance is $\mathsf{T} = 0.73$, in sharp contrast to the value of $\mathsf{T} \approx 0.06$ obtained for an equivalent curvature in the geometry of Fig. 9(a). However, when $R = 0$, back-reflection at the bend becomes the dominant loss mechanism with $\mathsf{R} = 0.96$, while the radiation loss remains small as shown in Fig. 10(b). The transmittance decreases to $\mathsf{T} \approx 0.002$. Because of its high reflectance,

this particular geometry is essentially a SPP mirror and may be implemented to construct SPP resonators[75].

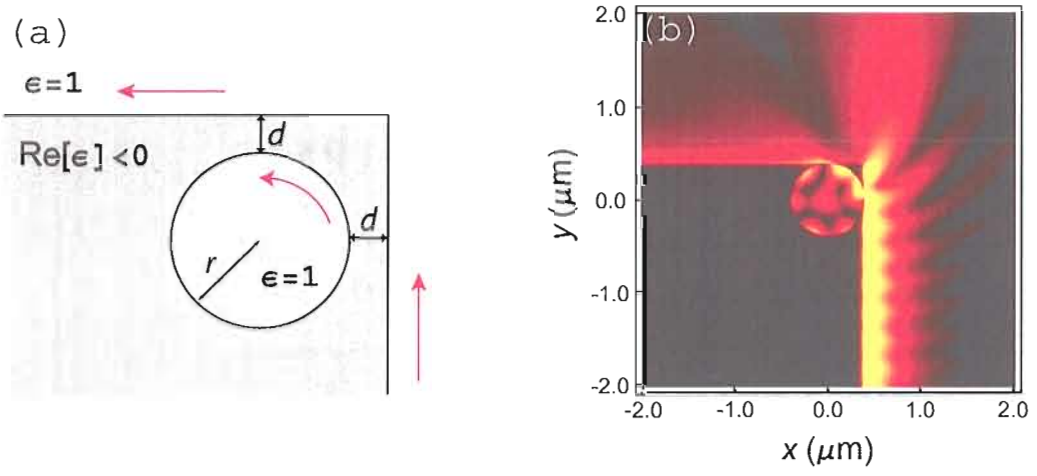

FIGURE 11. (a) Schematic diagram of a SPP microresonator embedded near a sharp edge. SPPs are incident from the bottom along the direction of the red arrow, couple to the resonator and couple out again. (b) Numerical FDTD simulation showing the magnitude of the magnetic field for $d = 8.4nm$ and $r = 378nm$. A significant portion of the field is seen to couple into the resonator.

Resonator-Enhanced Transmission around a Sharp Bend

We have shown that efficient transmission of SPP energy around bends is possible when propagating around small voids in metals, while SPP propagation about metallic bends is highly radiative. In what follows we demonstrate a method for reducing radiation losses by introducing an additional metal-dielectric interface into the system, which provides an alternative, low-loss transmission channel for SPPs. Consider the geometry shown in Fig. 11(a). A cylindrical hole of radius r is placed in close proximity to two flat metal interfaces joined by an abrupt 90° edge. Incident SPPs

propagating upward along the vertical interface are coupled through their near-fields into the void and our of it onto the second interface. Positioning of the resonator within the skin depth of the metal allows efficient excitation of the resonator modes by the incident SPPs, and subsequent outcoupling. The role of the dielectric void is similar to that of a dielectric microring resonator, and the evanescent wave coupling scheme is analogous to optical coupling between microring resonators and dielectric waveguides[76]. The SPP resonator provides an alternative transmission channel into which the field couples, leading to a reduction in the total SPP energy impinging on the highly radiative sharp edge. Hence, the efficiency of propagation increases significantly when a resonator is properly incorporated into the metal in the vicinity of the bend. Figure 11(b) shows the results of a simulation for a typical resonator-coupled system. We find that the transmission around an infinitely sharp bend in the absence of a resonator, ($\mathsf{T} \approx 0.07$) increases to $\mathsf{T} = 0.17$ when a cavity of radius $r = 378nm$ is incorporated at a distance $d = 8.4nm$ from the interfaces. A scattering-theory formalism has been previously developed to treat waveguide-resonator couplings[77, 78]. However, this method requires ab-initio knowledge of the scattering-matrix elements, attainable by solving Maxwell's equations using FDTD or other numerical methods. When applied to the geometries of our system, we find that this approach is less straightforward than our demonstrated method of extracting the transmission efficiency directly from FDTD simulations of resonator-coupled interfaces. The transmitted signal levels may be then optimized by fine-

tuning additional parameters of the system, such as resonator shape, the number of (cascaded) resonators and their relative positioning near the bend. In addition, incorporating a gain medium[29, 30] (i.e. SPP *amplifier*) inside the resonator cavity may further enhance transmission efficiencies. Future work will address the enhanced transmission via SPP resonators in detail.

Conclusions

In summary, we have studied the propagation of SPPs at a curved metal-dielectric interface both analytically and numerically. We have presented and confirmed a physically intuitive picture of the bend-induced radiation, and how the radiation loss is related to the SPP confinement at the interface. In the short wavelength limit, we have shown that calculating the propagation efficiency is analogous to a quantum mechanical 1D finite square well which is readily solved to obtain the expressions for energy transmission and reflection coefficients. The analysis of the upper bound on the transmittance has revealed that absorption, radiation, and diffraction are three competing mechanisms, responsible for the nonmonotonic behavior of the transmittance. Furthermore, our numerical study has shown that the calculated upper bound T_u is a good estimate for the actual transmittance for all bend radii $R \geq \lambda$. In the complementary reversed geometry, when the SPPs propagate around a dielectric void, it is argued that the fundamental mode is nonradiative, and thus SPP propagation is overall less radiative. This prediction was verified numerically. Finally,

we have studied a bend geometry in which a surface plasmon resonator is introduced to provide an alternative transmission channel for enhancing the propagation efficiency.

CHAPTER III

OPTICAL PROPERTIES OF RANDOM METAL-DIELECTRIC FILMS

Realistic metal surfaces are never perfectly flat, and are always rough to some degree. Thus, a thorough understanding of how surface roughness affects the SPPs and the optical properties of metal-dielectric systems in general is critical in plasmonics. In this chapter, we shift our focus from SPPs on curved metal surfaces to the optical response of rough metal-dielectric films. In particular, we focus our attention on how surface roughness affects the optical properties and SPPs of disordered metal-dielectric composites. The outline of this chapter is as follows. We first review the concept of random composites as metamaterials in the introductory section. In the second section, we report a study on a reflection asymmetry from rough metal-dielectric films, which was previously published with A. Chen, V. A. Podolskiy, and M. Deutsch in Ref. [60]. My specific contribution to this work was to perform the numerical modeling of the random composites. Subsequently, we describe the inadequacies of effective medium theories to describe our observations. We then present our recent investigation on the effect of surface morphology on the optical properties of random metal-dielectric composites. Conclusions are given in the final section.

Introduction: Random Metal-Dielectric Composites as Metamaterials

As was discussed in Chapter I, metamaterials are a class of artificial composites designed to produce an engineered electromagnetic response, often described in terms of effective permittivity and permeability. Metamaterials can be comprised of ordered or disordered arrays of subwavelength elements. The scientific studies of a disordered metal-dielectric composites as metamaterials date back over 100 years. In 1904, J. C. Maxwell Garnett developed an effective medium theory (EMT) to explain bright colors observed in metal doped glasses, such as the stained glass windows found in churches and cathedrals. According to the Maxwell-Garnett (MG) theory, the effective permittivity of an heterogeneous structure made of small spherical particles in a host medium is given by

$$\epsilon_{MG} = \epsilon_2 \frac{\epsilon_1(1+2p) + 2\epsilon_2(1-p)}{\epsilon_1(1-p) + \epsilon_2(2+p)}, \tag{III.1}$$

where f is the filling fraction of the spheres, and ϵ_1 and ϵ_2 are the permittivities of the inclusions and the host, respectively[79]. The MG theory is derived with an assumption that the coupling between the spheres can be neglected, and hence, is valid only for small filling fractions. Another commonly used EMT is the Bruggeman (BR) theory, according to which the effective permittivity ϵ_{BR} is determined by[80]

$$p\frac{\epsilon_1 - \epsilon_{BR}}{\epsilon_1 + 2\epsilon_{BR}} + (1-p)\frac{\epsilon_2 - \epsilon_{BR}}{\epsilon_2 + 2\epsilon_{BR}} = 0. \tag{III.2}$$

The BR theory treats two media symmetrically, and is applicable for a wider range of filling fraction. In general, EMTs use a quasistatic approximation and assume

that the inclusions are much smaller than the wavelength. This renders the effective permittivity independent of particle size as is evident in Eq. (III.1) and (III.2). As a result, it essentially ignores the effect of different roughnesses that may arise at the surface of the heterogeneous material due to different inclusion sizes.

Over the years, the MG and BR theories and their modified versions have been employed to describe various experimental results. For example, a number of studies have shown that the EMTs and their modified versions agree reasonably well with the transmission and reflection spectra of light from semicontinuous metal films on substrates[81–85]. Interestingly, the EMTs have only been used to model the reflectance from one side of the films. In fact, to our knowledge, the reflectance of light from *both* sides of random metal-dielectric films have never been investigated. As a first step toward understanding the effect of surface roughness, in the next section we present a study of a reflection asymmetry from semicontinuous metal films. We then test if any EMT, which ignores the effect of surface roughness, can adequately explain our experimental results.

Asymmetric Mirrors

The reflection spectra from two sides of a film are symmetric in most textbook examples; that is, $\Delta R \equiv R_1 - R_2 = 0$ where R is the reflectance and the subscripts refer to the direction of the incident light. However, if a system lacks inversion symmetry and is lossy (either in the form of absorption or diffusive scattering

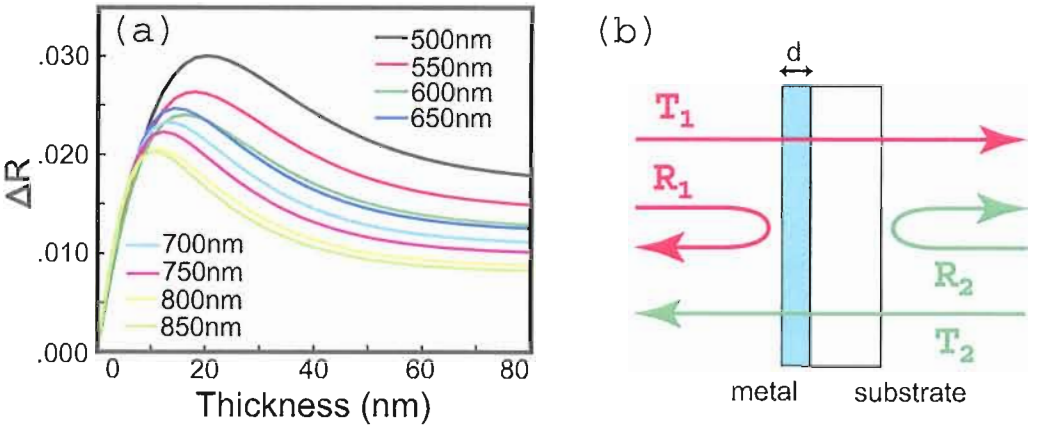

FIGURE 12. (a) Calculated ΔR from a smooth silver film on a glass substrate as a function of the metal thickness d. (b) A schematic diagram of the film, defining the direction of the incident light.

induced by surface roughness or material inhomogeneity), then the reflectance can be asymmetric. For instance, a smooth layer of silver on a glass substrate has $\Delta R \sim 2\%$ as shown in Fig. 12(a). The system is known as the asymmetric mirror if in addition the transmittance T of the film is nonzero[86]. The energy conservation dictates that $T + R_{1,2} + A_{1,2} = 1$, where A is the losses. Therefore, $\Delta R = -\Delta A$, and the reflection asymmetry is a direct measure of difference in the losses. Note that the reciprocity guarantees that the transmittance is symmetric; $\Delta T \equiv T_1 - T_2 = 0$. See, for example, Ref. [87] for detailed discussions of the optical reciprocity.

In our experiment, asymmetric mirrors consist of semicontinuous silver films deposited on 1mm thick glass substrate using a modified Tollen's reaction[88]. The amount of silver deposited was controlled by varying the deposition time between 1 to 6 hours. Figure 13(a) and (b) show high-resolution scanning electron microscope (SEM) images of typical samples. The images are taken with a Zeiss Ultra SEM,

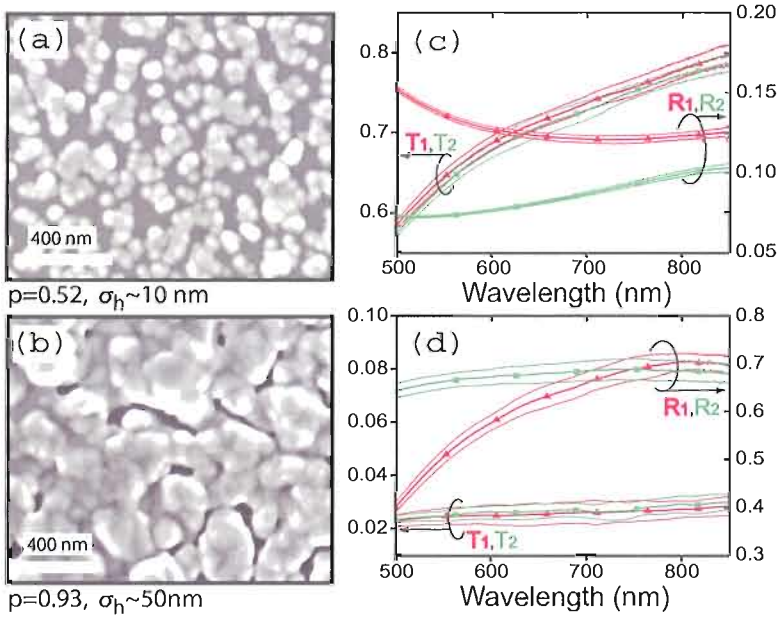

FIGURE 13. Reflection asymmetry from semicontinuous films. Left: SEM images of typical samples with $p = 0.52$ (a), and $p = 0.93$ (b). Right: Measured $T_{1,2}$ and $R_{1,2}$ of the samples.

and are used to measure the metal filling fraction p of the samples. The statistical information of the surface, such as the root mean square (rms) of the height variation σ_h, is obtained from atomic force microscope (AFM) images taken with a Digital Instruments MultiMode scanning probe microscope.

The reflection and transmission spectra were taken using an inverted optical microscope with a 10X objective (0.25 N. A.), coupled to a Horiba-Jobin-Yvon Triax320 spectrometer and a liquid-nitrogen-cooled Spectrum One CCD detector. White light from a tungsten-halogen source was incident normally on the samples. The reflectance was normalized by using two mirrors (Newport Broadband SuperMirror and UV Enhanced Aluminum Mirror) to cover wavelength ranging from

400nm to 850nm. Optical data was collected over $\sim$ 1mm across the sample to average out local inhomogeneities. The reflection and transmission spectra of the samples are shown in Fig. 13(c) and (d). The subscripts 1 and 2 refer to when light is incident from the air-silver and substrate-silver side, respectively. In addition, Fig. 14 shows a plot of ΔR vs p. The samples exhibit broadband reflection asymmetries, the signs of which can be both positive and negative. The absolute value of ΔR can be an order of magnitude greater than that of a smooth silver film, and especially large ΔR is observed for high filling fraction samples. A large ΔR has also been observed from ordered metamaterials, however, over a narrower spectral range[89, 90]. Remarkably, ΔR is nearly dispersionless (i.e. independent of the wavelength) for the sample with $p = 0.74$.

Inadequacies of Effective Medium Theories

If the reflection asymmetry can be modeled with an EMT, then there must be an effective dielectric function ϵ_{eff} that can simultaneously fit T, R_1, and R_2 reasonably well. By solving Maxwell's equations for a triple layered system with smooth interfaces, we obtain

$$T = \frac{n_3}{n_1}\left|\frac{t_{12}t_{23}e^{i\phi_2}}{1+r_{12}r_{23}e^{2i\phi_2}}\right|^2 \quad \text{(III.3)}$$

$$R_1 = \left|\frac{r_{12}+r_{23}e^{2i\phi_2}}{1+r_{12}r_{23}e^{2i\phi_2}}\right|^2 \quad \text{(III.4)}$$

$$R_2 = \left|\frac{r_{32}+r_{21}e^{2i\phi_2}}{1+r_{32}r_{21}e^{2i\phi_2}}\right|^2 \quad \text{(III.5)}$$

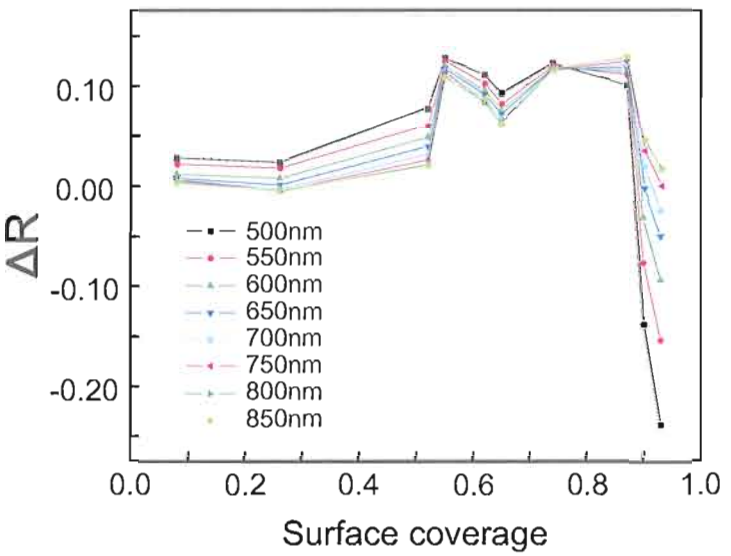

FIGURE 14. Dependence of the reflection asymmetry on the filling fraction. The sign of ΔR can be positive or negative, and the absolute value of ΔR can be an order of magnitude larger than that of a smooth silver film.

where $t_{ij} = 2n_i/(n_i + n_j)$, $r_{ij} = (n_i - n_j)/(n_i + n_j)$, $\phi_2 = n_2\omega d/c$, and n_i is the refractive index of the i-th medium. We numerically invert the expressions and use the measured values of T and R_1 to calculate the real and imaginary part of ϵ_{eff}. The film thickness d was used as a fitting parameter to obtain the best fit for R_2. Here, we ignore the interference effect from the finite thickness of the substrate since the interference fringe spacing is significantly smaller than the spectral resolution of our setup (0.1nm vs 0.5nm). However, we have taken the 4% reflection from the air-substrate interface into consideration when deriving ϵ_{eff}.

In Fig. 15(a), we plot ϵ_{eff} for the sample shown in Fig. 13(b). The best fit for R_2 is obtained when the film thickness is $d = 440$nm, which is several times greater

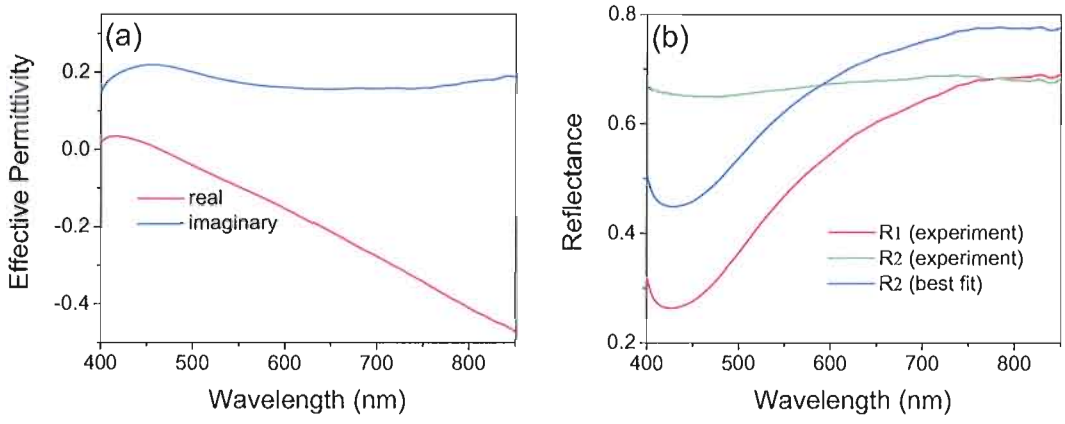

FIGURE 15. Effective permittivity fit. (a) The real and imaginary part of the effective dielectric function calculated from T and R_1. (b) A comparison between the experimental and the theoretical R_2.

than the rms height of 50nm. The calculated and the measured R_2 are shown in Fig. 15(b). From the graph, it is evident that even the best-fit R_2 with such unphysical value of d does not agree well with the measured R_2 Our analysis yields similar results for other samples with different surface coverage. Therefore, we conclude that semicontinuous films cannot be described by *any* EMT that is based on the smooth interface assumption. Surface roughness cannot be ignored.

As an aside, we note that although EMTs cannot describe our observations, it may be possible to use the EMTs as qualitative guidelines for designing asymmetric mirrors. For example, suppose we are interested in fabricating an asymmetric mirror exhibiting a dispersionless asymmetry with $\Delta R = 0.12$ when $d = 50$nm. Without specifying the transmittance, inverting the expressions for R_1 and R_2 yield the effective permittivity shown by the solid lines in Fig. 16(a). The plot of ΔR vs

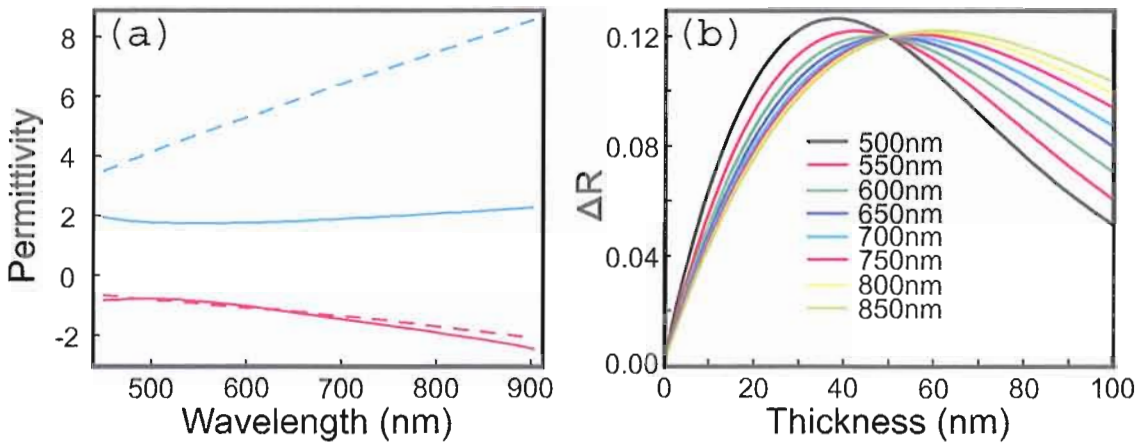

FIGURE 16. Effective permittivity modeling. (a) Solid lines: real (red, lower) and imaginary (blue, higher) parts of the effective permittivity obtained by numerically inverting R_1 and R_2. Dashed lines: the effective permittivity according to the BR theory. (b) The reflection asymmetry as a function of film thickness d.

d calculated from the derived effective permittivity is shown in Fig. 16(b), and it illustrates that the reflection asymmetry resembles that of the semicontinuous films shown in Fig. 14. Comparison with the EMTs indicates that the real part of the derived permittivity is in excellent agreement with that of the modified BR theory with $p = 0.71$[80, 81]. As discussed in the previous section, the semicontinuous film with $p = 0.74$ exhibit a nearly dispersionless asymmetry with $\Delta R \approx 0.12$. Therefore, while there is a significant discrepancy in the imaginary part, the filling fraction set by the EMT may be used as a starting point for fabricating the desired asymmetric mirror. For further discussion, see Ref [60].

The Effect of Surface Morphology

In the previous section, we have demonstrated that the surface roughness of the semicontinuous films influences their optical properties. However, it is not yet apparent *how* their roughness and surface morphology affect the reflectance and the transmittance. Moreover, it is not clear what physical mechanisms are responsible for the large broadband ΔR, or how they are related to the surface morphology of the disordered metallodielectric films. From a practical point of view, understanding the mechanisms behind the asymmetry is important in order to design and optimize the metamaterials for practical applications such as Fabry-Perot interferometers [91]. More fundamentally, understanding how surface morphology affects the reflection spectra is the first step toward understanding the optics of the disordered metallodielectric films and how the different morphology created, for instance by different deposition methods, can influence their optical properties. In this section, we present a study of the effect of the surface morphology on the reflection asymmetry from disordered metallodielectric films.

Disordered silver films of various surface coverage are fabricated using the same chemical-deposition method as above. However, for the present study, the silver is deposited on $15\text{mm} \times 15\text{mm} \times 0.15\text{mm}$ glass cover slips. Unlike the previous samples, the reaction is carried out at room temperature resulting in larger silver grains. This deposition method is developed and refined by S. Peterson, and the details can be

found in Ref. [92]. The amount of silver deposited is controlled by varying the deposition time between 5 to 25 minutes. The average mass thickness d_m is obtained from the mass of deposited silver measured with a Sartorius ME5 Microbalance. Figure 17(a) shows a high-resolution SEM image of a typical sample.

In order to study how surface morphology influences the reflection asymmetry, we induce morphology change by annealing the samples in ambient for 2 hours at temperatures ranging from 70°C to 220°C using a Barnstead Thermolyne F79300 tube furnace. SEM images are taken to observe changes in the morphology. Furthermore, to detect changes that are not observable under the SEM, the sheet resistance R_s of the film is measured by the van der Pauw method[93] using a Keithley 2004 SourceMeter.

SEM images in Fig. 17(a)–(d) show typical morphologies of a sample with $d_m =$ 101nm before and after annealing at various temperatures. No surface morphology change is detected with the SEM and the sheet resistance measurement below 70°C. At 70–80°C, the sheet resistance starts to decrease. This is associated with a removal of defects and vacancies within the silver crystallites[92]. SEM images indicate that the filling fraction also decreases slightly. As the annealing temperature increases, the sheet resistance continues to decrease. At $\sim$ 100°C, the resistance begins to increase while the surface coverage keeps decreasing due to the dewetting of the silver films. Annealing at a higher temperature further dewets the samples and smoothes the silver grains. At $\sim$ 220°C, the films dewet completely as shown in the environmental SEM image in Fig. 17(d), obtained using a FEI Quanta ESEM.

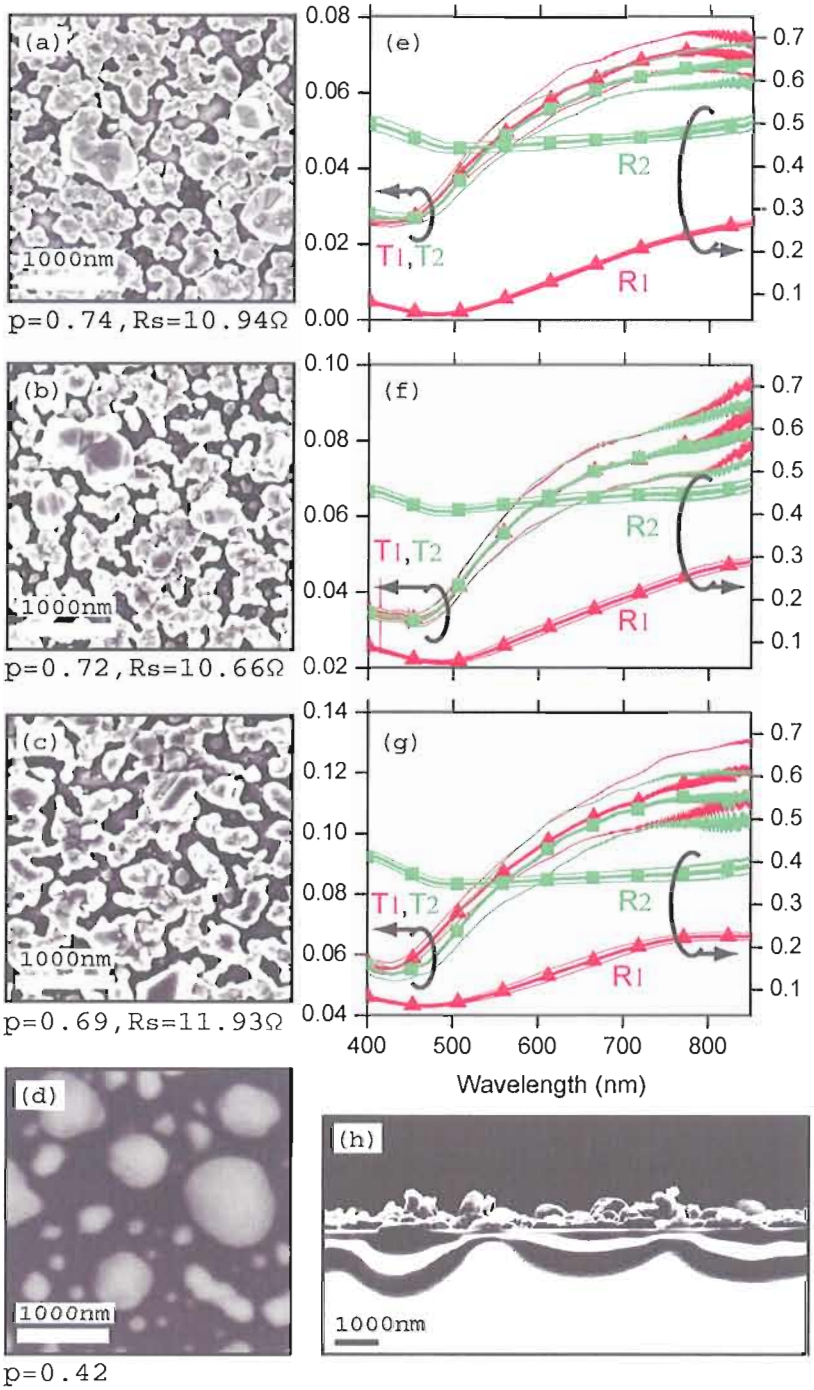

FIGURE 17. Effect of annealing on the asymmetric mirrors. Left: SEM images of a sample at different stages of annealing: (a) before annealing, (b) 80°C, (c) 170°C, (d) 220°C. Left: Measured $T_{1,2}$ and $R_{1,2}$ of the film: (e) before annealing, (f) 80°C, (g) 170°C. (h) a side view image of a typical sample.

The reflection and transmission spectra of the sample are shown in Fig. 17(e)–(g). The sample exhibits a large, negative reflectance asymmetry, between $\Delta R \sim -40\%$ and -20%. The transmittance spectra are always symmetric as before. Below $\sim$ 220°C, the shape of $R_{1,2}$ and $T_{1,2}$ are insensitive to the changes in morphology induced by annealing. We observe that R_2 is relatively flat, and its overall level decreases monotonically with increasing annealing temperature. These observations indicate that the reflectance from the substrate-silver side is dominated by a specular reflection of the incident light from the bottom surface of silver grains for the following reasons: As the annealing temperature increases, the filling fraction decreases. Therefore, a smaller fraction of the incident light is reflected from the bottom surface of the grains as a specular reflection. This also causes the sample to essentially act as a "poor" mirror, which explains the weak dependence of R_2 on the wavelength. To test this hypothesis, we compared R_2 of a sample before annealing with that of another sample with significantly greater mass thickness. In order to match their filling fractions, the second sample was annealed at 170°C. As shown in Fig. 18, two reflectance spectra are well within their errors even though the amount of silver deposited on the samples differs by nearly 60%.

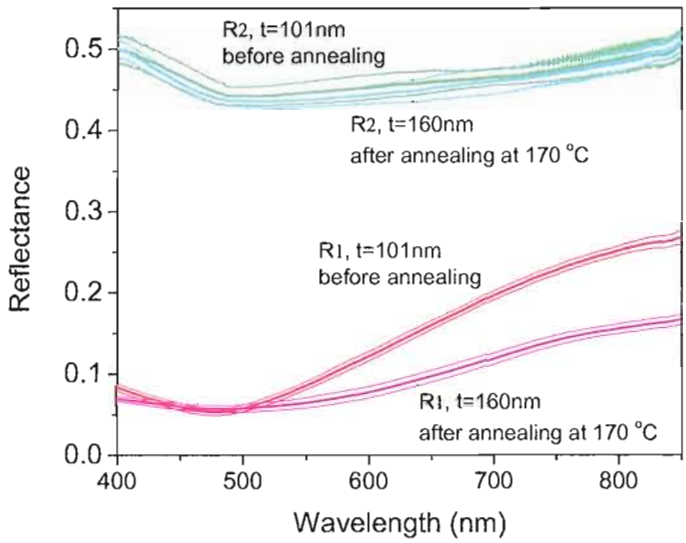

FIGURE 18. Reflection spectrum comparison of two samples with significantly different mass thickness (d_m = 101nm and d_m = 160nm). The sample with higher larger thickness was annealed at 170°C, such that the two samples have similar surface coverage ($p = 0.74 \pm 0.02$ and $p = 0.76 \pm 0.03$).

Unlike R_2, R_1 dips near $\lambda \approx 480$nm, and increases monotonically for longer wavelength. Moreover, compared to R_2, the overall level of R_1 is significantly less sensitive to the annealing. The side view image of a sample taken with SEM in Fig. 17(h) clearly shows that the film is considerably rougher on the air-silver side. According to the Rayleigh criterion[94], a surface is considered optically rough (smooth) if the root mean square height, σ_h, is greater (smaller) than $\lambda/8\cos\theta_i$, where θ_i is the angle of incidence. AFM measurements of the surface profile of the air-silver side indicate $\sigma_h \approx 110$nm. As a result, the sample is at the smooth-rough transition in the wavelength range, and we expect both the specular reflection

and nonspecular diffusive scattering to be significant when light is normally incident from the air-silver side. Since the surface appears smoother on the substrate-silver interface, we also predict a significantly smaller diffusive scattering when the light is incident from that side. The specular reflection from the air-silver side increases with the wavelength since the surface is relatively smoother for longer wavelength. As the sample is annealed, its surface profile changes. However, since the amount of silver on the surface is unchanged and the filling fraction does not change drastically, change in σ_h should be slight, causing R_1 to be less sensitive to annealing.

Note that although the average silver grain sizes differ, the general shapes of R_1 and R_2 here resemble the reflection spectra from the high filling fraction sample studied in the previous sections (see Fig. 13(d)). Therefore, the analysis above is likely to apply to the reflection asymmetry from the sample composed of smaller silver particles. However, the same interpretation would not apply for low filling fraction shown in Fig. 13(a), as its reflection from the air-silver side is *greater* than that from the substrate-silver side. Further study is necessary to investigate what physical mechanisms are responsible for creating a positive ΔR.

In order to test our prediction regarding the diffusive scattering and to investigate the effect of surface roughness further, we performed an angular-resolved experiment to compare the amount of diffusive scattering from the two sides of the film. The experimental setup was built by C. Rohde, and the details can be found in Ref. [95]. The source was a p-polarized helium-neon laser ($\lambda = 633$nm) with the incident angle

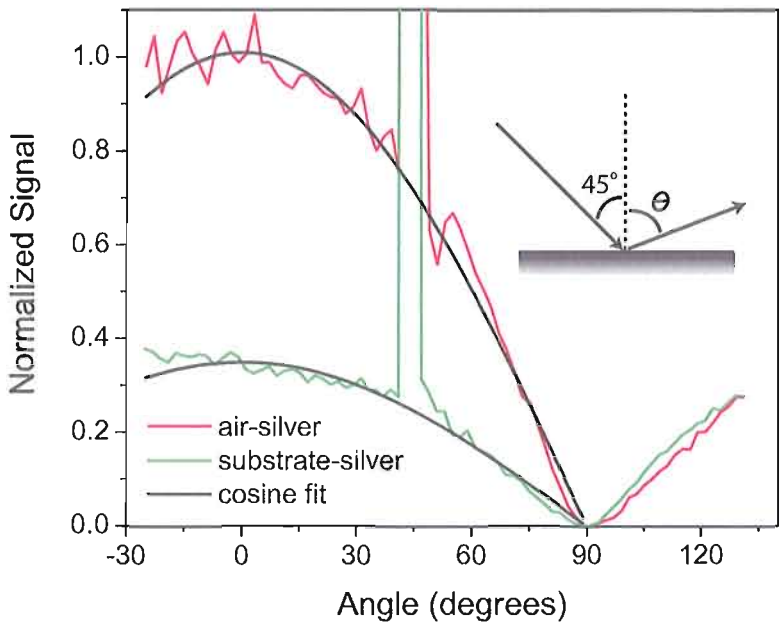

FIGURE 19. Diffusive scattering measurement from the air-silver side (red) and the substrate-silver side (green) of the asymmetric mirror. The source was a p-polarized helium-neon laser ($\lambda = 633$nm) with the incident angle set at $\theta_i = 45°$.

set at $\theta_i = 45°$. An off-normal incident angle was chosen such that the source was not blocked by the detector when scanning near the specular reflection. Figure 19 shows a plot of the diffusing scattering signal as a function of the scattering angle when the light is incident from the air-silver side and the substrate-silver side. The scattering angle is measured with respect to the surface normal as shown in the inset. Therefore, the spike at $\theta = 45°$ corresponds to the specular reflection. For both sides of the film, the diffusive scattering peaks at $\theta = 0°$, (i.e. in the direction normal to the sample surface), and decreases as the angle approaches 90°. For $\theta < 90°$,

the diffusive scattering from the air-silver side is approximately 3 times larger than from the opposite side. Thus, as predicted, the film behaves as a rough or smooth surface depending on the incident direction, resulting in the reflection asymmetry. A difference in absorption loss could also contribute to the asymmetry. However, as shown in the previous section, no effective permittivity, which ignores the surface roughness, reproduces the measured reflection and transmission spectra. This implies that the surface roughness is critical for the presence of the large asymmetry. The signal is symmetric for $\theta > 90°$ because the scattered light must encounter both rough and smooth sides of the film.

Figure 19 reveals that the diffusive scattering curves agree well with Lambert's Cosine Law. According to the Lambertian model, the radiant intensity of scattered light is proportional to the cosine of the angle between the surface normal and the scattered direction[96, 97]. A Lambertian reflection generally results from multiple scattering of light by inhomogeneities, and is normally considered as volume reflection. Surface reflection, on the other hand, arises from a single scattering of light from the surface, and often preferentially scatters light in directions toward the specular reflection, not toward the surface normal as shown in Fig. 19[94, 97, 98]. Further study is necessary to clarify why a multiple scattering seems to be preferred over a single scattering.

Conclusions

In summary, we have studied the effect of surface roughness on the optical properties of the disordered metal-dielectric films. Semicontinuous silver films of various surface coverage are deposited on glass substrates, and they are shown to exhibit a large broadband asymmetry in reflectance. By inverting the expressions for the transmittance and the reflectance, it has been shown that no EMT, which ignores the effect of surface roughness, can adequately describe the reflection asymmetry. The Rayleigh criterion was applied to show that the large asymmetry is due to the different surface roughness light encounters when incident from different sides of the film. More specifically, it was shown that the air-silver interface is at the smooth-rough transition, and produces significant diffusive scattering and small specular reflection R_1. On the other hand, we identified that R_2 is primarily due to coherent reflection of light from the smooth bottom surface of the silver grains, and hence, depends primarily on the surface coverage. Angle-resolved measurements have revealed that the diffusive scattering obeys the Lambert's cosine law, indicating that multiple scattering is preferred over single scattering from the surface. Much work remains to be done to investigate if SPPs play any vital role in the optical properties of disordered films.

CHAPTER IV

SURFACE PLASMON RESONANCES OF MULTILAYERED METAL-DIELECTRIC SYSTEMS

In recent years, metal nanoparticles and nanoshells have attracted much attention due to their ability to support geometrically tunable SPRs that can be used to control the interaction of light with micro- and nanoscale particles. These SPRs essentially provide a channel through which the incident EM field is efficiently focused to the particles. The geometric tunability and the field enhancement may be improved by increasing the number of metal-dielectric interfaces or by using a metamaterial coating for the layers. In this chapter, we present a study of SPPs on layered metal-dielectric systems. In the first section, we review SPRs of spherical metal particles and of nanoshells. We then present a theoretical study of triple layered metal-dielectric spheres in the second section. We show that when properly designed, the spheres exhibit an enhanced absorption as well as optical transparency that are both tunable over the entire visible range. The work in this section was previously published with C. Rohde and M. Deutsch in Ref [9] and [10]. My specific contribution was to develop a theory of the dispersion engineering and the enhanced absorption for the layered particles, as well as to derive a recursive algorithm for calculating the absorption and scattering cross-sections. Subsequently, we report a study on light scattering from

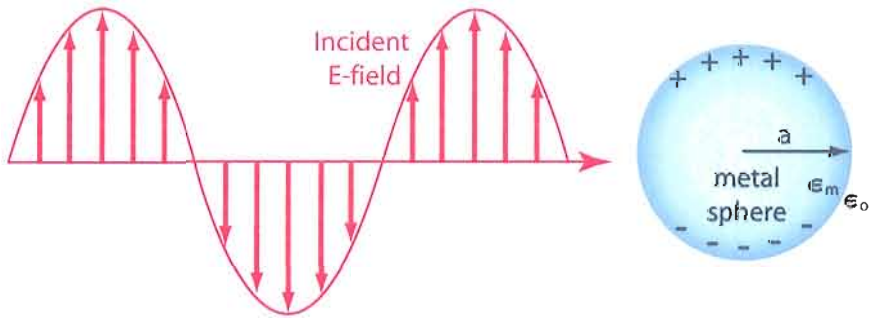

FIGURE 20. Schematic diagram of a dipolar SPR excited by incident light.

semicontinuous silver nanoshells, which was previously published with C. Rohde and M. Deutsch in Ref. [61]. My specific contribution to this work was to collaborate with C. Rohde to develop a theoretical model for describing the dielectric response of the nanoshells. Our findings are summarized in the final section.

Introduction

As discussed in Chapter I, spherical metal-dielectric systems, such as metal nanoparticles and nanoshells, support SPPs that are localized in space. Because of the spherical geometry, the SPPs excited in these systems exhibit multipolar resonances, and they create a large field enhancement near the metal-dielectric interfaces. Moreover, due to the surface curvature, the SPRs are not completely evanescent and are coupled to free propagating EM waves, much like the SPPs propagating around bends discussed in Chapter II. Therefore, unlike SPPs on planar metal-dielectric interfaces, it is possible to excite the localized SPPs directly by light

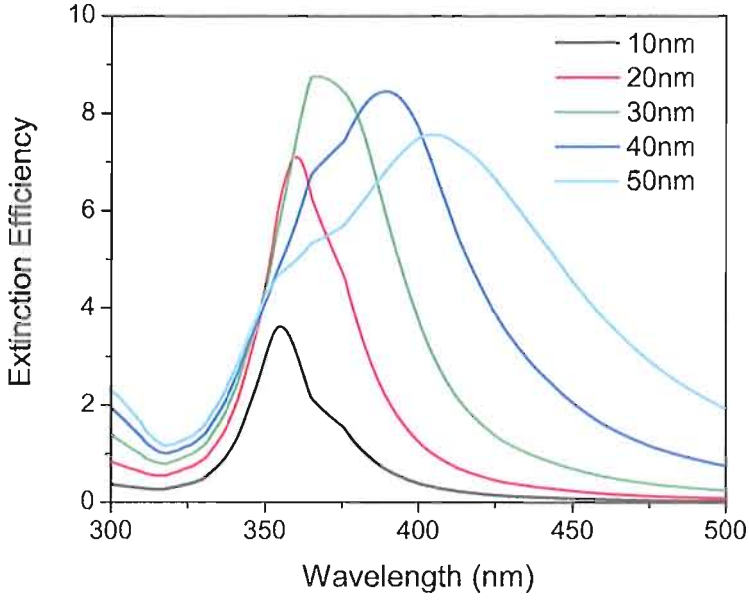

FIGURE 21. Extinction efficiencies of silver spheres of various radii. The extinction efficiency is defined as the extinction cross-section divided by the geometric cross-section.

illumination. Figure 20 shows a schematic diagram of a dipolar SPR of a metal sphere excited by incident light. The interactions of light with the spherical particles are primarily mediated by SPRs. Therefore, the geometric tunability of SPRs can be used to control the particles' optical properties, such as the extinction cross-section.

The extinction cross-section σ_{ext} is defined as the rate of energy absorbed and scattered normalized to incident intensity. When a SPR is excited, the incident light couples strongly to the resonance and an enhanced EM field is established around the particle. The light is then absorbed or scattered, resulting in a peak in the extinction spectrum. Calculated extinction spectra for silver spheres in air are plotted in Fig

21. Although the spheres are much smaller than the wavelength, they exhibit sharp resonances, and the position of the resonance peak varies with sphere radius a. At resonance, the EM energy density near the metal-dielectric interfaces can be orders of magnitude larger than that of the incident light. In the quasistatic limit (i.e. $a \to 0$), the resonant frequencies are determined by

$$\frac{\epsilon_m(\omega)}{\epsilon_o} + \frac{l+1}{l} = 0,$$

where l is a positive integer denoting the multipole number, and ϵ_m and ϵ_o are the permittivities of the metal and the surrounding medium, respectively. Note that realistic metals have complex dielectric functions, $\epsilon_m(\omega)$, and the equation above yields a complex ω. The real and imaginary part of ω determine the resonant frequency and the spectral width of SPRs, respectively. When the sphere is much smaller than the incident wavelength, only the dipole resonance makes a significant contribution to the extinction. By setting $l = 1$ in the equation above, we obtain the resonant frequency for the dipole SPR:

$$2\epsilon_o + \epsilon_m(\omega) = 0.$$

If the $\epsilon_o = 1$ and ϵ_m is given by the lossless Drude model, $\epsilon_m(\omega) = 1 - \omega_p^2/\omega_2$, then $\omega_{l=1} = \omega_p/\sqrt{3}$ where ω_p is the plasma frequency. As a becomes larger, the quasistatic approximation becomes less accurate, and the dipole resonance red shifts and becomes broader. For sufficiently large spheres, contributions from the quadrupole and higher

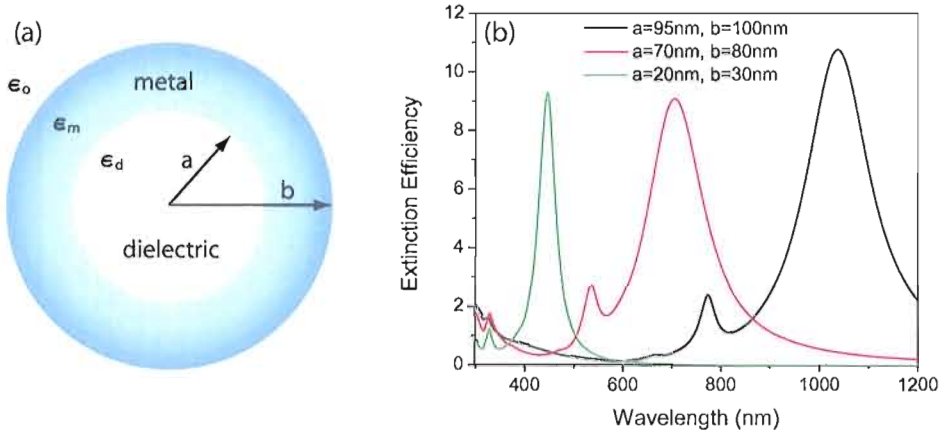

FIGURE 22. (a) Schematic diagram of a nanoshell. (b) The extinction efficiencies of silver-glass nanoshells. Compared to silver spheres, the SPRs of nanoshells can be tuned over a larger spectral range by varying the inner and outer radii.

multipole modes start to appear in the spectrum. For silver spheres, the geometric tunability of the sharp dipole resonance is between $\lambda \approx 350\text{nm}–550\text{nm}$[11].

The geometric tunability can be improved by increasing the number of metal-dielectric interfaces. Nanoshells consist of spherical dielectric cores surrounded by thin metal shells, and their SPRs can be tune over a significantly greater spectral range of geometric tunability as shown in Fig. 22. Studies have found that SPRs of silver and gold nanoshells can be tuned from near-ultraviolet to mid-infrared, or $\lambda \approx 400\text{nm}–9000\text{nm}$[11]. The resonant frequencies of the nanoshell in the quasistatic limit is

$$\left(\frac{b}{a}\right)^{2l+1}\left(\frac{\epsilon_d}{\epsilon_m(\omega)}+\frac{l+1}{l}\right)\left(\frac{\epsilon_m}{\epsilon_o}+\frac{l+1}{l}\right)+\frac{l+1}{l}\left(\frac{\epsilon_d}{\epsilon_m(\omega)}-1\right)\left(\frac{\epsilon_m}{\epsilon_o}-1\right)=0.$$

If $\epsilon_o = \epsilon_d = 1$ and ϵ_m is given by the lossless Drude model, then the expression

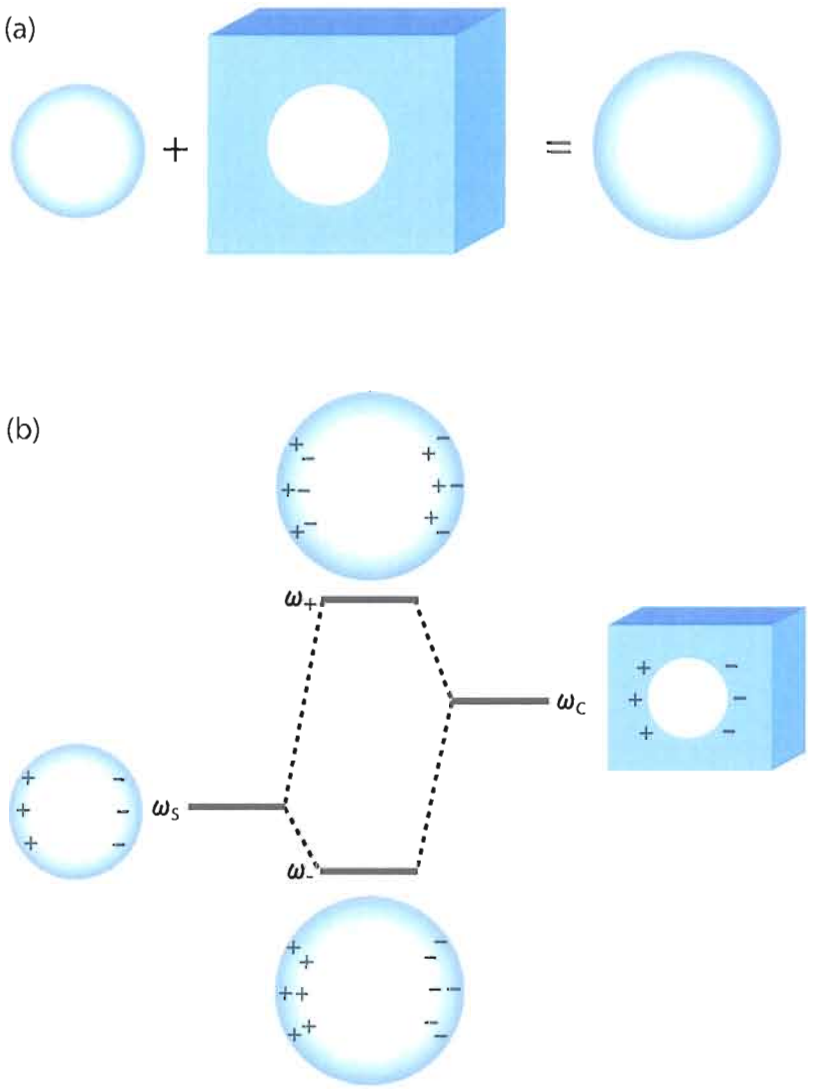

FIGURE 23. Surface plasmon hybridization. (a) A nanoshell can be considered as a hybridized sphere-cavity system. (b) The resonance modes of a nanoshell are due to symmetric and antisymmetric coupling of sphere and cavity modes. The schematic charge distribution is for the dipole modes. However, the same concept applies for higher multipole modes.

simplifies to[7]

$$\omega_{l,\pm}^2 = \frac{\omega_p^2}{2}\left[1 \pm \frac{1}{2l+1}\sqrt{1+4l(l+1)\left(\frac{a}{b}\right)^{2l+1}}\right].$$

The improved tunability of nanoshells is a result of a SPR hybridization as illustrated in Fig. 23. In the hybridization picture[8], the SPRs of the nanoshell are considered as the coupled modes of the sphere and cavity SPRs. Varying the inner and outer radius alters the coupling strength, and hence, the resonant frequencies $\omega_{l,\pm}$. In principle, SPRs of a metal-dielectric system with an arbitrary number of layers can be thought of as multiply hybridized sphere and cavity modes.

The size scale of a typical nanoshell is of the order of 100nm or less, a small fraction of the excitation wavelength. As a result, only a single, low order multipole resonance plays a vital role in channeling the incident EM energy towards the metallic shell. On the other hand, mesoscopic layered particles open up the possibility for simultaneous excitation of a large number of SPRs, further increasing the efficiency of the EM field focusing. This, in turn, enhances optical phenomena such as absorption and nonlinear response. In the next section, we show how to utilize dispersion engineering to enhance the EM field focusing and the absorption cross-section of mesoscopic multilayered spheres. We also show how the spheres exhibit a tunable transparency due to an avoided crossing of plasmonic bands.

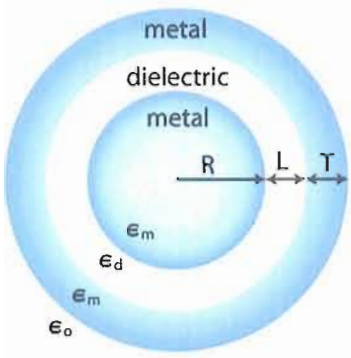

FIGURE 24. Schematic diagram of an MDM sphere. A metal sphere of radius R and permittivity $\epsilon_m(\omega)$ is coated with a concentric dielectric shell of thickness L (permittivity ϵ_d,) which in turn is covered with a concentric metal shell of thickness T and the same permittivity $\epsilon_m(\omega)$ as the core. The layered sphere is embedded in a dielectric host ϵ_o.

Metal-Dielectric-Metal Microspheres

The system consists of a spherical resonator comprised of thin, alternating layers of dielectric and metal shells around a concentric metal core. The composite particle is embedded in a homogeneous, isotropic dielectric host with permittivity ϵ_0. More specifically, we address metal-dielectric-metal (MDM) microspheres: metallic cores comparable in size to optical wavelengths, surrounded by one sequence of lossless dielectric shell of thickness L followed by a metal shell of thickness T. A schematic diagram of a MDM sphere is shown in Fig. 24. We show that it is possible to obtain a band of SPRs with nearly identical resonant frequencies (flat-dispersion band) by adjusting the above geometric parameters. By solving Maxwell's equations using a spherical multipole expansion, we calculate the dispersion relations for the flat band and the resultant enhanced absorption cross-section.

Dispersion Engineering

To analyze the SPRs excited in the system, we initially address the dispersion relations of a simplified geometry in which the outer metal shell is infinitely thick (infinite MDM). This model is complementary to a metal nanoshell on a dielectric core,[43] the DMD. Unlike the DMD, the presence of a properly designed *dielectric* shell in the MDM is necessary and sufficient for achieving a flat-dispersion band.

We first consider a metal characterized by a lossless Drude model, $\epsilon_m(\omega) = \epsilon_b - \omega_p^2/\omega^2$, where ϵ_b is the contribution of inter-band transitions and ω_p is the plasma frequency. The dielectric shell has a real permittivity ϵ_d. The eigenfrequencies of the simplified MDM system are determined by the eigenmode equation[99]

$$\begin{aligned} 0 = & \left\{ \eta \frac{h_l(k_d S)}{h_l(k_m S)} - \frac{[k_d S\ h_l(k_d S)]'}{[k_m S\ h_l(k_m S)]'} \right\} \\ & \times \left\{ \eta \frac{j_l(k_d R)}{j_l(k_m R)} - \frac{[k_d R\ j_l(k_d R)]'}{[k_m R\ j_l(k_m R)]'} \right\} \\ & - \left\{ \eta \frac{j_l(k_d S)}{h_l(k_m S)} - \frac{[k_d S\ j_l(k_d S)]'}{[k_m S\ h_l(k_m S)]'} \right\} \\ & \times \left\{ \eta \frac{h_l(k_d R)}{j_l(k_m R)} - \frac{[k_d R\ h_l(k_d R)]'}{[k_m R\ j_l(k_m R)]'} \right\} \end{aligned} \tag{IV.1}$$

where $\eta = 1$ for transverse electric (TE) modes and $\eta = \epsilon_d/\epsilon_m$ for transverse magnetic (TM) modes, and $k_{m,d} = \sqrt{\epsilon_{m,d}}\ \omega/c$. The radius of the inner metal core is R and $S \equiv R+L$. The spherical Bessel and Hankel functions of the first kind of integer order l are denoted respectively by j_l and h_l, and the prime denotes differentiation with respect to the argument. We limit our discussion to large enough particles, satisfying $1 \ll k_d R$ and $1 \ll |k_m| R$. Thus, the expression above cannot be simplified by using

the quasistatic approximation. Using a real $\epsilon_m(\omega)$ leads to straightforward analytic solutions of Eq. (IV.1) with real ω. We show later that using a realistic (lossy) metal only modifies quantitative aspects of the flat band, while its fundamental physical origins remain unaltered.

For each polarization there is an infinite number of solutions to Eq. (IV.1), each characterized by a multipole number, l and $n \geq 0$ roots, the latter yielding a radial excitation number (i.e. *band index*). We first examine the resonant modes for asymptotic limits of Eq. (IV.1). For high-order multipoles satisfying $l \gg |k_m|S$ and $l \gg k_d S$ we expand j_l and h_l to obtain the resonance condition

$$\epsilon_m(\omega_l) + \epsilon_d = 0. \tag{IV.2}$$

for TM polarization. No similar resonance condition exists for TE polarization. We next look for an expression for L such that Eq. (IV.2) is also satisfied for the TM mode with the smallest multipole number. For $l = 1$ where expansions of j_l and h_l may be applied, Eq. (IV.1) reduces to

$$(2n - 1)\pi = 2k_d L, \tag{IV.3}$$

with $n \geq 1$.

The high order multipole modes of Eq. (IV.2) belong to the $n = 1$ radial excitation band, hence by setting $n = 1$ in Eq. (IV.3), we obtain the geometric condition

$$L = L^\star \equiv \frac{\lambda_{sp}}{4\sqrt{\epsilon_d}} \tag{IV.4}$$

where $\lambda_{sp} = 2\pi c/\omega_{sp}$ and ω_{sp} is given by $\epsilon_m(\omega_{sp}) + \epsilon_d = 0$. The position of the flat band given by Eq. (IV.2) and the geometric condition, Eq. (IV.4), do not depend on R and are identical to those for the planar [100] and cylindrical MDM geometries. See Appendix C for detailed derivations of the flat-dispersion conditions for planar, spherical, and cylindrical MDM systems.

Figure 25(a) shows the resonant frequencies of the system plotted as a function of the multipole number l. To approximate the optical response of silver, we have chosen $\epsilon_b = 5.1$ and $\hbar\omega_p = 9.1$eV[101]. The dielectric shell has $\epsilon_d = 3.53$, corresponding to the measured value of amorphous titania. For clarity, we have chosen a high dielectric constant to place ω_{sp} well away from the bulk plasma resonance at ω_p. Using Eq. (IV.4), we obtain $L^\star = 53.4$nm. We set $R = 500$nm. From the figure, it is clear that there is a band of TM modes whose frequencies are weakly dependent on the multipole number. This flat-dispersion band is near $\omega_{sp}/\omega_p = (\epsilon_b + \epsilon_d)^{-1/2} \approx 0.34$ as expected, and the width of the band is given by $\delta\omega/\omega_{sp} = 0.014$ where $\delta\omega$ is the difference of the largest and the smallest frequencies in the band. For comparison, Fig. 25(b) shows the dispersion relation of a dielectric sphere of radius $R + L$ embedded in a metallic host.

By analyzing the dispersion relation of MDM spheres with various core radii, we have found that when $R \geq 100$nm, $\delta\omega$ depends weakly on the core radius R. For example, $\delta\omega/\omega_{sp} = 0.018$ for $R = 100$nm and $\delta\omega/\omega_{sp} = 0.014$ for $R = 1000$nm. We have observed that the material dispersion of the metallic medium affects the

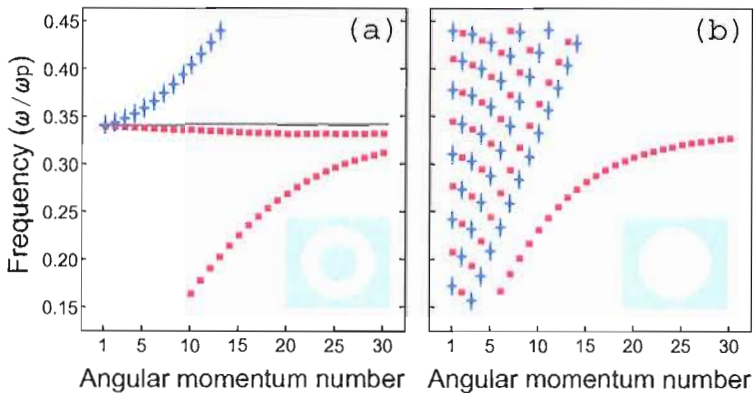

FIGURE 25. (a) Dispersion relations of an MDM sphere for TM (squares) and TE (crosses) modes. Near the plasmon frequency ω_{sp} (solid line), there is a flat band of TM modes weakly dependent on the multipole number. (b) Dispersion relation of the same structure without a metal core. The insets show schematic cross-sections of the systems.

flatness $\delta\omega/\omega_{sp}$ more significantly; a larger and positive $d\epsilon_m/d\omega|_{\omega_{sp}}$ leads to a flatter dispersion relation.

The weak dependence of the resonant frequency on l is reminiscent of the Coulomb potential system in quantum mechanics. In nonrelativistic quantum mechanics, if the potential is $V(r) = -\frac{e^2}{r}$, then the energy level is given by

$$E_n = -\frac{me^4}{2\hbar^2 n^2}.$$

It is independent of the angular momentum number l, because, in addition to the spherical symmetry, the system has an extra symmetry. The generator of the symmetry is given by the Laplace-Runge-Lenz vector[102],

$$\vec{K} = \frac{1}{2me^2}\left(\vec{L}\times\vec{p} - \vec{p}\times\vec{L}\right) + \frac{\vec{r}}{r},$$

which commutes with the Hamiltonian. By writing Maxwell's equations in an

operator form, i.e.

$$H\psi = \omega_{nl}\psi,$$

where

$$H = \begin{pmatrix} 0 & i\frac{c}{\epsilon(\vec{r})}\vec{\nabla}\times \\ -ic\vec{\nabla}\times & 0 \end{pmatrix}$$

and

$$\psi_{nlm} = \begin{pmatrix} \vec{E}_{nlm} \\ \vec{B}_{nlm} \end{pmatrix},$$

we have attempted to find an analogous operator K. Compared to the quantum system, there are two difficulties. First, the resonant frequencies of the SPRs of the flat band are only approximately equal. Therefore, if there is an analogous operator K, its commutator with H must be small, but not identically zero. Second, the weak dependence of ω_{nl} on l is only observed for one TM band. As a result, the symmetry defined by $\vec{K}$ cannot be the symmetry of the Hamiltonian. The flat-dispersion modes must have some special properties which renders $[H, K]\psi \approx 0$. Further research is necessary to see if the flat-dispersion band can be explained by a hidden symmetry the system.

Enhanced Absorption

Next, we analyze the absorption cross-section of the MDM sphere with a metal shell of finite thickness (finite MDM), and study the coupling between the incident plane wave and the flat-dispersion modes. Such spheres may be realized by chemical

synthesis of layered metallodielectric particles[8, 103]. We have developed an exact and numerically stable algorithm for calculating the absorption cross-section of multilayered spheres based on previous publications [104–108]. A detailed derivation of the algorithm is presented in Appendix C. We also account for absorption losses in the metal by modifying the Drude model to $\epsilon_m(\omega) = \epsilon_b - \omega_p^2(\omega^2 + i\Gamma\omega)^{-1}$, with Γ describing the electron relaxation rate. We set $\hbar\Gamma = 0.021\text{eV}$ [101] and $\epsilon_0 = 1$.

A sharp absorption peak near λ_{sp} is seen in Fig. 26(a). For a core of $R = 500\text{nm}$ this is maximized when $L = 62\text{nm}$ and $T = 77\text{nm}$, and it is positioned at $\lambda = 428\text{nm}$. The deviations of the peak from $\lambda_{sp} = 401\text{nm}$ and of the optimal value of L from $L^\star = 53.4\text{nm}$ are explained as follows: In addition to SPRs of the flat-dispersion band, SPRs of the outermost metal-host interface contribute to this peak. In fact, the two SPR branches are coupled through the finite metal shell. These plasmon hybridizations lead to slight modifications in peak position as well as in the optimal dielectric shell thickness.

The degree of coupling between the incident plane wave and the flat dispersion band is tuned by adjusting T, the thickness of the outer metal shell. As we show later, the value of L may be varied in the vicinity of $L^\star$ to spectrally tune the absorption maximum while maintaining a nearly flat dispersion band. For each such value of L there exists a T which optimizes the coupling. Nevertheless, if the metal shell is made too thin, strong plasmon hybridization will eventually distort the flat band.

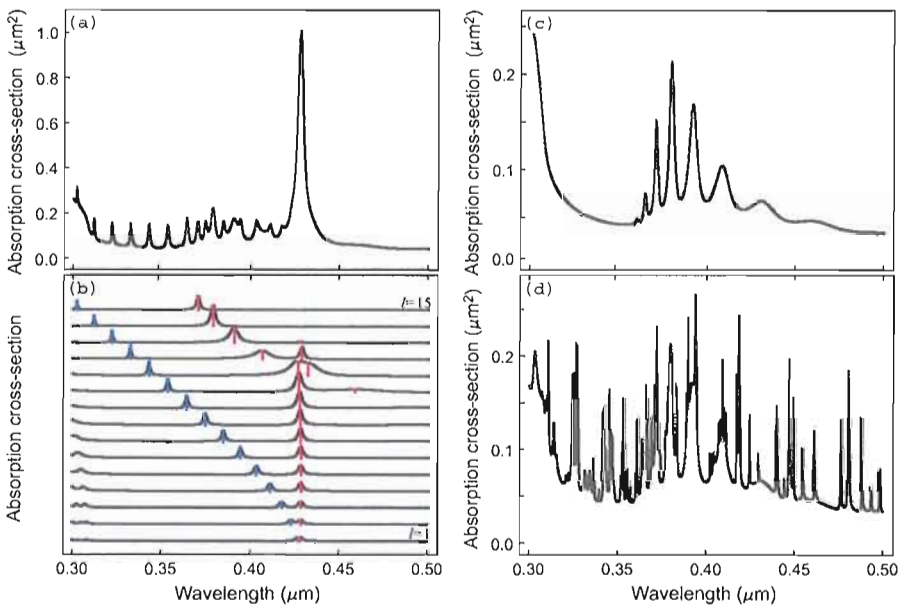

FIGURE 26. (a) Optimized absorption cross-section spectrum of MDM sphere with $R = 500$nm. (b) Mode decomposition of the spectrum from $l = 1$ (bottom) to $l = 15$ (top), showing contributions from TE modes (blue hatches), and TM modes (red hatches). (c) Absorption spectrum of a metal sphere of radius $R + L + T$. (d) Absorption spectrum of a sphere with a dielectric core of radius $R + L$ and metal shell of thickness T.

The mode decomposition of the spectrum, shown in Fig. 26(b), confirms that a large number of multipoles share nearly identical resonant frequencies and shows that the first 13 multipoles are excited concurrently by the incident plane wave. Higher order multipoles have negligible contribution to the absorption peak. Compared to the absorption spectrum of a metal sphere and of a core-shell of the same size, plotted in Fig. 26(c) and (d), the absorption cross-section of the MDM near $\lambda = 428$nm is enhanced by a factor of 10 and 4, respectively. The enhancement factor relative to the maximal absorption is seen to be ~ 4 for both cases. The enhanced absorption exists for all core radii $R \gtrsim 100$nm. The value of R affects the peak height and the

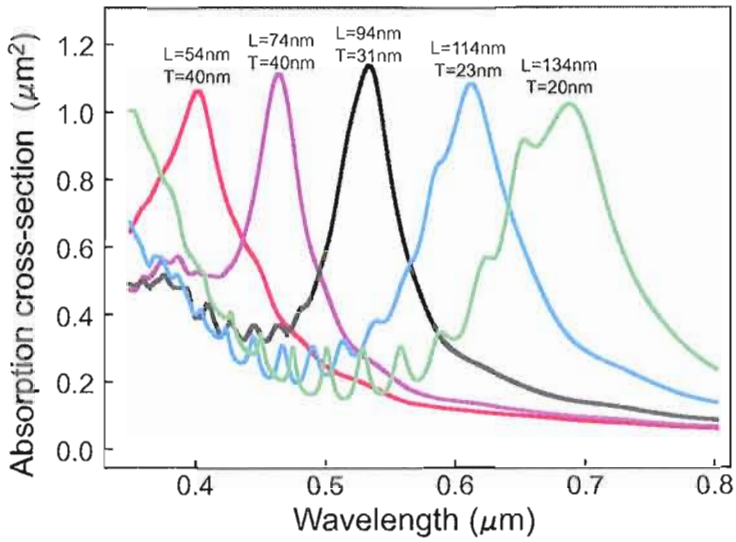

FIGURE 27. Absorption spectra of silver-titania MDM spheres with $R = 500$nm and various dielectric shell thickness L. The value of T is chosen to maximize the peak height.

number of simultaneously excited SPRs. Other spectral characteristics, such as the peak position, its FWHM, and the optimal values of L and T, are insensitive to the core size. For example, a change of a few hundred nanometers in the core radius alters the latter by less than several nanometers. For radii smaller than 100nm, the absorption broadens, splitting into multiple peaks. Below $R = 50$nm, the effect of the metal core on the absorption diminishes, the spectrum rapidly approaching that of a DMD nanoshell.

The enhanced absorption is also demonstrated numerically using the experimentally obtained dielectric function for silver[73]. For $R = 500$nm, the absorption cross-section peak is maximized for $L = 94$nm and $T = 31$nm, and it is at $\lambda = 533$nm with 64nm FWHM as shown in Fig. 27. The absorption enhancement factors relative to

a solid metallic sphere and to a core-shell sphere of a comparable size are 7 and 3, respectively. While the spectral position of the flat dispersion (i.e. ω_{sp}) depends only on the optical properties of the constituent media, the absorption peak position can be tuned by adjusting L. As discussed above, an arbitrary L does not produce a flat dispersion. However, the slope of the band, $\omega_l - \omega_{l-1}$, is generally small as long as $L \sim L^*$. Thus, it is possible to vary the value of L by tens of nanometers and shift the resonant frequencies, and still retain a significant overlap of the absorption cross-section peaks of various multipoles. Figure 27 shows the geometric tunability of the enhanced absorption over the visible range. Since the enhancement implies a large EM field concentration, these results suggest that the flat-dispersion MDM spheres may be used to enhance nonlinear optical phenomena, and more generally, they may lead to a new generation of mesoscale plasmonic systems in which numerous modes are excited to manipulate SPR-assisted light-matter interactions.

Plasmon Assisted Transparency

We have also found that the enhanced absorption of MDM microspheres is accompanied by a plasmon assisted transparency. The scattering cross-section for the same geometry and materials as above was also computed. As shown in Fig. 28, the transparency window is also tunable with the geometric parameters L and T. The low-scattering window follows the enhanced absorption as the values of L and T are varied. To establish the scale of the transparency peak, the figure also shows the well–known non–tunable transparency window near 320nm, attributed to the bulk

plasma resonance of the metal. Such intrinsic transparencies have been utilized to create high efficiency polarizing filters in planar MDM geometry[109].

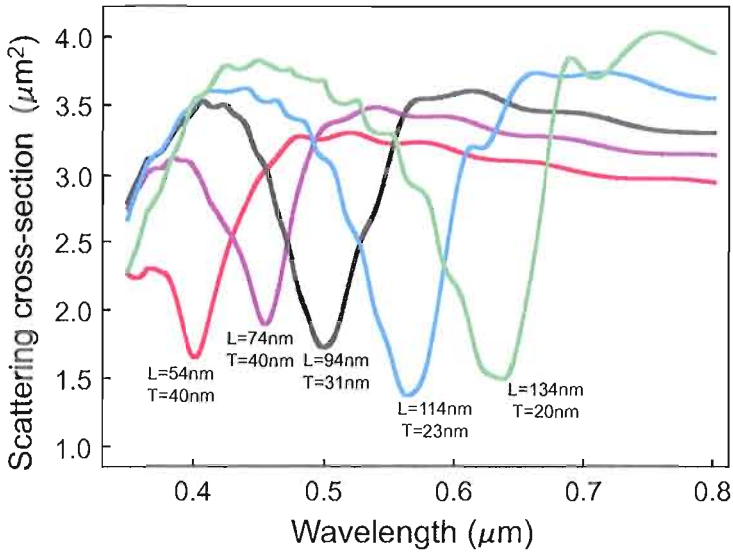

FIGURE 28. Scattering cross-section spectra of silver-titania MDM spheres with $R = 500$nm. The values of L and T are chosen to correspond to those found for the maximal absorption cross-section shown in Fig. 27.

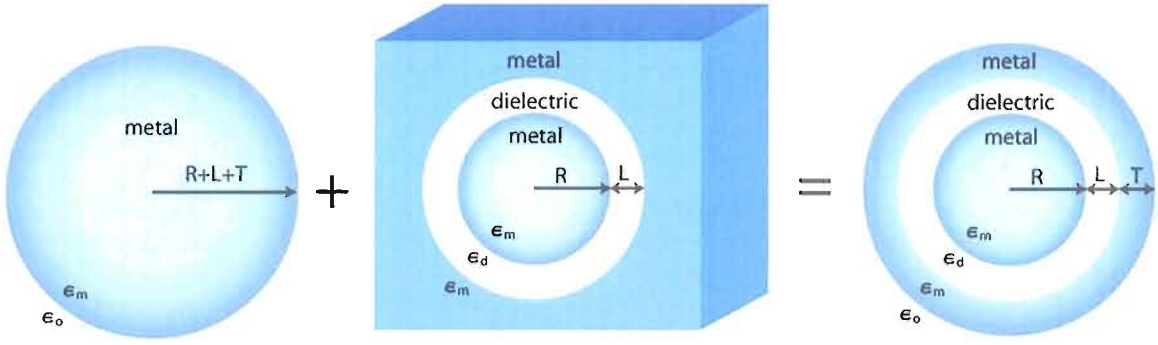

FIGURE 29. Surface plasmon hybridization for an MDM sphere. A finite MDM can be considered as a hybridized system of a solid metal sphere of radius $R+L+T$ and an infinite MDM with a core radius R and a dielectric shell thickness L.

In order to understand the mechanism behind the transparency, we consider a finite MDM sphere as a hybridized system of a solid metal sphere of radius $R+L+T$

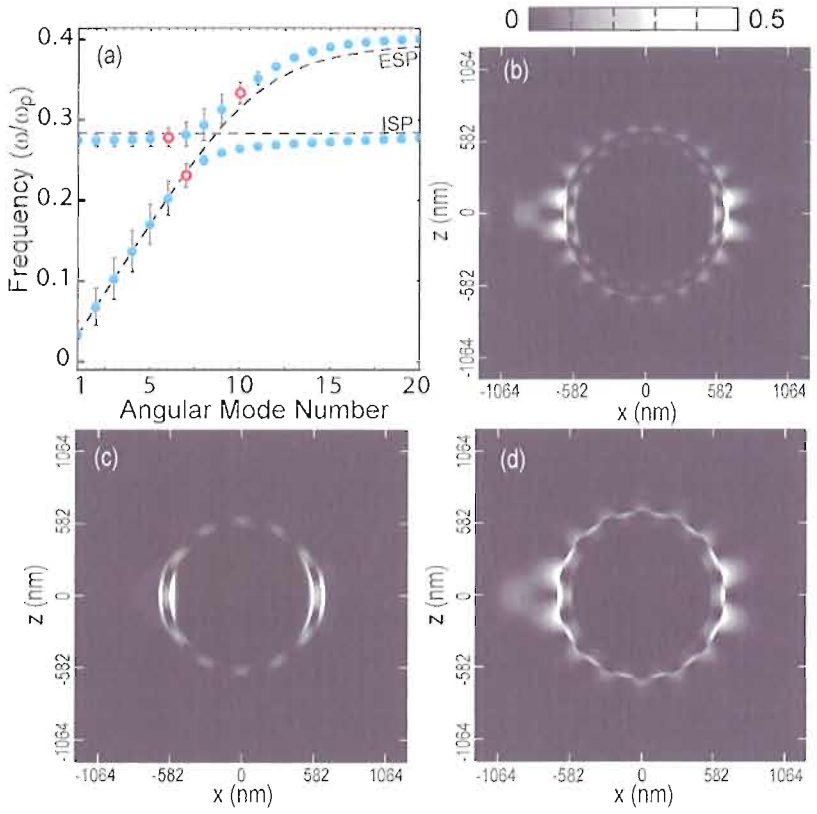

FIGURE 30. Surface plasmon resonances of a finite MDM sphere. (a) The dispersion diagram of an MDM sphere with $R = 500$nm, $L = 54$nm, and $T = 28$nm. The dielectric function of the metal follow the lossy silver-like Drude model presented in the previous subsection. The permittivity of the dielectric shell is $\epsilon_d = 5.76$. (b)–(c) Near-field energy density distribution of the SPRs indicated by the red circles in (a) at (b) $\omega/\omega_p = 0.336$, (c) $\omega/\omega_p = 0.294$, and (d) $\omega/\omega_p = 0.233$.

and an infinite MDM with core radius R and a dielectric shell thickness L as illustrated in Fig. 29. Unlike the nanoshells, the size scale of the MDM systems considered here are comparable or larger than the wavelength. Therefore, we must consider the hybridization of different SPR *bands*.

Figure 30(a) shows the eigenfrequencies of the three geometries in Fig. 29. The line labeled ESP is the SPR band of the solid metal sphere, while the dashed horizontal

line labeled ISP is the flat-dispersion band of the infinite MDM. In the finite MDM, these two bands become hybridized, resulting in an avoided crossing as shown by blue dots. The width of each resonance is given by a vertical bar in the figure. For clarity, the figure does not show the lowest ($n = 0$) SPR band or the TE bands. In Fig. 30(b)–(c), we plot the EM energy densities corresponding to three eigenmodes denoted by red circles in Fig. 30(a). The energy densities of the high- and low-frequency modes (Fig. 30(b) and (d)) are concentrated near the outer interface of the metal shell. They resemble the SPRs of a solid metal sphere, and are associated with the *external surface plasmon*(ESP) branch of the finite MDM. Since the energy density is concentrated near the outer interface, they are coupled to radiative modes. As a result, when excited, these modes make significant contribution to the scattering cross-section. On the other hand, the energy density of the intermediate frequency mode is primarily focused near the inner two metal-dielectric interfaces as shown in 30(c). The distribution is similar to the flat-dispersion mode of an infinite MDM, and it belongs to an *internal surface plasmon*(ISP) branch of the finite MDM. Since the energy density is primarily localized inside the MDM sphere, it does not couple strongly to radiative modes. Hence, an excitation of the ISP modes makes an insignificant contribution to the scattering cross-section. Near the avoided crossing, the ESP and ISP modes are strongly coupled. The coupling causes the resonant frequencies of the ESP and ISP to split, producing a window of ω where the highly radiative ESP modes are absent. As a result, the scattering cross-section is reduced

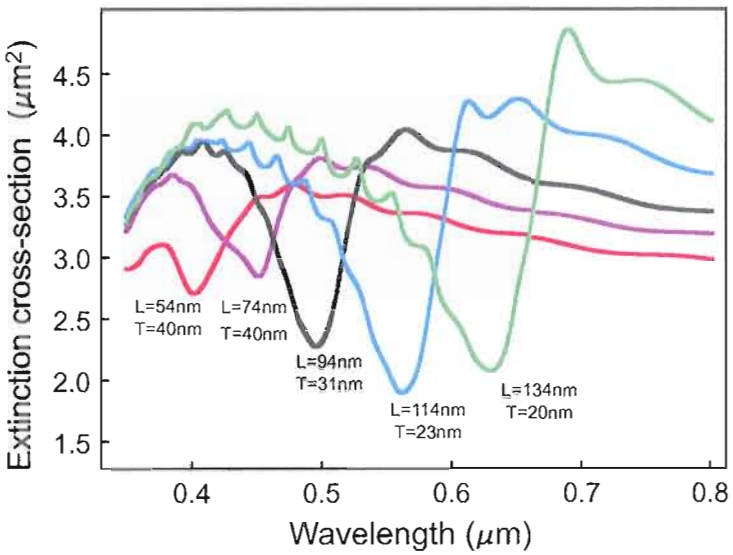

FIGURE 31. Extinction cross-section spectra of silver-titania MDM spheres with $R = 500$nm. The values of L and T are chosen to correspond to those found in Fig. 27 and Fig. 28.

considerably within the window as shown in Fig. 28. The transparency window is tunable with L and T, since the spectral position of the avoided crossing can be shifted by modifying the slope of the flat-dispersion band.

In many experiments, the quantity of interest is the extinction cross-section, which is equal to the sum of the absorption cross-section and the scattering cross-section. If the transmittance intensity I_T of light through a suspension of particles is measured, then it is related to the extinction cross-section σ_{ext} of the individual particle through the Beer's law:

$$I_T = \exp(-\sigma_{ext} n l) I_0,$$

where n is the number density of the particles, l is the path length of the suspension, and I_0 is the incident intensity. For the MDM spheres considered, the absorption

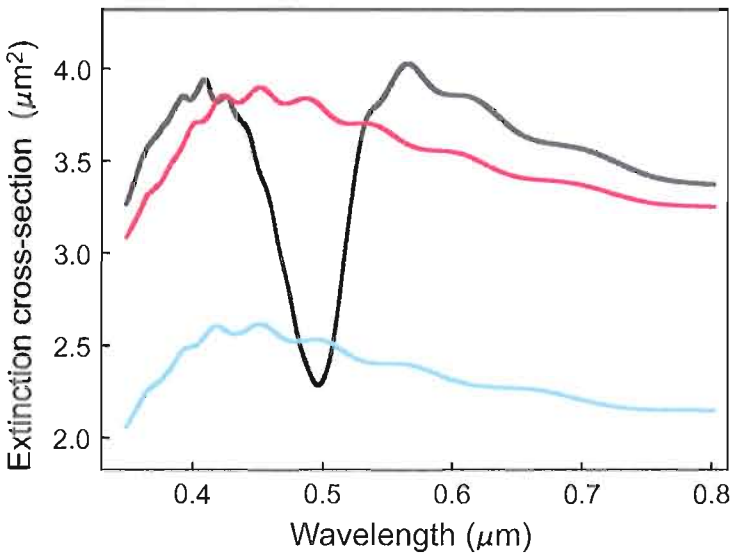

FIGURE 32. Comparison of the extinction spectra of a silver-titania MDM with $R = 500$nm, $L = 94$nm, and $T = 31$nm(black); a solid metal spheres of radius $R + L + T = 625$nm(red); and radius $R = 500$nm(blue).

cross-section is considerably smaller than the scattering cross-section. Moreover, the enhanced absorption peak is generally slightly shifted in frequency relative to the transparency window. Therefore, the extinction cross-section spectrum also exhibits a tunable transparency window as shown in Fig. 31.

In order to evaluate the degree of the transparency, we compare the extinction cross-section of an MDM with that of solid metal spheres of various radii in Fig. 32. Within the transparency window, the extinction cross-section of the MDM is considerably smaller than that of a solid metal sphere of the same geometric cross-section. Surprisingly, it is even smaller than the extinction cross-section of the metal core by itself. Therefore, by adding thin dielectric and metal shells, we have made

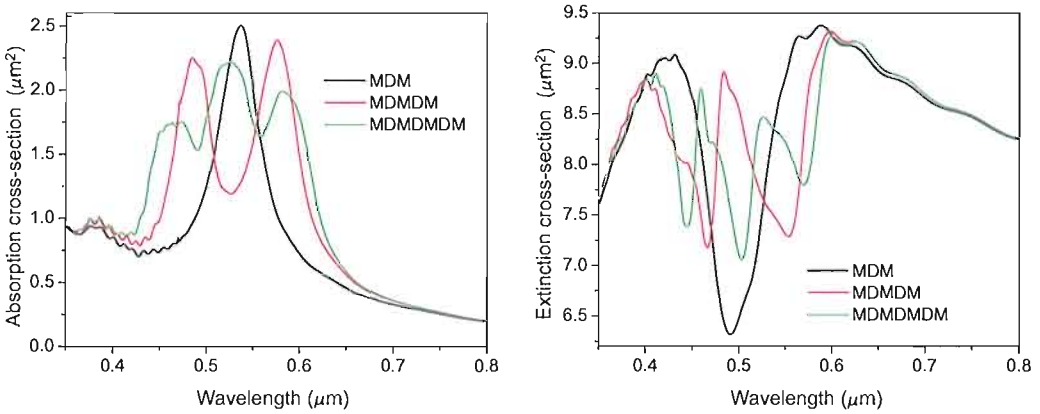

FIGURE 33. The absorption and extinction cross-sections of multi-MDM spheres: silver-titania MDM (black), MDMDM (red), and MDMDMDM (green). For each sphere, the total radius is 1000nm, and the dielectric and metal shell thicknesses are $L = 94$nm and $T = 31$nm, respectively.

the metal core less visible to incident light. Such metal-dielectric coatings may be used for an optical cloaking of macroscopic objects.

Beyond MDM

Thus far, we have shown that a properly designed MDM sphere exhibits an enhanced absorption peak and a plasmon assisted transparency window. It is possible to create multiple enhanced absorption peaks and transparency windows by introducing additional layers of alternating metal and dielectric shells as shown in Fig. 33. By adding another sequence of dielectric and metal shells to MDM, we create a MDMDM sphere, which exhibits two well-resolved absorption peaks as well as two transparency windows. Introducing another sequence of shells to MDMDM produces yet another absorption peak and transparency window. These multiple

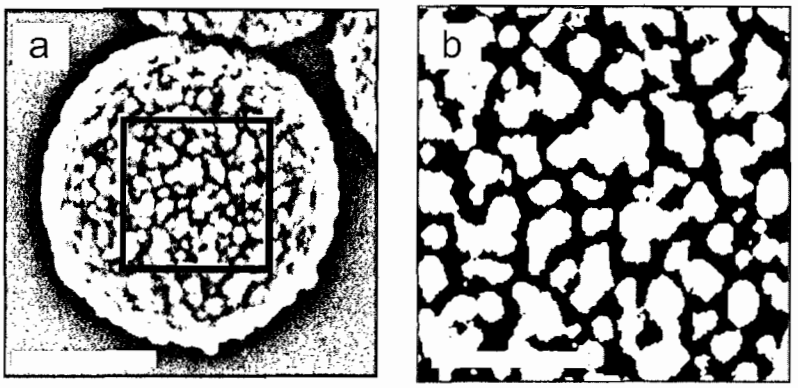

FIGURE 34. (a) SEM image of a percolative nanoshell with diameter 1μnm with 20nm thick silver shell. Scale bar corresponds to 500nm. (b) Digitally processed binary image of the square region in (a). Scale bar corresponds to 200nm. Similar images from ~ 100 spheres are used to obtain the average filling fraction of $\bar{p} = 0.55$.

enhanced absorptions and plasmon assisted transparencies are results of multiple flat-dispersion bands and avoided crossings in the dispersion relations. Further research is necessary to systematically investigate the optical properties of spherical systems with an arbitrary number of alternating layers of metal and dielectric shells.

Semicontinuous Nanoshells

We now turn our attention to light scattering from semicontinuous nanoshells. As discussed earlier in this chapter, nanoshells with smooth metal coatings support geometrically tunable multipole SPRs. In this section, we show that semicontinuous metal nanoshells also support geometrically tunable SPRs. Semicontinuous silver films of various filling fractions are deposited on silica spheres (300–1000nm diameter) using a modified Tollen's reaction[110]. Transmission electron micrographs (TEM)

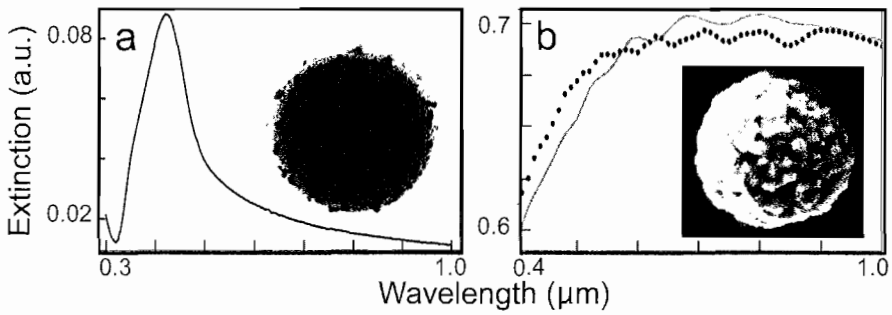

FIGURE 35. (a) The measured extinction spectrum of 1μnm diameter spheres sparsely coated with silver nanocrystals. The inset shows the TEM image of a typical sphere. (b) Measured (dots) and calculated (line) extinction spectra of 1μnm diameter spheres with 70nm thick silver shells. The MG theory is used to obtain the calculated extinction. The SEM image of a typical sphere is shown in the inset.

of the coated samples are used to measure the average shell thickness. Moreover, scanning electron micrographs (SEM) are taken to determine the filling fraction p. Figure 34 shows a SEM image of a typical sample.

The optical response of the semicontinuous nanoshells are characterized by measuring their extinction spectrum of dilute aqueous suspensions of the particles with a UV-Vis spectrometer. For sparsely coated spheres, the extinction has a sharp resonance peak near $\lambda = 420$nm as shown in Fig. 35(a). This is characteristic of the SPRs of the individual, nonaggregate silver nanocrystals on the silver sphere. Note that the peak position is slightly shifted toward longer wavelength compared to Fig. 21 because the nanocrystals are in water. Due to the sparsity of the coating, these nanoparticle SPRs are not coupled to each other. Furthermore, since they are not coupled to the weak Mie resonance of the silica sphere, the extinction peak is not geometrically tunable with the sphere diameter.

On the other hand, silica spheres with thick silver coatings as in Fig. 35(b) exhibit SPRs that depend on the radius and the thickness of the particles. The extinction spectra exhibit resonant peaks, which we attribute to the multipolar SPRs of the nanoshells. Unlike the extinction in Fig. 22, several peaks are visible since the size scale of the nanoshells is comparable to the wavelength, and thus, several SPRs lie within the spectral range. SEM images indicate that the silver shells have high filling fractions ($0.8 \lesssim p \lesssim 0.9$) with small interparticle voids. As a result, the Maxwell-Garnett (MG) effective medium theory, described in Chapter III, may be used to model the dielectric response of the porous shells. Recall that the MG theory provides an effective permittivity of a heterogeneous structure made of small spherical inclusions within a host medium. By considering the thick coating as a metal host with small dielectric inclusions, we derive the dielectric function ϵ_{MG}, which is used to calculate the extinction spectrum of the particle using a modified Mie theory. While there are some discrepancies in the spectral positions of some resonant peaks, the calculated extinction spectrum reproduces the measured extinction well as shown in Fig. 35(b).

Semicontinuous nanoshells with intermediate surface coverage, such as the one shown in Fig. 34, also exhibit geometrically tunable resonances as shown in Fig. 36. Near-field studies of vacuum deposited, semicontinuous metal films on flat substrates have shown that the samples whose filling fraction is near the percolation threshold support cluster-localized surface plasmon "hot spots" that are randomly distributed

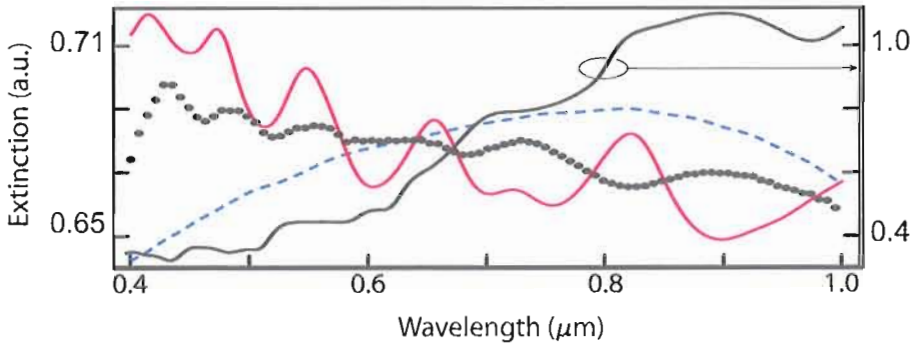

FIGURE 36. The measured extinction spectrum of the thin nanoshells (dots) shown in Fig. 34. For comparison, calculated extinction obtained using the modified ST (red), the BR theory (blue), and the tabulated bulk silver dielectric function (black).

over their surfaces[111, 112]. SEM images indicate that the surface morphology of our chemically deposited, semicontinuous films are similar to that of the vacuum deposited samples. Therefore, we expect the cluster-localized surface plasmons to exist on the nanoshells. The observed geometrically tunable peaks in the extinction indicate that these localized modes are coupled to the cavity Mie resonances of the silica sphere. Thus, varying the sphere size modifies the cavity modes, which in turn, affects the number of peaks and their positions.

In the past, the dielectric response of vacuum deposited, semicontinuous films near the percolation threshold has been modeled with a scaling theory (ST)[84, 113, 114]. We develop a model for describing the dielectric response of nanoshells by modifying ST. In the following paragraphs, we summarize the basic concept of ST and explain our modifications. For the details of ST, see Ref. [84].

A number of experiments have indicated that the electric conductivity of disordered conductor-insulator composite films near the percolation threshold has a

power-law dependence on $|p-p_c|$ where p is the filling fraction and p_c is the percolation threshold[115–117]. We assume that the average conductivity satisfies

$$\langle\sigma\rangle = \chi F\left(\delta p\ \eta^{-1}, \sigma_i\chi^{-1}\eta^{-s}, \sigma_m\chi^{-1}\eta^{\mu}\right) \tag{IV.5}$$

for a square piece of the sample with a linear dimension L_ξ[118]. Here, $\delta p = (p-p_c)/p_c$, σ_i and σ_m are the conductance of the insulating and conducting inclusion, respectively. The critical parameter η measures how close the system is to the percolation threshold, while the other critical parameter χ is associated with the scale transformation invariance of Kirkoff's law (i.e. multiplying σ_i and σ_m by a common factor changes $\langle\sigma\rangle$ by the same factor). The length scale L_ξ is the maximum length scale over which the system obeys the scaling law. Therefore, it is defined as

$$L_\xi = \min\left\{L, L_\omega, \xi\right\},$$

where L is the system size, L_ω is the coherence length, and ξ is the percolation correlation length. The coherence length is given by

$$L_\omega = B\xi_0(\lambda/\xi_0)^{-1/(2+\theta)} \sim \omega^{-1/(2+\theta)},$$

where λ is the wavelength, $\theta = 0.79$, and B is a coefficient of order 1. It determines the average distance electrons travels through the random network of conductors, and is often identified as the localization length[114]. The percolation correlation length $\xi = \xi_0|p-p_c|^{-\nu}$ describes the "connectivity" of the random network of the insulators or the conductors, with ξ_0 as the typical nanocrystal size. For 2D systems, the critical exponents are $\mu = s = 1.3$ and $\nu = 4/3$[113].

Let $\chi = \sigma_m |\delta p|^\mu$ and $\eta = |\delta p|$. Then, Eq. (IV.5) becomes

$$\langle \sigma \rangle = \sigma_m |\delta p|^\mu F\left(\mathrm{sgn}(p - p_c), \frac{\sigma_i}{\sigma_m} |\delta p|^{-s-\mu}, 1\right).$$

Near the percolation threshold, the function F can be expanded as

$$\begin{aligned} F(1, z, 1) &\approx A_1 + A_2 z \\ F(-1, z, 1) &\approx A_3 z + A_4 z^2 \end{aligned}$$

with A_i as the coefficients of the order 1. The constant term is absent in the second equation since for $p < p_c$ (i.e. $\mathrm{sgn}(p - p_c) = -1$) there is no conducting path across the sample. Following Ref. [84], we describe the ac conductivities of the insulating and conducting inclusions by

$$\begin{aligned} \sigma_i &= -i\omega C_0 \\ \sigma_m &= \sigma_{dc}/(1 - i\omega\tau) \end{aligned} \qquad \text{(IV.6)}$$

where C_0 is the capacitance between two neighboring metal grains, σ_{dc} is the dc conductivity of the metal, and $\tau = \tau_0 + b_\tau \omega^2$ is the frequency dependent relaxation time. The average local permittivity of a $L_\xi \times L_\xi$ patch is determined by the usual relation

$$\langle \epsilon \rangle = \epsilon_0 + i4\pi \langle \sigma \rangle / \omega.$$

Since the local filling fraction p of a $L_\xi \times L_\xi$ patch can deviate from the average filling fraction $\bar{p}$, each patch can be either conducting or insulating with an average dielectric function $\langle \epsilon(\omega, L_\xi) \rangle_c$ or $\langle \epsilon(\omega, L_\xi) \rangle_i$, respectively.

As is mentioned above, the cluster-localized SPRs are coupled to the cavity Mie resonances of the silica sphere. Therefore, the localized SPRs can be driven coherently by the incident light. To account for this coupling, we modify ST by defining the shell-averaged dielectric permittivity using the Newton formula[119]:

$$\epsilon_{shell}(\omega) = \bar{p}\langle\epsilon(\omega, L_\xi)\rangle_c + (1-\bar{p})\langle\epsilon(\omega, L_\xi)\rangle_i. \tag{IV.7}$$

Figure 36 shows the calculated extinction of the nanoshell using ST, the Bruggeman (BR) theory, and the tabulated bulk silver dielectric function[73]. The parameters for ST follow Ref. [84] except the following modifications: $\sigma_{dc} = 2.574 \times 10^{17}\text{sec}^{-1}$, $b_\tau = 3 \times 10^{-16}$sec, $L = 1\mu$m, and $C_0 = 0.884$. Due to the large number of ST parameters, we have found the multivariate fitting to be impractical. Both ST and the BR theory curves are obtained by performing Gaussian averaging over the measured filling fraction distribution and the sphere size distribution with the following parameters: $\bar{p} = 0.55$, $\sigma_p = 0.08$, $\bar{r} = 500$nm, $\sigma_r = 10$nm, $\bar{T} = 24$nm, $\sigma_T = 3.1$nm where T is the shell thickness. As the figure illustrates, the number of resonances, their positions as well as their contrast are poorly described by the BR theory and the tabulated bulk silver dielectric function. On the other hand, ST reproduces the spectral positions of some of the resonances as well as the overall trend of the measured extinction, indicating that the coherently driven cluster-localized SPRs of the semicontinuous nanoshells can be described reasonably well by ST. Like EMTs, ST ignores the effect of surface roughness. In the previous chapter, we have discussed the importance of surface roughness in describing the optical properties

of semicontinuous films. Given this fact, it is not surprising that there are some discrepancies between ST and the observed extinction.

Conclusions

In summary, we have presented a study of SPRs on layered metal-dielectric particles. In the first part of the chapter, we have investigated the optical properties of MDM spheres. Using the concept of dispersion engineering, we have shown that the spheres support a band of SPRs whose resonant frequencies are nearly identical. A large number of these SPRs can be excited simultaneously by an incident light, enhancing the absorption cross-section of the spheres. Moreover, the dispersion relations exhibit an avoided crossing, which creates a plasmon assisted transparency window in the extinction cross-section. In the second part of the chapter, we have presented a study of light scattering from semicontinuous nanoshells. We have shown that when the filling fraction is close to the percolation threshold, ST can be used to model the coherently driven cluster-localized SPRs. Further research is necessary to refine ST and our understanding of the coherently driven localized SPRs.

CHAPTER V

CONCLUSIONS

In recent years, the promises for new technological applications have led to a surge of interest in plasmonics among scientists. While a number of novel plasmonic devices have been developed, our present understanding of the fundamental nature of SPPs and how they affect the optical properties of metal-dielectric systems is still far from complete. In this dissertation, we have investigated the effect of curvature, roughness, and number of metal-dielectric layers on SPPs and the optical properties of metal-dielectric systems. In Chapter II, we explored how surface curvature affects the propagation of SPPs on metal-dielectric interfaces. We developed a qualitative and intuitive model for describing the origin of the curvature-induced radiation. Using the model, we derived the parameter G whose magnitude determines the degree of the radiation. This quantity sets a limit on how small the radius of curvature can be without significantly affecting SPP propagation length, and may also set a limit on the size scale of plasmonic circuit devices.

Moreover, we have quantified the propagation efficiency both analytically and numerically. In the short wavelength limit, we derived the energy transmission and reflection coefficients using a method analogous to a quantum mechanical 1D finite square well. By analyzing the upper bound on the transmittance, we also

showed that the nonmonotonic behavior of the transmittance is a result of three competing mechanisms: absorption, radiation, and diffraction. Furthermore, our FDTD simulation results indicate that the upper bound is a good estimate for the transmittance for all bend radii larger than the wavelength. When the SPPs propagate around a dielectric void, it is shown that SPP propagation is less radiative, and hence, more efficient. This prediction was confirmed with simulations. Finally, we introduced a bend-resonator geometry for enhancing the transmission efficiency. In general, our results indicate that an efficient propagation around a curved surface is possible only when SPPs propagate around a metal surface with a small and negative radius of curvature. In other systems we have studied, most of the incident energy is lost either as radiation loss or absorption. One way to compensate for the losses could be by incorporating a gain medium to amplify SPPs. Further research is necessary to test if presently available gain media would provide large enough gain to overcome the losses.

In Chapter III, we investigated how the surface morphology influences the transmittance and the reflectance of light from disordered metal-dielectric films. Using a modified Tollen's method, semicontinuous silver films of various surface coverage are deposited on glass substrates. The films exhibit a large broadband asymmetry in reflectance, and it has been shown that the asymmetry cannot be explained adequately by any EMT, which ignores the effect of surface roughness. To investigate how the surface morphology influences the reflection asymmetry, we

annealed the samples at various temperatures to induce changes in the morphology and measured corresponding changes in the reflectance. We discovered that the large asymmetry is due to the different surface roughness light encounters when incident from different sides of the film. It was shown that the air-silver interface is at the smooth-rough transition according to the Rayleigh criterion, and produces significant diffusive scattering and small specular reflection R_1. On the other hand, R_2 is largely due to the coherent reflection of light from the smooth bottom surface of the silver grains, and therefore, depends primarily on the surface coverage. We have performed angle-resolved measurements to compare the diffusive scattering from both sides of the film, and shown that it is significantly greater from the air-silver side than from the substrate-silver side as predicted. Moreover, the measurements have shown that the diffusive scattering obeys Lambert's Cosine Law, indicating that a multiple scattering is preferred over a single scattering from the surface. Our investigation so far has not revealed if SPPs play any important role in the optical properties of disordered metal-dielectric films. To better understand the optics of disordered films, it is essential to investigate how surface morphology affects the nature of SPPs on the disordered system, and how those SPPs in turn affect the far-field optical measurements. Further research is necessary to uncover how surface roughness influences the optical response of semicontinuous metal films.

In Chapter IV, we explored light scattering from layered metal-dielectric systems. Using the concept of dispersion engineering, we have shown that a properly designed

MDM microsphere supports a band of SPRs whose resonant frequencies are nearly identical. Unlike SPRs of nanoscale metal-dielectric systems, these SPRs can be excited simultaneously by a monochromatic incident light, producing a geometrically tunable enhanced absorption. Moreover, using a modified Mie theory, we have shown that the extinction cross-section of the system exhibits a tunable plasmon assisted transparency window. Surprisingly, our study shows that coating a metal sphere with one sequence of dielectric and metal shells reduces its extinction cross-section, rendering the particle less visible. This suggests that alternating metal-dielectric coatings may be used for an optical cloaking of macroscopic objects. Additionally, we have studied light scattering semicontinuous silver nanoshells, and developed a modified scaling theory in an attempt to model their optical response. Our study suggests that particles support coherently driven cluster-localized plasmons. Much work remains in the investigation of optical properties of layered metal-dielectric particles. It would be interesting to fabricate MDM spheres in a laboratory and to test if the spheres exhibit enhanced absorption and plasmon assisted transparency in a laboratory setting. It would also be interesting to investigate how well a simultaneous excitation of a large number of SPRs enhances the nonlinear optical response of MDM systems. Further research is also necessary to systematically explore the optical properties of spherical systems with an arbitrary number of alternating layers of metal and dielectric shells.

The research presented in this dissertation has been fundamental in its approach to plasmonics. Rather than attempting to develop novel plasmonics devices, our attempt has been to improve our present understanding of SPPs and how they are affected by surface curvature, surface roughness, and the number of metal-dielectric interfaces. Further research will improve scientists' insight into the fundamental nature of the SPPs, and into the true potential of plasmonics.

APPENDIX A

FINITE-DIFFERENCE TIME-DOMAIN METHOD FOR SIMULATING SURFACE PLASMON POLARITONS

The finite-difference time-domain method (FDTD) is a versatile numerical technique for solving Maxwell's equations in time domain, which was originally introduced by Kane Yee in 1966[120]. FDTD offers a number of advantages over other numerical methods such as the finite element method. In general, FDTD requires less memory and is more robust compared to other techniques. Moreover, unlike frequency-domain methods, FDTD can treat the propagation of pulses and the nonlinear response of systems naturally. Furthermore, it can simulate the electromagnetic response of inhomogeneous, lossy, and anisotropic media with relative ease. For these reasons, FDTD has become one of the most widely used numerical methods for solving electromagnetic problems. It has been used to simulate a wide variety of electromagnetic systems, including the propagation of low-frequency electromagnetic waves around the Earth's ionosphere, interference of electromagnetic radiation from a cell phone with the human head, detection of breast cancer using microwave radar, and photonic crystal microcavity laser (See [121] and references therein).

There are three major difficulties associated with using FDTD to simulate the propagation of SPPs. First, when discretizing the computational domain, the lattice spacing must be much smaller than the wavelength. Due to the evanescent nature of SPPs, their electromagnetic field decays rapidly into the metal and dielectric. For example, in the visible range, the typical decay length into the metal is $\sim$ 20nm. Thus, in order to simulate this evanescent nature of SPPs on a discretized computational domain, the lattice spacing must be much smaller than 20nm. For comparison, a typical lattice spacing for FDTD simulations not involving an evanescent field is $\lambda/20$, or $\sim$ 30nm in the visible range. Using a small, uniform grid size in the computational domain is straightforward. However, it also requires a large memory and long computational time.

It is possible to increase the efficiency of the FDTD simulation by using nonuniform orthogonal grids [121]. Since SPPs only decay rapidly near metal-dielectric interfaces and in the direction perpendicular to the surface, it is only necessary to employ small lattice spacing near the surface in the perpendicular direction. In the parallel direction or away from the interface, grid size of $\lambda/20$ is generally sufficient. In our simulation, using a nonuniform, orthogonal grid where lattice spacing was varied between $\lambda/300$ and $\lambda/20$ reduced the memory requirement and computational time by one to two orders of magnitude.

The second difficulty for simulating the propagation of SPPs is incorporating the proper optical response of metal. Since FDTD simulations are carried out in the

time domain, it is essential that the dispersions of all materials are modeled using dielectric functions that preserve the causality, such as the Debye model or the Drude model. For this reason, it is not possible to let the electric permittivity of the metal be a constant with negative real part. Such simplification of the dielectric function renders FDTD unstable. To include the proper frequency response of the metal in the time domain, the electric displacement field must be obtained by computing the convolution of the electric field and the material response function (i.e. time-domain susceptibility). In FDTD, this is accomplished using a numerical technique for, such as the piecewise linear recursive convolution (PLRC)[122], Z-transform[123], and auxiliary differential equation[124], for calculating the convolution.

The third difficulty is the absorbing boundary conditions (ABCs) for truncating the computational domain. In our simulations, the transmitted and the reflected SPPs as well as any radiation must "leave" the computational domain without producing any spurious numerical reflection at the domain boundaries. This is accomplished by using ABCs. While they are effective, commonly used ABCs, such as Mur's ABC[125] and Berenger's perfectly-matched layer (PML)[126], were developed for truncating non-dispersive media. Therefore, they are not suited for absorbing outgoing SPPs, which propagate on metal surfaces. Other ABCs must be used to terminate dispersive media.

This Appendix presents one way to overcome these difficulties by employing the FDTD algorithm with PML for dispersive media developed by Fan and Liu[74] and

using a nonuniform orthogonal grid. We assume that the magnetic field of SPPs to be parallel to $\hat{z}$: $\vec{H} = H_z\hat{z}$. As we have done in Chapter 2, we assume that the system is uniform in the z-direction. As a result, there are only three nontrivial field components—H_z, E_x, and E_y—and they depend only on x and y coordinates, rendering the FDTD 2-dimensional. (It is straightforward to extend the following algorithm to 3D systems with all six field components present.)

We begin by modifying Maxwell's equations in the frequency domain. The curl equations in Gaussian units are

$$\vec{\nabla} \times \vec{E} = i\frac{\omega}{c}\vec{B}$$
$$\vec{\nabla} \times \vec{H} = -i\frac{\omega}{c}\vec{D} + \frac{4\pi\sigma}{c}\vec{E}$$

where σ is the electric conductivity. To formulate the FDTD algorithm with PML for dispersive media, the differential operator $\vec{\nabla}$ is replaced with $\vec{\nabla}_e$, where[127]

$$\vec{\nabla}_e = \hat{x}\frac{1}{e_x}\partial_x + \hat{y}\frac{1}{e_y}\partial_y + \hat{z}\frac{1}{e_z}\partial_z, \quad \text{and} \quad e_i = a_i + i\frac{\Omega_i}{\omega}.$$

In order to understand the significance of a_i and Ω_i, consider a plane wave propagating in the x-direction e^{ikx}. Replacing $\vec{\nabla}$ with $\vec{\nabla}_e$ in Maxwell's equations transforms x to $x' = x(a_x + i\Omega_x/\omega)$ and the planewave wave e^{ikx} to

$$\exp(ikx') = \exp(ia_xkx - \Omega_xkx).$$

This expression indicates that Ω_i and a_i represent an attenuation and a scaling factor, respectively. In the physical region where we study the propagation of SPPs, we let $e_i = 1$ (i.e. $\Omega_i = 0$ and $a_i = 1$) so that we recover the unmodified Maxwell's equations.

In the PML region near the computational domain boundaries, where we want the outward propagating waves to be absorbed without spurious numerical reflection, we let $\Omega_i \neq 0$.

Next, we split the vector fields ($\vec{E}$, $\vec{D}$, $\vec{B}$, and $\vec{H}$):

$$\vec{E} = \sum_{\eta=x,y,z} \sum_{\substack{\zeta=x,y,z \\ \zeta\neq\eta}} E_{\eta\zeta}\hat{\eta}$$

and similarly for other vector fields. For example, the z-component of the magnetic field becomes $B_z = B_{zx} + B_{zy}$. Roughly speaking, we can consider B_{zx} and B_{zy} as the z-component of the magnetic field associated with an electromagnetic wave propagating in the x and y direction, respectively. The field splitting allows us to selectively absorb the electromagnetic field associated with waves propagating in a specific direction while minimizing spurious numerical reflections caused by the impedance mismatch at absorbing boundaries.

With these modifications, Maxwell's curl equations become

$$\begin{aligned}
\frac{\partial E_y}{\partial x} &= i\omega\frac{a_x}{c}B_{zx} - \frac{\Omega_x}{c}B_{zx} \\
-\frac{\partial E_x}{\partial y} &= i\omega\frac{a_y}{c}B_{zy} - \frac{\Omega_y}{c}B_{zy} \\
-\frac{\partial B_z}{\partial x} &= -i\omega\frac{a_x}{c}D_y + \frac{\Omega_x}{c}D_y + \frac{4\pi\sigma}{c}a_x E_y + i\frac{4\pi\sigma}{c}\frac{\Omega_x}{\omega}E_y \\
\frac{\partial B_z}{\partial y} &= -i\omega\frac{a_y}{c}D_x + \frac{\Omega_y}{c}D_x + \frac{4\pi\sigma}{c}a_y E_x + i\frac{4\pi\sigma}{c}\frac{\Omega_y}{\omega}E_x.
\end{aligned}$$

We assume that the system is nonmagnetic (i.e. $\mu = 1$), so that $\vec{B} = \vec{H}$. Moreover, we have used our original assumptions that the system of interest is uniform along the z axis and that the magnetic field points in the z direction. Under these assumptions,

$E_x = E_{xy}$, $E_y = E_{yx}$, $D_x = D_{xy}$, $D_y = D_{yx}$, and $B_z = B_{zx} + B_{zy}$. Converting these equations into the time domain by the Fourier transform yields

$$\frac{\partial E_y}{\partial x} = -\frac{a_x}{c}\frac{\partial B_{zx}}{\partial t} - \frac{\Omega_x}{c}B_{zx} \tag{A.1}$$

$$-\frac{\partial E_x}{\partial y} = -\frac{a_y}{c}\frac{\partial B_{zy}}{\partial t} - \frac{\Omega_y}{c}B_{zy} \tag{A.2}$$

$$-\frac{\partial B_z}{\partial x} = \frac{a_x}{c}\frac{\partial D_y}{\partial t} + \frac{\Omega_x}{c}D_y + \frac{4\pi\sigma}{c}a_x E_y + \frac{4\pi\sigma}{c}\Omega_x \int_{-\infty}^{t} E_y(t')dt' \tag{A.3}$$

$$\frac{\partial B_z}{\partial y} = \frac{a_y}{c}\frac{\partial D_x}{\partial t} + \frac{\Omega_y}{c}D_x + \frac{4\pi\sigma}{c}a_y E_x + \frac{4\pi\sigma}{c}\Omega_y \int_{-\infty}^{t} E_x(t')dt'. \tag{A.4}$$

The electric displacement $\vec{D}$ in the time domain is given by

$$\vec{D}(t) = \epsilon_\infty \vec{E}(t) + \int_{-\infty}^{t} \vec{E}(t')\chi(t-t')dt' \tag{A.5}$$

where ϵ_∞ is the electric permittivity at $\omega \to \infty$, and $\chi(t)$ is the time-domain electric susceptibility. The optical response of a medium determines ϵ_∞, χ, as well as σ. For a dielectric medium that is nondispersive or weakly dispersive, we let $\chi = 0$, $\sigma = 0$, and $\epsilon_\infty = \epsilon$ where ϵ is the dielectric constant. For a dispersive medium that follows the Debye model of the form Eq. (II.16), the time-domain susceptibility is

$$\chi(t) = \frac{\epsilon_s - \epsilon_\infty}{\tau}\, e^{-t/\tau}\theta(t),$$

where θ is the Heaviside step function.

We now proceed to discretize Eq. (A.1) through Eq. (A.5). We assume that the magnetic field is evaluated at $t = (n + 1/2)\Delta t$, while the rest of the vector fields are evaluated at $t = n\Delta t$ where n is an integer. Then, the time derivative of field

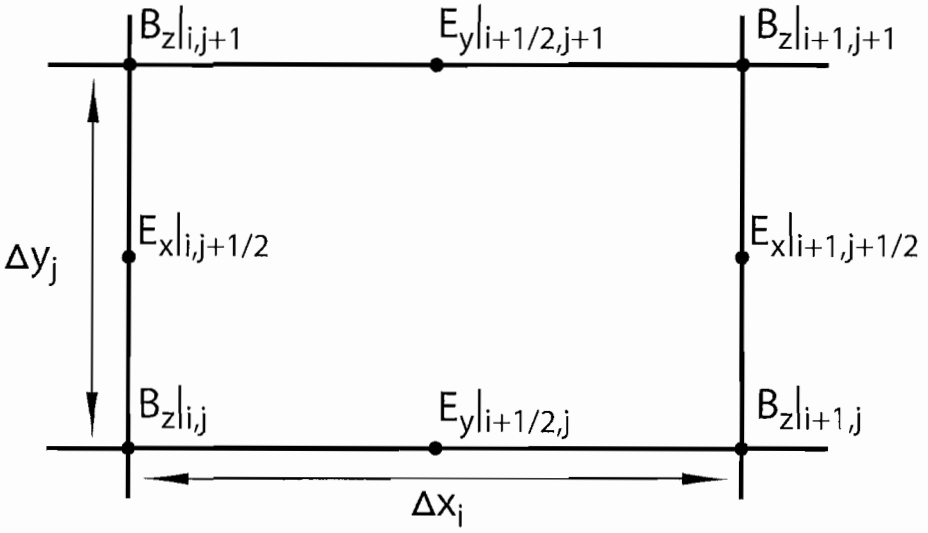

FIGURE 37. A unit cell of the 2-dimensional Yee lattice for transverse magnetic modes.

component U evaluated at $t = n\Delta t$ becomes

$$\frac{\partial U}{\partial t}(n\Delta t) = \frac{U|^{n+1/2} - U|^{n-1/2}}{\Delta t},$$

where $U|^n \equiv U(n\Delta t)$. To discretize the spatial derivatives, we assume that the fields are evaluated following the standard 2D Yee lattice for the transverse magnetic modes shown in Fig. 37. We denote a point (x, y) in Cartesian coordinates by two integers (i, j) where

$$(x, y) = (x_i, y_j) = \left(\sum_{p=1}^{i} \Delta x_p, \sum_{q=1}^{j} \Delta y_q \right)$$

where Δx_p and Δy_q are the dimensions of the pq-th Yee cell. If the grid is uniform such that Δx_p and Δy_q are independent of p and q, the expressions simplify and become $x_i = i\Delta x$ and $y_j = j\Delta y$. According to the Yee lattice, B_{zx} and B_{zy} are evaluated at (x_i, y_j), or more simply (i, j). Likewise, E_x and D_x are evaluated at $(i, j + 1/2)$ where

$j+1/2$ denotes the midpoint between y_j and $y_{j+1/2}$, and E_y and D_y are evaluated at $(i+1/2, j)$. Using these notations and suppressing the time dependence for now, the spatial derivatives of field components can be written as

$$\left.\frac{\partial B_z}{\partial x}\right|_{i+1/2,j} = \frac{B_z|_{i+1,j} - B_z|_{i,j}}{\Delta x_i} \tag{A.6}$$

$$\left.\frac{\partial Bz}{\partial y}\right|_{i,j+1/2} = \frac{B_z|_{i,j+1} - B_z|_{i,j}}{\Delta y_j}. \tag{A.7}$$

$$\left.\frac{\partial E_y}{\partial x}\right|_{i,j} = \frac{E_y|_{i+1/2,j} - E_y|_{i-1/2,j}}{[\Delta x_i + \Delta x_{i-1}]/2} \tag{A.8}$$

$$\left.\frac{\partial E_x}{\partial y}\right|_{i,j} = \frac{E_x|_{i,j+1/2} - E_x|_{i,j-1/2}}{[\Delta y_j + \Delta y_{j-1}]/2} \tag{A.9}$$

According to the Yee lattice, the separation between $E_y|_{i+1/2,j}$ and $E_y|_{i-1/2,j}$ is the average of Δx_i and Δx_{i-1}. Thus, the denominator of Eq. (A.8) is $[\Delta x_i + \Delta x_{i-1}]/2$ and not Δx_i. The denominator of Eq. (A.9) is $[(\Delta y_j + \Delta y_{j-1}]/2$ for an analogous reason.

Discretizing the time and spatial derivatives as above turns Eq. (A.1) through (A.4) into finite difference equations. Equation (A.1) becomes

$$\frac{E_y|^n_{i+1/2,j} - E_y|^n_{i-1/2,j}}{\Delta x_i} = -\frac{a_x}{c}\frac{B_{zx}|^{n+1/2}_{i,j} - B_{zx}|^{n-1/2}_{i,j}}{\Delta t} - \frac{\Omega_x}{c}\frac{B_{zx}|^{n+1/2}_{i,j} + B_{zx}|^{n-1/2}_{i,j}}{2}$$

where we have used $[B_{zx}|^{n+1/2}_{i,j} + B_{zx}|^{n-1/2}_{i,j}]/2$ to approximate $B_{zx}|^n_{i,j}$. This approximation is necessary since the magnetic field is only evaluated at $t = (n + 1/2)\Delta t$ but not at $t = n\Delta t$. Rearranging the expression yields

$$B_{zx}|^{n+1/2}_{i,j} = \frac{2a_x - \Omega_x\Delta t}{2a_x + \Omega_x\Delta t}B_{zx}|^{n-1/2}_{i,j} - \frac{2c\Delta t/\Delta x_i}{2a_x + \Omega_x\Delta t}\left(E_y|^n_{i+1/2,j} - E_y|^n_{i-1/2,j}\right). \tag{A.10}$$

Similarly, Eq. (A.2) becomes

$$B_{zy}|_{i,j}^{n+1/2} = \frac{2a_y - \Omega_y \Delta t}{2a_y + \Omega_y \Delta t} B_{zy}|_{i,j}^{n-1/2} + \frac{2c\Delta t/\Delta y_j}{2a_y + \Omega_y \Delta t} \left(E_x|_{i,j+1/2}^{n} - E_x|_{i,j-1/2}^{n} \right). \quad \text{(A.11)}$$

In FDTD, the two equations above are used to calculate the value of the magnetic field at time $(n + 1/2)\Delta t$ from its value at $(n - 1/2)\Delta t$ and the electric field at $n\Delta t$. Hence, these finite-difference equations constitute a part of the recursive algorithm for FDTD.

To obtain analogous recursive finite-difference equations for Eq. (A.3) and (A.4), we must first derive recursive equations for $\vec{D}$ and the time integral of $\vec{E}$. Let $t = n\Delta t$. Assuming $\vec{E}$ is zero for $t < 0$ and suppressing the spatial coordinates, Eq. (A.5) becomes

$$\begin{aligned} \vec{D}|^n &= \epsilon_\infty \vec{E}|^n + \int_0^{n\Delta t} \vec{E}(t')\chi(n\Delta t - t')dt' \\ &= \epsilon_\infty \vec{E}|^n + \int_0^{n\Delta t} \vec{E}(n\Delta t - t')\chi(t')dt' \\ &= \epsilon_\infty \vec{E}|^n + \sum_{m=0}^{n-1} \int_{m\Delta t}^{(m+1)\Delta t} \vec{E}(n\Delta t - t')\chi(t')dt'. \end{aligned}$$

To discretize the electric field inside the integral, we use a piecewise linear approximation to $\vec{E}(t)$ between $t \in [m\Delta t, (m+1)\Delta t]$:

$$\vec{E}(t) \approx \vec{E}|^{m+1} + \frac{\vec{E}|^{m+1} - \vec{E}|^m}{\Delta t} [t - (m+1)\Delta t].$$

Then

$$\vec{D}|^n = \epsilon_\infty \vec{E}|^n + \sum_{m=0}^{n-1} \left[\hat{\chi}|^m \vec{E}|^{n-m} + \hat{\xi}|^m \left(\vec{E}|^{n-m-1} - \vec{E}|^{n-m} \right) \right]$$

where

$$\begin{aligned}\hat{\chi}|^m &= \int_{m\Delta t}^{(m+1)\Delta t} \chi(t')dt' \\ \hat{\xi}|^m &= \frac{1}{\Delta t}\int_{m\Delta t}^{(m+1)\Delta t} (t' - m\Delta t)\chi(t')dt'.\end{aligned}$$

For the Debye model,

$$\begin{aligned}\hat{\chi}|^m &= \hat{\chi}_0 e^{-m\Delta t/\tau}; \qquad \hat{\chi}_0 = (\epsilon_s - \epsilon_\infty)\left[1 - e^{-\Delta t/\tau}\right] \\ \hat{\xi}|^m &= \hat{\xi}_0 e^{-m\Delta t/\tau}; \qquad \hat{\xi}_0 = (\epsilon_s - \epsilon_\infty)\frac{\tau}{\Delta t}\left[1 - \left(1 + \frac{\Delta t}{\tau}\right)e^{-\Delta t/\tau}\right].\end{aligned}$$

Let

$$\vec{\psi}|^n = \sum_{m=0}^{n-1}\left[\hat{\chi}|^m \vec{E}|^{n-m} + \hat{\xi}|^m\left(\vec{E}|^{n-m-1} - \vec{E}|^{n-m}\right)\right],$$

so that

$$\vec{D}|^n = \epsilon_\infty \vec{E}|^n + \vec{\psi}|^n. \tag{A.12}$$

At $t = (n+1)\Delta t$, the expressions for $\vec{\psi}$ and $\vec{D}$ are

$$\begin{aligned}\vec{\psi}|^{n+1} &= \sum_{m=0}^{n}\left[\hat{\chi}|^m \vec{E}|^{n-m+1} + \hat{\xi}|^m\left(\vec{E}|^{n-m} - \vec{E}|^{n-m+1}\right)\right] \\ &= \sum_{m=0}^{n}\left[\left(\hat{\chi}_0 - \hat{\xi}_0\right)\vec{E}|^{n+1-m} + \hat{\xi}_0\vec{E}|^{n-m}\right]e^{-m\Delta t/\tau} \\ &= \left(\hat{\chi}_0 - \hat{\xi}_0\right)\vec{E}|^{n+1} + \hat{\xi}_0\vec{E}|^n \\ &\quad + \sum_{m=1}^{n}\left[\left(\hat{\chi}_0 - \hat{\xi}_0\right)\vec{E}|^{n+1-m} + \hat{\xi}_0\vec{E}|^{n-m}\right]e^{-m\Delta t/\tau} \\ &= \left(\hat{\chi}_0 - \hat{\xi}_0\right)\vec{E}|^{n+1} + \hat{\xi}_0\vec{E}|^n + e^{-\Delta t/\tau}\vec{\psi}|^n \end{aligned} \tag{A.13}$$

and

$$\begin{aligned}\vec{D}|^{n+1} &= \epsilon_\infty \vec{E}|^{n+1} + \vec{\psi}|^{n+1} \\ &= \left(\epsilon_\infty + \hat{\chi}_0 - \hat{\xi}_0\right)\vec{E}|^{n+1} + \hat{\xi}_0 \vec{E}|^n + e^{-\Delta t/\tau}\vec{\psi}|^n, \end{aligned} \tag{A.14}$$

respectively. Equation (A.13) and (A.14) can be used to calculate $\vec{D}$ recursively.

Recursive equations for the time integral of $\vec{E}$ are calculated as follows. Since Eq. (A.3) and (A.4) are evaluated at $t = (n + 1/2)\Delta t$, we set the upper integration limit to $(n + 1/2)\Delta t$. Assuming again that $\vec{E} = 0$ when $t < 0$, the lower integration limit becomes zero. Then

$$\begin{aligned}\int_0^{(n+1/2)\Delta t} \vec{E}(t')dt' &= \int_0^{(n-1/2)\Delta t} \vec{E}(t')dt' + \int_{(n-1/2)\Delta t}^{n\Delta t} \vec{E}(t')dt' \\ &\quad + \int_{n\Delta t}^{(n+1/2)\Delta t} \vec{E}(t')dt' \\ &= \int_0^{(n-1/2)\Delta t} \vec{E}(t')dt' + \frac{\Delta t}{2}\left[\frac{\vec{E}|^n}{2} + \frac{1}{2}\frac{\vec{E}|^n + \vec{E}|^{n-1}}{2}\right] \\ &\quad + \frac{\Delta t}{2}\left[\frac{1}{2}\frac{\vec{E}|^{n+1} + \vec{E}|^n}{2} + \frac{\vec{E}|^n}{2}\right] \\ &= \int_0^{(n-1/2)\Delta t} \vec{E}(t')dt' + \frac{\Delta t}{8}\vec{E}|^{n+1} + \frac{3\Delta t}{4}\vec{E}|^n + \frac{\Delta t}{8}\vec{E}|^{n-1}\end{aligned}$$

where the trapezoid rule was employed to approximate two of the integrals. Rearranging the expression above yields

$$\vec{E}_I|^n = \vec{E}_I|^{n-1} + \frac{7}{8}\vec{E}|^n + \frac{1}{8}\vec{E}|^{n-1}$$

or

$$\vec{E}_I|^{n+1} = \vec{E}_I|^n + \frac{7}{8}\vec{E}|^{n+1} + \frac{1}{8}\vec{E}|^n \tag{A.15}$$

where $\vec{E}_I$ is defined as

$$\vec{E}_I|^n \equiv \frac{1}{\Delta t}\int_0^{(n+1/2)\Delta t} \vec{E}(t')dt' - \frac{1}{8}\vec{E}|^{n+1}.$$

Using the equations for $\vec{\psi}$ and $\vec{E}_I$ derived above, we now discretize Eq. (A.3);

$$\begin{aligned}
-c\frac{B_z|^{n+1/2}_{i+1,j} - B_z|^{n+1/2}_{i,j}}{\Delta x_i} &= a_x\frac{D_y|^{n+1}_{i+1/2,j} - D_y|^{n}_{i+1/2,j}}{\Delta t} + \Omega_x\frac{D_y|^{n+1}_{i+1/2,j} + D_y|^{n}_{i+1/2,j}}{2} \\
&\quad +4\pi\sigma a_x\frac{E_y|^{n+1}_{i+1/2,j} + E_y|^{n}_{i+1/2,j}}{2} \\
&\quad +4\pi\sigma\Omega_x\Delta t\left(E_{Iy}|^{n}_{i+1/2,j} + \frac{1}{8}E_y|^{n+1}_{i+1/2,j}\right) \\
&= \left(\frac{a_x}{\Delta t} + \frac{\Omega_x}{2}\right)\left([\epsilon_\infty + \hat{\chi}_0 + \hat{\xi}_0]E_y|^{n+1}_{i+1/2,j}\right. \\
&\qquad \left. +\hat{\xi}_0 E_y|^{n}_{i+1/2,j} + e^{-\Delta t/\tau}\psi_y|^{n}_{i+1/2,j}\right) \\
&\quad -\left(\frac{a_x}{\Delta t} - \frac{\Omega_x}{2}\right)\left(\epsilon_\infty E_y|^{n}_{i+1/2,j} + \psi_y|^{n}_{i+1/2,j}\right) \\
&\quad +4\pi\sigma a_x\frac{E_y|^{n+1}_{i+1/2,j} + E_y|^{n}_{i+1/2,j}}{2} \\
&\quad +4\pi\sigma\Omega_x\Delta t\left(E_{Iy}|^{n}_{i+1/2,j} + \frac{1}{8}E_y|^{n+1}_{i+1/2,j}\right) \\
&= \left\{\left(\frac{a_x}{\Delta t} + \frac{\Omega_x}{2}\right)[\epsilon_\infty + \hat{\chi}_0 + \hat{\xi}_0]\right. \\
&\qquad \left. +2\pi\sigma a_x + \frac{\pi\sigma\Omega_x\Delta t}{2}\right\}E_y|^{n+1}_{i+1/2,j} \\
&\quad -\left\{\left(\frac{a_x}{\Delta t} + \frac{\Omega_x}{2}\right)\hat{\xi}_0 - \left(\frac{a_x}{\Delta t} - \frac{\Omega_x}{2}\right)\epsilon_\infty\right. \\
&\qquad \left. +2\pi\sigma a_x\right\}E_y|^{n}_{i+1/2,j} \\
&\quad -\left\{\left(\frac{a_x}{\Delta t} - \frac{\Omega_x}{2}\right) - \left(\frac{a_x}{\Delta t} + \frac{\Omega_x}{2}\right)e^{-\Delta t/\tau}\right\}\psi_y|^{n}_{i+1/2,j} \\
&\quad +4\pi\sigma\Omega_x\Delta t E_{Iy}|^{n}_{i+1/2,j}.
\end{aligned}$$

By rearranging the expression, we obtain

$$E_y|_{i+1/2,j}^{n+1} = c_{Ey1}E_y|_{i+1/2,j}^{n} + c_{Ey2}\left(B_z|_{i+1,j}^{n+1/2} - B_z|_{i,j}^{n+1/2}\right) + c_{Ey3}\psi_y|_{i+1/2,j}^{n} + c_{Ey4}E_{Iy}|_{i+1/2,j}^{n}. \quad \text{(A.16)}$$

The four coefficients are defined as

$$\begin{aligned}
c_{Ey1} &= \left\{\left(\frac{a_x}{\Delta t}+\frac{\Omega_x}{2}\right)\hat{\xi}_0 - \left(\frac{a_x}{\Delta t}-\frac{\Omega_x}{2}\right)\epsilon_\infty + 2\pi\sigma a_x\right\}A_y \\
c_{Ey2} &= -\frac{c}{\Delta x_i}A_y \\
c_{Ey3} &= \left\{\left(\frac{a_x}{\Delta t}-\frac{\Omega_x}{2}\right) - \left(\frac{a_x}{\Delta t}+\frac{\Omega_x}{2}\right)e^{-\Delta t/\tau}\right\}A_y \\
c_{Ey4} &= -4\pi\sigma\Omega_x\Delta t A_y \\
A_y^{-1} &= \left\{\left(\frac{a_x}{\Delta t}+\frac{\Omega_x}{2}\right)[\epsilon_\infty + \hat{\chi}_0 + \hat{\xi}_0] + 2\pi\sigma a_x + \frac{\pi\sigma\Omega_x\Delta t}{2}\right\}.
\end{aligned}$$

A similar calculation gives a recursion relation for E_x

$$E_x|_{i,j+1/2}^{n+1} = c_{Ex1}E_x|_{i,j+1/2}^{n} + c_{Ex2}\left(B_z|_{i,j+1}^{n+1/2} - B_z|_{i,j}^{n+1/2}\right) + c_{Ex3}\psi_x|_{i,j+1/2}^{n} + c_{Ex4}E_{Ix}|_{i,j+1/2}^{n}. \quad \text{(A.17)}$$

$$\begin{aligned}
c_{Ex1} &= \left\{\left(\frac{a_y}{\Delta t}+\frac{\Omega_y}{2}\right)\hat{\xi}_0 - \left(\frac{a_y}{\Delta t}-\frac{\Omega_y}{2}\right)\epsilon_\infty + 2\pi\sigma a_y\right\}A_x \\
c_{Ex2} &= +\frac{c}{\Delta y_i}A_y \\
c_{Ex3} &= \left\{\left(\frac{a_y}{\Delta t}-\frac{\Omega_y}{2}\right) - \left(\frac{a_y}{\Delta t}+\frac{\Omega_y}{2}\right)e^{-\Delta t/\tau}\right\}A_x \\
c_{Ex4} &= -4\pi\sigma\Omega_y\Delta t A_x \\
A_x^{-1} &= \left\{\left(\frac{a_y}{\Delta t}+\frac{\Omega_y}{2}\right)[\epsilon_\infty + \hat{\chi}_0 + \hat{\xi}_0] + 2\pi\sigma a_y + \frac{\pi\sigma\Omega_y\Delta t}{2}\right\}.
\end{aligned}$$

In summary, the FDTD algorithm is derived for the perfectly matched layers for dispersive media with a nonuniform orthogonal Yee lattice. The algorithm is based

on the following nine recursive equations:

$$
\begin{aligned}
B_{zx}|_{i,j}^{n+1/2} &= c_{Bzx1} B_{zx}|_{i,j}^{n-1/2} + c_{Bzx2}\left(E_y|_{i+1/2,j}^{n} - E_y|_{i-1/2,j}^{n}\right) \\
B_{zy}|_{i,j}^{n+1/2} &= c_{Bzy1} B_{zy}|_{i,j}^{n-1/2} + c_{Bzy2}\left(E_x|_{i,j+1/2}^{n} - E_x|_{i,j-1/2}^{n}\right) \\
B_{z}|_{i,j}^{n+1/2} &= B_{zx}|_{i,j}^{n+1/2} + B_{zy}|_{i,j}^{n+1/2} \\
E_x|_{i,j+1/2}^{n+1} &= c_{Ex1} E_x|_{i,j+1/2}^{n} + c_{Ex2}\left(B_z|_{i,j+1}^{n+1/2} - B_z|_{i,j}^{n+1/2}\right) \\
&\qquad + c_{Ex3}\psi_x|_{i,j+1/2}^{n} + c_{Ex4} E_{Ix}|_{i,j+1/2}^{n} \\
E_y|_{i+1/2,j}^{n+1} &= c_{Ey1} E_y|_{i+1/2,j}^{n} + c_{Ey2}\left(B_z|_{i+1,j}^{n+1/2} - B_z|_{i,j}^{n+1/2}\right) \\
&\qquad + c_{Ey3}\psi_y|_{i+1/2,j}^{n} + c_{Ey4} E_{Iy}|_{i+1/2,j}^{n} \\
\psi_x|_{i,j+1/2}^{n+1} &= c_{\psi 1} E_x|_{i,j+1/2}^{n+1} + c_{\psi 2} E_x|_{i,j+1/2}^{n} + c_{\psi 3}\psi_x|_{i,j+1/2}^{n} \\
\psi_y|_{i+1/2,j}^{n+1} &= c_{\psi 1} E_y|_{i+1/2,j}^{n+1} + c_{\psi 2} E_y|_{i+1/2,j}^{n} + c_{\psi 3}\psi_y|_{i+1/2,j}^{n} \\
E_{Ix}|_{i,j+1/2}^{n+1} &= E_{Ix}|_{i,j+1/2}^{n} + \frac{7}{8} E_x|_{i,j+1/2}^{n+1} + \frac{1}{8} E_x|_{i,j+1/2}^{n} \\
E_{Iy}|_{i+1/2,j}^{n+1} &= E_{Iy}|_{i+1/2,j}^{n} + \frac{7}{8} E_y|_{i+1/2,j}^{n+1} + \frac{1}{8} E_y|_{i+1/2,j}^{n}
\end{aligned}
$$

where

$$
\begin{aligned}
c_{Bzx1} &= \frac{2a_x - \Omega_x \Delta t}{2a_x + \Omega_x \Delta t} \\
c_{Bzx2} &= -\frac{2c\Delta t/\Delta x_i}{2a_x + \Omega_x \Delta t} \\
c_{Bzy1} &= \frac{2a_y - \Omega_y \Delta t}{2a_y + \Omega_y \Delta t} \\
c_{Bzy2} &= +\frac{2c\Delta t/\Delta y_j}{2a_y + \Omega_y \Delta t}
\end{aligned}
$$

$$
\begin{aligned}
c_{Ex1} &= \left\{\left(\frac{a_y}{\Delta t}+\frac{\Omega_y}{2}\right)\hat{\xi}_0-\left(\frac{a_y}{\Delta t}-\frac{\Omega_y}{2}\right)\epsilon_\infty+2\pi\sigma a_y\right\}A_x \\
c_{Ex2} &= +\frac{c}{\Delta y_i}A_y \\
c_{Ex3} &= \left\{\left(\frac{a_y}{\Delta t}-\frac{\Omega_y}{2}\right)-\left(\frac{a_y}{\Delta t}+\frac{\Omega_y}{2}\right)e^{-\Delta t/\tau}\right\}A_x \\
c_{Ex4} &= -4\pi\sigma\Omega_y\Delta t A_x \\
A_x^{-1} &= \left\{\left(\frac{a_y}{\Delta t}+\frac{\Omega_y}{2}\right)[\epsilon_\infty+\hat{\chi}_0+\hat{\xi}_0]+2\pi\sigma a_y+\frac{\pi\sigma\Omega_y\Delta t}{2}\right\} \\
c_{Ey1} &= \left\{\left(\frac{a_x}{\Delta t}+\frac{\Omega_x}{2}\right)\hat{\xi}_0-\left(\frac{a_x}{\Delta t}-\frac{\Omega_x}{2}\right)\epsilon_\infty+2\pi\sigma a_x\right\}A_y \\
c_{Ey2} &= -\frac{c}{\Delta x_i}A_y \\
c_{Ey3} &= \left\{\left(\frac{a_x}{\Delta t}-\frac{\Omega_x}{2}\right)-\left(\frac{a_x}{\Delta t}+\frac{\Omega_x}{2}\right)e^{-\Delta t/\tau}\right\}A_y \\
c_{Ey4} &= -4\pi\sigma\Omega_x\Delta t A_y \\
A_y^{-1} &= \left\{\left(\frac{a_x}{\Delta t}+\frac{\Omega_x}{2}\right)[\epsilon_\infty+\hat{\chi}_0+\hat{\xi}_0]+2\pi\sigma a_x+\frac{\pi\sigma\Omega_x\Delta t}{2}\right\} \\
c_{\psi 1} &= \hat{\chi}_0-\hat{\xi}_0 \\
c_{\psi 2} &= \hat{\xi}_0 \\
c_{\psi 3} &= e^{-\Delta t/\tau}
\end{aligned}
$$

Although not explicit, the coefficients above depend on the coordinates (i, j).

APPENDIX B

FLAT-DISPERSION CONDITIONS FOR PLANAR, SPHERICAL, AND CYLINDRICAL METAL-DIELECTRIC-METAL GEOMETRIES

The plasmon enhanced absorption of the metal-dielectric-metal (MDM) microspheres presented in Chapter 4 are based on the existence of a band of transverse magnetic (TM) modes whose resonant frequencies are nearly identical. This band, called the flat band, is present in the dispersion diagram when the system satisfies the flat-dispersion condition,

$$L = L^{\star} \equiv \frac{\lambda_{sp}}{4\sqrt{\epsilon_d}},$$

where L is the thickness of the dielectric shell. The condition is independent of the metal core radius, R. Moreover, as stated in Chapter 4, the same condition also applies to planar and cylindrical MDM geometries. The existence of the flat-dispersion band in a planar MDM geometry was originally presented by H. Shin *et al.* in [100]. We have also shown[9] that the flat-dispersion band exists for spherical as well as cylindrical geometries, and that the conditions are identical to that of the planar geometry. In particular, our analysis has revealed that the conditions are independent of the radius of the metal core. In this Appendix, the flat-dispersion conditions are derived for planar, cylindrical, and spherical MDM systems, and it is shown explicitly that the conditions are identical for the three geometries.

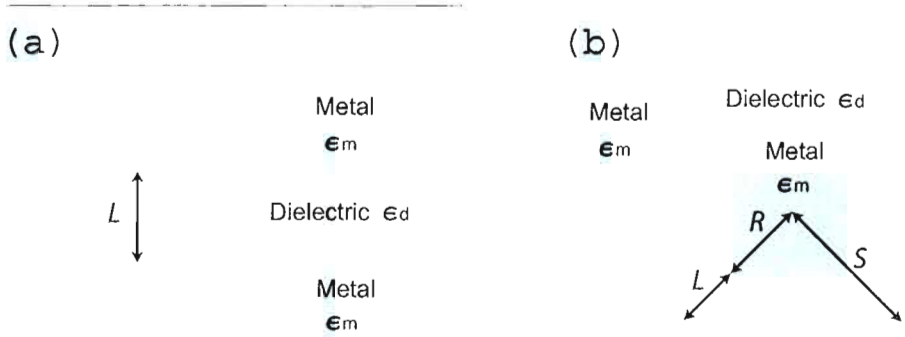

FIGURE 38. Schematic diagrams for the planar and spherical metal-dielectric-metal geometries.

The planar MDM geometry is shown in Fig. 38(a). For this system, the resonant frequencies of TM modes are given by

$$\begin{aligned} 0 &= -e^{-2L\sqrt{k^2-\epsilon_d\omega^2/c^2}}\left(\frac{1}{\epsilon_d}\sqrt{k^2-\epsilon_d\frac{\omega^2}{c^2}}-\frac{1}{\epsilon_m}\sqrt{k^2-\epsilon_m\frac{\omega^2}{c^2}}\right)^2 \\ &\quad+\left(\frac{1}{\epsilon_d}\sqrt{k^2-\epsilon_d\frac{\omega^2}{c^2}}+\frac{1}{\epsilon_m}\sqrt{k^2-\epsilon_m\frac{\omega^2}{c^2}}\right)^2 \end{aligned} \tag{B.1}$$

where k is the wavenumber, and ϵ_d and ϵ_m are the permittivity of the dielectric and metal, respectively. In the limit of $k \to \infty$, the exponential approaches zero, and the expression becomes $0 = k/\epsilon_d + k/\epsilon_m$, or

$$0 = \epsilon_d + \epsilon_m(\omega). \tag{B.2}$$

Since ϵ_m depends on frequency ω, the equation above determines the resonant frequencies of TM modes in the limit of $k \to \infty$.

To obtain the flat-dispersion band, we look for an expression for L such that Eq. (B.2) holds for small k. Let $k \ll \sqrt{\epsilon_d}\omega/c$, $|\sqrt{\epsilon_m}|\omega/c$ and $\epsilon_m(\omega) = -\epsilon_d$ in Eq. (B.1).

Then, to the first order in k, the equation becomes

$$\begin{aligned} 0 &= -e^{-i2L\sqrt{\epsilon_d}\omega/c}\left(\frac{i}{\sqrt{\epsilon_d}}+\frac{1}{\sqrt{\epsilon_d}}\right)^2+\left(\frac{i}{\sqrt{\epsilon_d}}-\frac{1}{\sqrt{\epsilon_d}}\right)^2+O[(k)^2] \\ &= -\frac{2i}{\sqrt{\epsilon_d}}\left(e^{-i2L\sqrt{\epsilon_d}\omega/c}+1\right)+O[(k)^2], \end{aligned}$$

or

$$(2n-1)\pi = 2L\sqrt{\epsilon_d}\frac{\omega}{c}$$

where $n \geq 1$ is the band index. The resonance modes given by Eq. (B.2) belong to the lowest TM band (i.e. $n = 1$). By setting $n = 1$, we obtain the flat-dispersion condition

$$L = L^\star \equiv \frac{\lambda_{sp}}{4\sqrt{\epsilon_d}} \tag{B.3}$$

with $\lambda_{sp} = 2\pi c/\omega_{sp}$ and ω_{sp} given by $0 = \epsilon_d + \epsilon_m(\omega_{sp})$. The subscript is added to ω to indicate that it is identical to the resonant frequency for SPPs on a flat metal surface. Therefore, when $L = L^\star$, the resonant frequencies of the modes belonging to the lowest TM band approach ω_{sp} in both limits of k (i.e. $k \to \infty$ and $k \to \infty$), causing the TM band to be flat.

For the spherical MDM geometry shown in Fig. 38(b), the TM mode frequencies are given by

$$\begin{aligned} 0 &= \left\{\frac{\epsilon_d j_l(k_dR)}{\epsilon_m j_l(k_mR)}-\frac{[k_dR\ j_l(k_dR)]'}{[k_mR\ j_l(k_mR)]'}\right\} \\ &\quad\times\left\{\frac{\epsilon_d h_l(k_dS)}{\epsilon_m h_l(k_mS)}-\frac{[k_dS\ h_l(k_dS)]'}{[k_mS\ h_l(k_mS)]'}\right\} \\ &\quad-\left\{\frac{\epsilon_d h_l(k_dR)}{\epsilon_m j_l(k_mR)}-\frac{[k_dR\ h_l(k_dR)]'}{[k_mR\ j_l(k_mR)]'}\right\} \\ &\quad\times\left\{\frac{\epsilon_d j_l(k_dS)}{\epsilon_m h_l(k_mS)}-\frac{[k_dS\ j_l(k_dS)]'}{[k_mS\ h_l(k_mS)]'}\right\}, \end{aligned} \tag{B.4}$$

with $k_{d,m} = \sqrt{\epsilon_{d,m}}\omega/c$, $S = R + L$, and j_l and h_l denoting the spherical Bessel and Hankel functions of the first kind, respectively. The prime denotes differentiation with respect to the argument. The metal core radius is denoted by R as shown in Fig. 38 Like the planar MDM case, L represents the thickness of the dielectric layer. Note that the positive integer l is a measure of the angular momentum, and takes the place of the wavenumber k in the planar geometry.

We first calculate the resonant condition in the limit of $l \to \infty$. For $l \gg |x|$,

$$\begin{aligned} j_l(x) &\approx \frac{x^l}{(2l+1)!!} \\ h_l(x) &\approx -i\frac{(2l-1)!!}{x^{l+1}}, \end{aligned}$$

with $(2l+1)!! = 1 \cdot 3 \cdot 5 \ldots (2l-3) \cdot (2l-1)$. Therefore, in the limit of the large multipole number l, we substitute the expressions above in Eq. (B.4)

$$\begin{aligned} 0 &= \left\{ \frac{\epsilon_d (k_d R)^l}{\epsilon_m (k_m R)^l} - \frac{[(k_d R)^{l+1}]'}{[(k_m R)^{l+1}]'} \right\} \left\{ \frac{\epsilon_d (k_d S)^{-(l+1)}}{\epsilon_m (k_m S)^{-(l+1)}} - \frac{[(k_d S)^{-l}]'}{[(k_m S)^{-l}]'} \right\} \\ &\quad - \left\{ \frac{\epsilon_d (k_d R)^{-(l+1)}}{\epsilon_m (k_m R)^l} - \frac{[(k_d R)^{-l}]'}{[(k_m R)^{l+1}]'} \right\} \left\{ \frac{\epsilon_d (k_d S)^l}{\epsilon_m (k_m S)^{-(l+1)}} - \frac{[(k_d S)^{l+1}]'}{[(k_m S)^{-l}]'} \right\} \\ &= \frac{k_d^{-1}}{k_m^{-1}} \left(\frac{\epsilon_d}{\epsilon_m} - 1 \right)^2 - \frac{k_d^{-1}}{k_m^{-1}} \left(\frac{\epsilon_d}{\epsilon_m} + \frac{l}{l+1} \right) \left(\frac{\epsilon_d}{\epsilon_m} + \frac{l+1}{l} \right) \underbrace{\left(1 + \frac{L}{R} \right)^{2l+1}}_{\to\infty \text{ as } l \to \infty}, \end{aligned}$$

and obtain

$$0 = \epsilon_d + \epsilon_m(\omega), \tag{B.5}$$

which is identical to Eq. (B.2).

To derive the flat-dispersion condition, we look for a condition for L such that Eq. (B.5) also holds for low multipole modes with $l \ll k_d R, |k_m R|$. We assume that

R is at least comparable to the wavelength such that $k_dR, |k_mR| >> 1$. Then, by employing the asymptotic forms of the spherical Bessel and Hankel functions valid for $|x| \gg l$,

$$\begin{aligned} j_l(x) &\approx \frac{\sin(x-\frac{\pi l}{2})}{x} \\ h_l(x) &\approx (-i)^{l+1}\frac{e^{ix}}{x}, \end{aligned} \tag{B.6}$$

Eq. (B.4) becomes

$$\begin{aligned} 0 &= \left\{ \frac{\epsilon_d \frac{1}{k_dR}\sin(k_dR-\frac{\pi l}{2})}{-\epsilon_d \frac{1}{ik_dR}\sin(ik_dR-\frac{\pi l}{2})} - \frac{\cos(k_dR-\frac{\pi l}{2})}{\cos(ik_dR-\frac{\pi l}{2})} \right\} \\ &\quad \times \left\{ \frac{\epsilon_d \frac{(-i)^{l+1}}{k_dS}e^{ik_dS}}{-\epsilon_d \frac{(-i)^{l+1}}{ik_dS}e^{-k_dS}} - \frac{(-i)^l e^{ik_dS}}{(-i)^l e^{-k_dS}} \right\} \\ &\quad - \left\{ \frac{\epsilon_d \frac{(-i)^{l+1}}{k_dR}e^{ik_dR}}{-\epsilon_d \frac{1}{ik_dR}\sin(ik_dR-\frac{\pi l}{2})} - \frac{(-i)^l e^{ik_dR}}{\cos(ik_dR-\frac{\pi l}{2})} \right\} \\ &\quad \times \left\{ \frac{\epsilon_d \frac{1}{k_dS}\sin(k_dS-\frac{\pi l}{2})}{-\epsilon_d \frac{(-i)^{l+1}}{ik_dS}e^{-k_dS}} - \frac{\cos(k_dS-\frac{\pi l}{2})}{(-i)^l e^{-k_dS}} \right\} \\ &= \left\{ -i\frac{\sin(k_dR-\frac{\pi l}{2})}{\sin(ik_dR-\frac{\pi l}{2})} - \frac{\cos(k_dR-\frac{\pi l}{2})}{\cos(ik_dR-\frac{\pi l}{2})} \right\} \\ &\quad \times \left\{ -i\frac{e^{ik_dS}}{e^{-k_dS}} - \frac{e^{ik_dS}}{e^{-k_dS}} \right\} \\ &\quad - \left\{ -\frac{e^{ik_dR}}{\sin(ik_dR-\frac{\pi l}{2})} - \frac{e^{ik_dR}}{\cos(ik_dR-\frac{\pi l}{2})} \right\} \\ &\quad \times \left\{ \frac{\sin(k_dS-\frac{\pi l}{2})}{e^{-k_dS}} - \frac{\cos(k_dS-\frac{\pi l}{2})}{e^{-k_dS}} \right\}. \end{aligned}$$

Since $k_dR \gg 1$,

$$\begin{aligned} \cos\left(ik_dR-\frac{\pi l}{2}\right) &\approx \frac{1}{2}e^{-i\left(ik_dR-\frac{\pi l}{2}\right)} \\ \sin\left(ik_dR-\frac{\pi l}{2}\right) &\approx \frac{i}{2}e^{-i\left(ik_dR-\frac{\pi l}{2}\right)}. \end{aligned}$$

Substituting these approximate expressions yields

$$
\begin{aligned}
0 &= 2e^{ik_dS+k_dS}\left[\left\{i\frac{\sin(k_dR-\frac{\pi l}{2})}{ie^{-i(ik_dR-\frac{\pi l}{2})}}+\frac{\cos(k_dR-\frac{\pi l}{2})}{e^{-i(ik_dR-\frac{\pi l}{2})}}\right\}\{i+1\}\right. \\
&\qquad -\left\{-\frac{1}{ie^{-i(ik_dR-\frac{\pi l}{2})}}-\frac{1}{e^{-i(ik_dR-\frac{\pi l}{2})}}\right\} \\
&\qquad\qquad \left.\times\left\{\sin\left(k_dS-\frac{\pi l}{2}\right)-\cos\left(k_dS-\frac{\pi l}{2}\right)\right\}e^{-ik_dL}\right] \\
&= 2e^{ik_dS+k_dL-i\frac{\pi l}{2}}(1+i)\left[\left\{\sin\left(k_dR-\frac{\pi l}{2}\right)+\cos\left(k_dR-\frac{\pi l}{2}\right)\right\}\right. \\
&\qquad\qquad \left.-i\left\{\sin\left(k_dS-\frac{\pi l}{2}\right)-\cos\left(k_dS-\frac{\pi l}{2}\right)\right\}e^{-ik_dL}\right] \\
&= e^{ik_dS+k_dL-i\frac{\pi l}{2}}(1+i)\left[(-i+1)e^{i\left(k_dR-\frac{\pi l}{2}\right)}+(i+1)e^{-i\left(k_dR-\frac{\pi l}{2}\right)}\right. \\
&\qquad\qquad \left.+(-1+i)e^{i\left(k_dR-\frac{\pi l}{2}\right)}+(1+i)e^{-i\left(k_dR+2ik_dL-\frac{\pi l}{2}\right)}\right] \\
&= e^{k_dL}(1+i)^2\left[e^{ik_dL}+e^{-ik_dL}\right],
\end{aligned}
$$

which reduces to $\cos(k_dL)=0$, or $(2n-1)\pi=2k_dL$ where $n\geq 1$ is the band index. The higher multipole TM modes of Eq. (B.5) belong to the lowest band. Thus, letting $n=1$ yields the flat-dispersion condition for the spherical geometry,

$$L=L^{\star}\equiv\frac{\lambda_{sp}}{4\sqrt{\epsilon_d}}, \tag{B.7}$$

which is identical to the planar case.

The cylindrical MDM geometry does not permit pure TM and TE modes in general[99]. However, there are two cases for which pure TM and TE modes exist:

Case I: wave vector $\vec{k}$ orthogonal to $\hat{z}$,

Case II: wave vector $\vec{k}$ orthogonal to $\hat{\phi}$.

Here, $\hat{z}$ and $\hat{\phi}$ are unit vectors pointing in the axial and angular directions of the cylindrical geometry. We consider these two cases separately below. For Case I, the resonant frequencies of TM modes are determined by

$$\begin{aligned} 0 &= \left\{ \frac{\sqrt{\epsilon_d}}{\sqrt{\epsilon_m}} \frac{J_l(k_m R)}{J_l(k_d R)} - \frac{J_l'(k_m R)}{J_l'(k_d R)} \right\} \\ &\quad \times \left\{ \frac{\sqrt{\epsilon_d}}{\sqrt{\epsilon_m}} \frac{H_l(k_m S)}{H_l(k_d S)} - \frac{H_l'(k_m S)}{H_l'(k_d S)} \right\} \\ &\quad - \left\{ \frac{\sqrt{\epsilon_d}}{\sqrt{\epsilon_m}} \frac{H_l(k_m R)}{J_l(k_d R)} - \frac{H_l'(k_m R)}{J_l'(k_d R)} \right\} \\ &\quad \times \left\{ \frac{\sqrt{\epsilon_d}}{\sqrt{\epsilon_m}} \frac{J_l(k_m S)}{H_l(k_d S)} - \frac{J_l'(k_m S)}{H_l'(k_d S)} \right\} \end{aligned} \tag{B.8}$$

where l is a non-negative integer, and J_l and H_l denote the cylindrical Bessel and Hankel functions of the first kind, respectively. The geometric parameters R, L and S are defined as the spherical case.

We first let $l \to \infty$. In this limit, the Hankel and Bessel functions, valid for $|x| \ll l$, are approximated by

$$\begin{aligned} J_l(x) &\approx \frac{1}{l!} \left(\frac{x}{2} \right)^n \\ H_l(x) &\approx -i \frac{(l-1)!}{\pi} \left(\frac{2}{x} \right)^n . \end{aligned}$$

Then, Eq. (B.8) reduces to

$$0 = \left\{ \frac{\epsilon_d}{\epsilon_m} - 1 \right\} \left\{ 1 - \frac{\epsilon_m}{\epsilon_d} \right\} - \left\{ \frac{\sqrt{\epsilon_d}}{\sqrt{\epsilon_m}} + \frac{\sqrt{\epsilon_m}}{\sqrt{\epsilon_d}} \right\}^2 \underbrace{\left(1 + \frac{L}{R} \right)^{2l}}_{\to \infty \text{ as } l \to \infty} .$$

From the expression above, we obtain a familiar expression

$$0 = \epsilon_d + \epsilon_m(\omega). \tag{B.9}$$

As for the planar and spherical cases, we now look for a condition for L such that Eq. (B.9) is satisfied for TM modes with small l such that $k_dR, |k_mR| \gg 1, l$. Then, by employing the asymptotic forms of the functions appropriate for $|x| \gg 1$,

$$J_l(x) \approx \sqrt{\frac{2}{\pi x}}\,\cos\left(x - \frac{(2l+1)\pi}{4}\right) \tag{B.10}$$

$$H_l(x) \approx \sqrt{\frac{2}{\pi x}}\,e^{i\left(x-\frac{(2l+1)\pi}{4}\right)}, \tag{B.11}$$

Eq. (B.8) reads

$$\begin{aligned}
0 = & \left\{ \frac{\sqrt{\epsilon_d}}{\sqrt{-\epsilon_d}} \frac{\sqrt{\frac{2}{\pi k_d R}}\cos\left(k_dR - \frac{(2l+1)\pi}{4}\right)}{\sqrt{\frac{2}{i\pi k_d R}}\cos\left(ik_dR - \frac{(2l+1)\pi}{4}\right)} - \frac{-\sqrt{\frac{2}{\pi k_d R}}\sin\left(k_dR - \frac{(2l+1)\pi}{4}\right)}{-\sqrt{\frac{2}{i\pi k_d R}}\sin\left(ik_dR - \frac{(2l+1)\pi}{4}\right)} \right\} \\
& \times \left\{ \frac{\sqrt{\epsilon_d}}{\sqrt{-\epsilon_d}} \frac{\sqrt{\frac{2}{\pi k_d S}}e^{i\left(k_dS - \frac{(2l+1)\pi}{4}\right)}}{\sqrt{\frac{2}{i\pi k_d S}}e^{i\left(ik_dS - \frac{(2l+1)\pi}{4}\right)}} - \frac{i\sqrt{\frac{2}{\pi k_d S}}e^{i\left(k_dS - \frac{(2l+1)\pi}{4}\right)}}{i\sqrt{\frac{2}{i\pi k_d S}}e^{i\left(ik_dS - \frac{(2l+1)\pi}{4}\right)}} \right\} \\
& - \left\{ \frac{\sqrt{\epsilon_d}}{\sqrt{-\epsilon_d}} \frac{\sqrt{\frac{2}{\pi k_d R}}e^{i\left(k_dR - \frac{(2l+1)\pi}{4}\right)}}{\sqrt{\frac{2}{i\pi k_d R}}\cos\left(ik_dR - \frac{(2l+1)\pi}{4}\right)} - \frac{i\sqrt{\frac{2}{\pi k_d R}}e^{i\left(k_dR - \frac{(2l+1)\pi}{4}\right)}}{-\sqrt{\frac{2}{i\pi k_d R}}\sin\left(ik_dR - \frac{(2l+1)\pi}{4}\right)} \right\} \\
& \times \left\{ \frac{\sqrt{\epsilon_d}}{\sqrt{-\epsilon_d}} \frac{\sqrt{\frac{2}{\pi k_d S}}\cos\left(k_dS - \frac{(2l+1)\pi}{4}\right)}{\sqrt{\frac{2}{i\pi k_d S}}e^{i\left(ik_dS - \frac{(2l+1)\pi}{4}\right)}} - \frac{-\sqrt{\frac{2}{\pi k_d S}}\sin\left(k_dS - \frac{(2l+1)\pi}{4}\right)}{i\sqrt{\frac{2}{i\pi k_d S}}e^{i\left(ik_dS - \frac{(2l+1)\pi}{4}\right)}} \right\} \\
= & \sqrt{i}\left\{ -i\frac{\cos\left(k_dR - \frac{(2l+1)\pi}{4}\right)}{\cos\left(ik_dR - \frac{(2l+1)\pi}{4}\right)} - \frac{\sin\left(k_dR - \frac{(2l+1)\pi}{4}\right)}{\sin\left(ik_dR - \frac{(2l+1)\pi}{4}\right)} \right\} \\
& \times \left\{ -i\frac{e^{i\left(k_dS - \frac{(2l+1)\pi}{4}\right)}}{e^{i\left(ik_dS - \frac{(2l+1)\pi}{4}\right)}} - \frac{e^{i\left(k_dS - \frac{(2l+1)\pi}{4}\right)}}{e^{i\left(ik_dS - \frac{(2l+1)\pi}{4}\right)}} \right\} \\
& -\sqrt{i}\left\{ -i\frac{e^{i\left(k_dR - \frac{(2l+1)\pi}{4}\right)}}{\cos\left(ik_dR - \frac{(2l+1)\pi}{4}\right)} + i\frac{e^{i\left(k_dR - \frac{(2l+1)\pi}{4}\right)}}{\sin\left(ik_dR - \frac{(2l+1)\pi}{4}\right)} \right\} \\
& \times \left\{ -i\frac{\cos\left(k_dS - \frac{(2l+1)\pi}{4}\right)}{e^{i\left(ik_dS - \frac{(2l+1)\pi}{4}\right)}} - i\frac{\sin\left(k_dS - \frac{(2l+1)\pi}{4}\right)}{e^{i\left(ik_dS - \frac{(2l+1)\pi}{4}\right)}} \right\}.
\end{aligned}$$

Since $k_dR \gg 1$,

$$\begin{aligned}\cos\left(ik_dR - \frac{(2l+1)\pi}{4}\right) &\approx \frac{1}{2}e^{-i\left(ik_dR - \frac{(2l+1)\pi}{4}\right)} \\ \sin\left(ik_dR - \frac{(2l+1)\pi}{4}\right) &\approx \frac{i}{2}e^{-i\left(ik_dR - \frac{(2l+1)\pi}{4}\right)}.\end{aligned}$$

Thus,

$$\begin{aligned}0 &= \sqrt{i}\frac{e^{i\left(k_dR - \frac{(2l+1)\pi}{4}\right)}}{e^{i\left(ik_dS - \frac{(2l+1)\pi}{4}\right)}}\left[\left\{i\frac{\cos\left(k_dR - \frac{(2l+1)\pi}{4}\right)}{\frac{1}{2}e^{-i\left(ik_dR - \frac{(2l+1)\pi}{4}\right)}} + \frac{\sin\left(k_dR - \frac{(2l+1)\pi}{4}\right)}{\frac{i}{2}e^{-i\left(ik_dR - \frac{(2l+1)\pi}{4}\right)}}\right\}\right. \\ &\qquad \times \left\{i\frac{e^{ik_dL}}{1} + \frac{e^{ik_dL}}{1}\right\} \\ &\qquad -\left\{-\frac{1}{\frac{1}{2}e^{-i\left(ik_dR - \frac{(2l+1)\pi}{4}\right)}} + \frac{1}{\frac{i}{2}e^{-i\left(ik_dR - \frac{(2l+1)\pi}{4}\right)}}\right\} \\ &\qquad \left.\times \left\{\frac{\cos\left(k_dS - \frac{(2l+1)\pi}{4}\right)}{1} + \frac{\sin\left(k_dS - \frac{(2l+1)\pi}{4}\right)}{1}\right\}\right] \\ &= 2\sqrt{i}e^{ik_dS + k_dL - i\frac{(2l+1)\pi}{4}} \\ &\qquad \times \left[\left\{i\cos\left(k_dR - \frac{(2l+1)\pi}{4}\right) - i\sin\left(k_dR - \frac{(2l+1)\pi}{4}\right)\right\}\{i+1\}\right. \\ &\qquad \left. -\{-1-i\}\left\{\cos\left(k_dS - \frac{(2l+1)\pi}{4}\right) + \sin\left(k_dS - \frac{(2l+1)\pi}{4}\right)\right\}e^{-ik_dL}\right] \\ &= \sqrt{i}e^{ik_dS + k_dL - i\frac{(2l+1)\pi}{4}}(1+i)\left[(i-1)e^{i\left(k_dR - \frac{(2l+1)\pi}{4}\right)} + (i+1)e^{-i\left(k_dR - \frac{(2l+1)\pi}{4}\right)}\right. \\ &\qquad \left. +(1-i)e^{i\left(k_dR - \frac{(2l+1)\pi}{4}\right)} + (1+i)e^{-i\left(k_dR + 2k_dL - \frac{(2l+1)\pi}{4}\right)}\right] \\ &= \sqrt{i}e^{k_dL}(1+i)^2\left[e^{ik_dL} + e^{-ik_dL}\right],\end{aligned}$$

which simplifies to $\cos(k_dL) = 0$, or $(2n-1)\pi = 2k_dL$. Choosing $n = 1$, we obtain the flat-dispersion condition for Case I of the cylindrical MDM geometry,

$$L = L^\star \equiv \frac{\lambda_{sp}}{4\sqrt{\epsilon_d}}. \tag{B.12}$$

The dispersion relations of the TM modes in Case II are determined by

$$
\begin{aligned}
0 \;=\; & \left\{ \frac{\frac{\lambda_d}{\epsilon_d} J_0(\lambda_d R)}{\frac{\lambda_m}{\epsilon_m} J_0(\lambda_m R)} - \frac{J_0'(\lambda_d R)}{J_0'(\lambda_m R)} \right\} \\
& \times \left\{ \frac{\frac{\lambda_d}{\epsilon_d} H_0(\lambda_d S)}{\frac{\lambda_m}{\epsilon_m} H_0(\lambda_m S)} - \frac{H_0'(\lambda_d S)}{H_0'(\lambda_m S)} \right\} \\
& - \left\{ \frac{\frac{\lambda_d}{\epsilon_d} H_0(\lambda_d R)}{\frac{\lambda_m}{\epsilon_m} J_0(\lambda_m R)} - \frac{H_0'(\lambda_d R)}{J_0'(\lambda_m R)} \right\} \\
& \times \left\{ \frac{\frac{\lambda_d}{\epsilon_d} J_0(\lambda_d S)}{\frac{\lambda_m}{\epsilon_m} H_0(\lambda_m S)} - \frac{J_0'(\lambda_d S)}{H_0'(\lambda_m S)} \right\}
\end{aligned}
\tag{B.13}
$$

with $\lambda_{d,m} = \sqrt{k_{d,m}^2 - k_z^2}$ and k_z is the z component of $\vec{k}$. We assume that R is at least comparable to the wavelength. Then in the limit of $k_z \to 0$ and also $k_z \to \infty$, $|\lambda_{d,m}|R \gg 1$ and we can approximate the Bessel and Hankel functions with Eq. (B.10) and Eq. (B.11), respectively. Equation (B.13) now reads

$$
\begin{aligned}
0 \;=\; & \left\{ \frac{\frac{\lambda_d}{\epsilon_d}\sqrt{\frac{2}{\pi\lambda_d R}}\cos(\lambda_d R - \frac{\pi}{4})}{\frac{\lambda_m}{\epsilon_m}\sqrt{\frac{2}{\pi\lambda_m R}}\cos(\lambda_m R - \frac{\pi}{4})} - \frac{-\sqrt{\frac{2}{\pi\lambda_d R}}\sin(\lambda_d R - \frac{\pi}{4})}{-\sqrt{\frac{2}{\pi\lambda_m R}}\sin(\lambda_m R - \frac{\pi}{4})} \right\} \\
& \times \left\{ \frac{\frac{\lambda_d}{\epsilon_d}\sqrt{\frac{2}{\pi\lambda_d S}}e^{i(\lambda_d S - \frac{\pi}{4})}}{\frac{\lambda_m}{\epsilon_m}\sqrt{\frac{2}{\pi\lambda_m S}}e^{i(\lambda_m S - \frac{\pi}{4})}} - \frac{i\sqrt{\frac{2}{\pi\lambda_d S}}e^{i(\lambda_d S - \frac{\pi}{4})}}{i\sqrt{\frac{2}{\pi\lambda_m S}}e^{i(\lambda_m S - \frac{\pi}{4})}} \right\} \\
& - \left\{ \frac{\frac{\lambda_d}{\epsilon_d}\sqrt{\frac{2}{\pi\lambda_d R}}e^{i(\lambda_d R - \frac{\pi}{4})}}{\frac{\lambda_m}{\epsilon_m}\sqrt{\frac{2}{\pi\lambda_m R}}\cos(\lambda_m R - \frac{\pi}{4})} - \frac{i\sqrt{\frac{2}{\pi\lambda_d R}}e^{i(\lambda_d R - \frac{\pi}{4})}}{-\sqrt{\frac{2}{\pi\lambda_m R}}\sin(\lambda_m R - \frac{\pi}{4})} \right\} \\
& \times \left\{ \frac{\frac{\lambda_d}{\epsilon_d}\sqrt{\frac{2}{\pi\lambda_d S}}\cos(\lambda_d S - \frac{\pi}{4})}{\frac{\lambda_m}{\epsilon_m}\sqrt{\frac{2}{\pi\lambda_m S}}e^{i(\lambda_m S - \frac{\pi}{4})}} - \frac{-\sqrt{\frac{2}{\pi\lambda_d S}}\sin(\lambda_d S - \frac{\pi}{4})}{i\sqrt{\frac{2}{\pi\lambda_m S}}e^{i(\lambda_m S - \frac{\pi}{4})}} \right\} \\
= \; & 2\frac{\lambda_m}{\lambda_d} e^{i(\lambda_d S - \lambda_m L - \frac{\pi}{4})} \\
& \times \left[\left\{ \frac{\frac{\lambda_d}{\epsilon_d}}{\frac{\lambda_m}{\epsilon_m}} \cos\left(\lambda_d R - \frac{\pi}{4}\right) + i\sin\left(\lambda_d R - \frac{\pi}{4}\right) \right\} \left\{ \frac{\frac{\lambda_d}{\epsilon_d}}{\frac{\lambda_m}{\epsilon_m}} - 1 \right\} \right. \\
& \left. - \left\{ \frac{\frac{\lambda_d}{\epsilon_d}}{\frac{\lambda_m}{\epsilon_m}} + 1 \right\} \left\{ \frac{\frac{\lambda_d}{\epsilon_d}}{\frac{\lambda_m}{\epsilon_m}} \cos\left(\lambda_d S - \frac{\pi}{4}\right) - i\sin\left(\lambda_d S - \frac{\pi}{4}\right) \right\} e^{-i\lambda_d L} \right].
\end{aligned}
\tag{B.14}
$$

As $k_z \to \infty$, $\lambda_{d,m} \to ik_z$ and Eq. (B.14) reduces to

$$\begin{aligned} 0 &= e^{i(ik_zS - ik_zL - \frac{\pi}{4})} \left[\left(\frac{\epsilon_m}{\epsilon_d} e^{-i\left(ik_zR - \frac{\pi}{4}\right)} - e^{-i\left(ik_zR - \frac{\pi}{4}\right)} \right) \left(\frac{\epsilon_m}{\epsilon_d} - 1 \right) \right. \\ &\qquad \left. - \left(\frac{\epsilon_m}{\epsilon_d} + 1 \right) \left(\frac{\epsilon_m}{\epsilon_d} e^{-i\left(ik_zS - \frac{\pi}{4}\right)} + e^{-i\left(ik_zS - \frac{\pi}{4}\right)} \right) e^{k_zL} \right] \\ &= \left(\frac{\epsilon_m}{\epsilon_d} - 1 \right)^2 - \left(\frac{\epsilon_m}{\epsilon_d} + 1 \right)^2 e^{2k_zL}, \end{aligned} \tag{B.15}$$

hence

$$0 = \epsilon_d + \epsilon_m(\omega). \tag{B.16}$$

In the limit of $k_z \to 0$,

$$\lambda_{d,m} = k_{d,m} + O[(k_z)^2].$$

Assuming that Eq. (B.16) is also satisfied in this limit, the flat-dispersion condition is derived from Eq. (B.14):

$$\begin{aligned} 0 &= 2ie^{i(k_dS - ik_dL - \frac{\pi}{4})} \left[\left\{ i\cos\left(k_dR - \frac{\pi}{4}\right) + i\sin\left(k_dR - \frac{\pi}{4}\right) \right\} \{i-1\} \right. \\ &\qquad \left. - \{i+1\} \left\{ i\cos\left(k_dS - \frac{\pi}{4}\right) - i\sin\left(k_dS - \frac{\pi}{4}\right) \right\} e^{-ik_dL} \right] \\ &= e^{i(k_dS - ik_dL - \frac{\pi}{4})}(1-i) \left[(1-i)e^{i\left(k_dR - \frac{\pi}{4}\right)} + (1+i)e^{-i\left(k_dR - \frac{\pi}{4}\right)} \right. \\ &\qquad \left. + (i-1)e^{i\left(k_dR - \frac{\pi}{4}\right)} + (i+1)e^{-i\left(k_dR - 2k_dL - \frac{\pi}{4}\right)} \right] \\ &= e^{k_dL}(1-i)(1+i)\left[e^{ik_dL} + e^{-ik_dL} \right] \\ &= 4e^{k_dL}\cos(k_dL). \end{aligned} \tag{B.17}$$

Therefore, the flat-dispersion condition is

$$L = L^\star \equiv \frac{\lambda_{sp}}{4\sqrt{\epsilon_d}}. \tag{B.18}$$

for Case II as well.

We have demonstrated that the flat-dispersion condition is identical for planar, spherical, and cylindrical MDM geometries. This result suggests that the flat-dispersion band is not specific to a particular geometry, and that any MDM system may exhibit a flat-dispersion band as long as its local radius curvature is at least comparable to the wavelength and if $L = \lambda_{sp}/4\sqrt{\epsilon_d}$.

APPENDIX C

RECURSIVE MIE ALGORITHM FOR MULTILAYERED SPHERICAL PARTICLES

The theory of light scattering by a spherical particle, commonly known as the Mie theory or the Mie solution, was developed by Gustav Mie one hundred years ago[128]. It is an exact solution to Maxwell's equations in the spherical coordinates with an incident plane-wave as the boundary condition. Mie's original work was concerned with homogeneous particles. Later, the theory was extended for coated spheres[129] and multilayered spheres[130]. The objective of the theory is to calculate the scattering coefficients, a_n and b_n, which may be used to obtain the electromagnetic field distribution as well as the scattering and extinction coefficients via

$$\sigma_{sca} = \frac{2\pi}{k^2}\sum_{n=1}^{\infty}(2n+1)\left[|a_n|^2+|b_n|^2\right] \tag{C.1}$$

$$\sigma_{ext} = \frac{2\pi}{k^2}\sum_{n=1}^{\infty}(2n+1)\mathrm{Re}\left[a_n+b_n\right], \tag{C.2}$$

where k is the wavenumber.

There are a few difficulties associated with using the Mie theory to obtain numerical values of a_n and b_n. First, as the number layer L increases, the calculation becomes complicated very rapidly because it essentially requires computing the determinants of four $2L \times 2L$ matrices. Second, if the layers are absorptive and if the

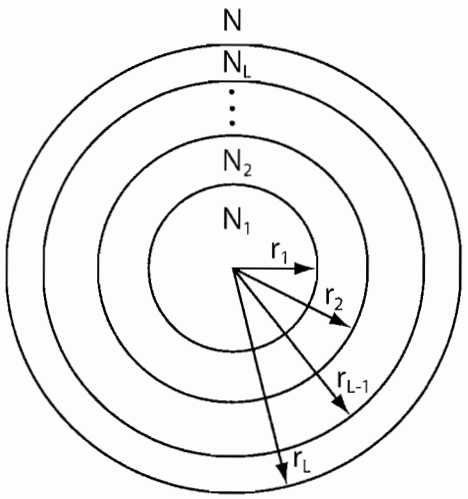

FIGURE 39. Schematic diagram for the L-layered spherical particle. Each layer has the index of refraction N_i and the outer radius r_i. The sphere is embedded in a homogeneous medium with index N.

wavelength is comparable or greater than the radius of the sphere, the solution often involves subtraction of two large but nearly identical numbers, causing their difference to be numerically inaccurate. Moreover, the expressions for a_n and b_n contain the spherical Bessel functions of a complex argument. These functions grow exponentially with their argument, and may lead to computer overflow. Over the years, much work has been published to address these issues[104, 107, 108, 131]. We have found the work of T. Kaiser and G. Schweiger[105] and by W. Yang[106] particularly appealing for their efficiency and ease of computer programming implementation. In this Appendix, we present an efficient and stable recursive Mie algorithm for a spherical particle with an arbitrary number of layers, which we developed based on their work.

Considered a sphere with L concentric layers as shown in Fig. 39. The l-th layer has the refractive index of N_l, and inner and outer radii of r_{l-1} and r_l, respectively,

where $l = 1, 2, \ldots L$ The sphere is embedded in a lossless dielectric host with an index of refraction N. Let the incident light be an x-polarized plane wave $\vec{E}_i = E_o e^{ikz}\hat{x}$, or

$$\vec{E}_i = E_0 \sum_{n=1}^{\infty} i^n \frac{2n+1}{n(n+1)} \left[\vec{M}_{o1n}^{(1)} - i\vec{N}_{e1n}^{(1)}\right] \tag{C.3}$$

using the spherical wave expansion[132]. Throughout this appendix, we suppress the $e^{-i\omega}t$ time dependence. The scattered field can be written in terms of the scattering coefficients a_n and b_n as

$$\vec{E}_s = E_0 \sum_{n=1}^{\infty} i^n \frac{2n+1}{n(n+1)} \left[ia_n\vec{N}_{e1n}^{(3)} - b_n\vec{M}_{o1n}^{(3)}\right]. \tag{C.4}$$

Here, $\vec{M}_{o1n}^{(j)}$, $\vec{M}_{e1n}^{(j)}$, $\vec{N}_{o1n}^{(j)}$, and $\vec{N}_{e1n}^{(j)}$ are the vector spherical harmonics. The superscripts $j = 1, 3$ signify that their radial dependence is specified by both the Bessel function for $j = 1$ and the Hankel function of the first kind for $j = 3$. The solution to Maxwell's equations in the l-th region are

$$\vec{E}_l = E_0 \sum_{n=1}^{\infty} i^n \frac{2n+1}{n(n+1)} \left[c_n^{(l)}\vec{M}_{o1n}^{(1)} - id_n^{(l)}\vec{N}_{e1n}^{(1)} + ia_n^{(l)}\vec{N}_{e1n}^{(3)} - b_n^{(l)}\vec{M}_{o1n}^{(3)}\right] \tag{C.5}$$

$$\vec{H}_l = -\frac{k_l c}{\omega} E_0 \sum_{n=1}^{\infty} i^n \frac{2n+1}{n(n+1)} \left[d_n^{(l)}\vec{M}_{e1n}^{(1)} + ic_n^{(l)}\vec{N}_{o1n}^{(1)} - ib_n^{(l)}\vec{N}_{o1n}^{(3)} - a_n^{(l)}\vec{M}_{e1n}^{(3)}\right] \tag{C.6}$$

with $k_l = N_l\omega/c$. Since the Hankel function diverges at the origin, $a_n^{(1)} = b_n^{(1)} = 0$. Moreover, from Eq. (C.3) and Eq. (C.4), $c_n^{(L+1)} = d_n(L+1) = 1$, $a_n^{(L+1)} = a_n$, and $b_n^{(L+1)} = b_n$.

Using the orthogonality of the vector spherical harmonics, the standard Maxwell boundary conditions yield

$$\begin{aligned} 0 &= d_n^{(l)} m_{l-1} \psi_n'(m_l x_{l-1}) - a_n^{(l)} m_{l-1} \zeta_n'(m_l x_{l-1}) \\ &\quad - d_n^{(l-1)} m_l \psi_n'(m_{l-1} x_{l-1}) + a_n^{(l-1)} m_l \zeta_n'(m_{l-1} x_{l-1}) \qquad \text{(C.7)} \\ 0 &= c_n^{(l)} m_{l-1} \psi_n(m_l x_{l-1}) - b_n^{(l)} m_{l-1} \zeta_n(m_l x_{l-1}) \\ &\quad - c_n^{(l-1)} m_l \psi_n(m_{l-1} x_{l-1}) + b_n^{(l-1)} m_l \zeta_n(m_{l-1} x_{l-1}) \qquad \text{(C.8)} \\ 0 &= c_n^{(l)} \psi_n'(m_l x_{l-1}) - b_n^{(l)} \zeta_n'(m_l x_{l-1}) \\ &\quad - c_n^{(l-1)} \psi_n'(m_{l-1} x_{l-1}) + b_n^{(l-1)} \zeta_n'(m_{l-1} x_{l-1}) \qquad \text{(C.9)} \\ 0 &= d_n^{(l)} \psi_n(m_l x_{l-1}) - a_n^{(l)} \zeta_n(m_l x_{l-1}) \\ &\quad - d_n^{(l-1)} \psi_n(m_{l-1} x_{l-1}) + a_n^{(l-1)} \zeta_n(m_{l-1} x_{l-1}), \qquad \text{(C.10)} \end{aligned}$$

where ψ_n is the Riccati-Bessel function, ζ_n is the Riccati-Hankel function of the first kind, $m_l = N_l/N$, and $x_l = N\omega r_l/c$. The primes denote differentiation with respect to the argument. Let

$$\begin{aligned} \bar{A}_n^{(l)} &\equiv \frac{\zeta_n(m_l x_l)}{\psi_n(m_l x_l)} \frac{a_n^{(l)}}{d_n^{(l)}} \qquad \text{(C.11)} \\ \bar{B}_n^{(l)} &\equiv \frac{\zeta_n(m_l x_l)}{\psi_n(m_l x_l)} \frac{b_n^{(l)}}{c_n^{(l)}} \qquad \text{(C.12)} \end{aligned}$$

Then, by rearranging the terms in Eq. (C.7) through Eq. (C.10), we obtain recursive

relations for $\bar{A}_n^{(l)}$ and $\bar{B}_n^{(l)}$:

$$\begin{aligned}
\bar{A}_n^{(l)} &= \frac{\psi_n(m_l x_{l-1})}{\psi_n(m_l x_l)} \frac{\zeta_n(m_l x_l)}{\zeta_n(m_l x_{l-1})} \\
&\times \frac{\bar{A}_n^{(l-1)} \left[\frac{m_l}{m_{l-1}} F_n(m_{l-1}x_{l-1}) - D_n(m_l x_{l-1})\right] - \left[\frac{m_l}{m_{l-1}} D_n(m_{l-1}x_{l-1}) - D_n(m_l x_{l-1})\right]}{\bar{A}_n^{(l-1)} \left[\frac{m_l}{m_{l-1}} F_n(m_{l-1}x_{l-1}) - F_n(m_l x_{l-1})\right] - \left[\frac{m_l}{m_{l-1}} D_n(m_{l-1}x_{l-1}) - F_n(m_l x_{l-1})\right]} \\
\bar{B}_n^{(l)} &= \frac{\psi_n(m_l x_{l-1})}{\psi_n(m_l x_l)} \frac{\zeta_n(m_l x_l)}{\zeta_n(m_l x_{l-1})} \\
&\times \frac{\bar{B}_n^{(l-1)} \left[\frac{m_l}{m_{l-1}} D_n(m_l x_{l-1}) - F_n(m_{l-1}x_{l-1})\right] - \left[\frac{m_l}{m_{l-1}} D_n(m_l x_{l-1}) - D_n(m_{l-1}x_{l-1})\right]}{\bar{B}_n^{(l-1)} \left[\frac{m_l}{m_{l-1}} F_n(m_l x_{l-1}) - F_n(m_{l-1}x_{l-1})\right] - \left[\frac{m_l}{m_{l-1}} F_n(m_l x_{l-1}) - D_n(m_{l-1}x_{l-1})\right]}
\end{aligned}$$

for $l = 2, \ldots L$, and

$$\begin{aligned}
a_n &= \frac{\psi_n(x_L)}{\zeta_n(x_L)} \frac{\bar{A}_n^{(L)} \left[\frac{1}{m_L} F_n(m_L x_L) - D_n(x_L)\right] - \left[\frac{1}{m_L} D_n(m_L x_L) - D_n(x_L)\right]}{\bar{A}_n^{(L)} \left[\frac{1}{m_L} F_n(m_L x_L) - F_n(x_L)\right] - \left[\frac{1}{m_L} D_n(m_L x_L) - F_n(x_L)\right]} \\
b_n &= \frac{\psi_n(x_L)}{\zeta_n(x_L)} \frac{\bar{B}_n^{(L)} \left[\frac{1}{m_L} D_n(x_L) - F_n(m_L x_L)\right] - \left[\frac{1}{m_L} D_n(x_L) - D_n(m_L x_L)\right]}{\bar{B}_n^{(L)} \left[\frac{1}{m_L} F_n(x_L) - F_n(m_L x_L)\right] - \left[\frac{1}{m_L} F_n(x_L) - D_n(m_L x_L)\right]}
\end{aligned}$$

with $\bar{A}_n^{(1)} = 0$ and $\bar{B}_n^{(1)} = 0$ as initial conditions. Here, we have used

$$D_n(z) \equiv \frac{\psi_n'(z)}{\psi_n(z)} \tag{C.13}$$

$$F_n(z) \equiv \frac{\zeta_n'(z)}{\zeta_n(z)}. \tag{C.14}$$

To render the recursive algorithm more suitable for computer programming, we define new variables,

$$\begin{aligned}
A_n^{\star(l)} &\equiv \frac{\psi_n(m_l x_l)}{\psi_n(m_l x_{l-1})} \frac{\zeta_n(m_l x_{l-1})}{\psi_n(m_l x_l)} \bar{A}_n^{(l)} \\
B_n^{\star(l)} &\equiv \frac{\psi_n(m_l x_l)}{\psi_n(m_l x_{l-1})} \frac{\zeta_n(m_l x_{l-1})}{\psi_n(m_l x_l)} \bar{B}_n^{(l)},
\end{aligned}$$

and bring the recursion relations to a form similar to that of T. Kaiser and G.

Schweiger[105]:

$$A_n^{\star(l)} = \frac{D_n(m_l x_{l-1}) - \frac{m_l}{m_{l-1}} \tilde{D}_n^{(l-1)}}{F_n(m_l x_{l-1}) - \frac{m_l}{m_{l-1}} \tilde{D}_n^{(l-1)}} \tag{C.15}$$

$$B_n^{\star(l)} = \frac{\frac{m_l}{m_{l-1}} D_n(m_l x_{l-1}) - \tilde{G}_n^{(l-1)}}{\frac{m_l}{m_{l-1}} F_n(m_l x_{l-1}) - \tilde{G}_n^{(l-1)}} \tag{C.16}$$

for $l = 2, \cdots L$, and

$$a_n = \frac{\left(\frac{\tilde{D}_n^{(L)}}{m_L} + \frac{n}{x_L}\right) \psi_n(x_L) - \psi_{n-1}(x_L)}{\left(\frac{\tilde{D}_n^{(L)}}{m_L} + \frac{n}{x_L}\right) \zeta_n(x_L) - \zeta_{n-1}(x_L)} \tag{C.17}$$

$$b_n = \frac{\left(m_L \tilde{G}_n^{(L)} + \frac{n}{x_L}\right) \psi_n(x_L) - \psi_{n-1}(x_L)}{\left(m_L \tilde{G}_n^{(L)} + \frac{n}{x_L}\right) \zeta_n(x_L) - \zeta_{n-1}(x_L)} \tag{C.18}$$

with

$$A_n^{\star(1)} = 0 \tag{C.19}$$

$$B_n^{\star(1)} = 0 \tag{C.20}$$

as initial conditions, where

$$\tilde{D}_n^{(l)} \equiv \frac{D_n(m_l x_l) - \frac{\psi_n(m_l x_{l-1})}{\psi_n(m_l x_l)} \frac{\zeta_n(m_l x_l)}{\zeta_n(m_l x_{l-1})} F_n(m_l x_l) A_n^{\star(l)}}{1 - \frac{\psi_n(m_l x_{l-1})}{\psi_n(m_l x_l)} \frac{\zeta_n(m_l x_l)}{\zeta_n(m_l x_{l-1})} A_n^{\star(l)}} \tag{C.21}$$

$$\tilde{G}_n^{(l)} \equiv \frac{D_n(m_l x_l) - \frac{\psi_n(m_l x_{l-1})}{\psi_n(m_l x_l)} \frac{\zeta_n(m_l x_l)}{\zeta_n(m_l x_{l-1})} F_n(m_l x_l) B_n^{\star(l)}}{1 - \frac{\psi_n(m_l x_{l-1})}{\psi_n(m_l x_l)} \frac{\zeta_n(m_l x_l)}{\zeta_n(m_l x_{l-1})} B_n^{\star(l)}}. \tag{C.22}$$

Note that these equations are expressed in terms of the Riccati-Bessel and Riccati-Hankel functions with a real argument ($\psi_n(x_L)$ and $\zeta_n(x_L)$), the logarithmic derivatives ($D_n(z)$ and $F_n(z)$), and the ratios of the functions ($\psi_n(z_1)/\psi_n(z_2)$ and $\zeta_n(z_1)/\zeta_n(z_2)$), all of which can be calculated reliably, without numerical instability, using known upward or downward recursions[104, 108]. The computer program for

the recursive algorithm was written by C. Rohde using C/C++, and the details of the code can be found in his Ph.D. dissertation[95].

BIBLIOGRAPHY

[1] W. H. Brattain, "Surface Properties of Semiconductors," http://nobelprize.org/.

[2] H. Raether, *Surface Plasmons on Smooth and Rough Surfaces and on Gratings* (Springer-Verlag, Berlin, 1988).

[3] R. Jin, Y. W. Cao, C. A. Mirkin, K. L. Kelly, G. C. Schatz, and J. G. Zheng, Science **294**, 1901 (2001).

[4] J. J. Mock, M. Barbic, D. R. Smith, D. A. Schultz, and S. Schultz, J. Chem. Phys. **116**, 6755 (2002).

[5] H. Kuwata, H. Tamaru, K. Esumi, and K. Miyano, Appl. Phys. Lett. **83**, 4625 (2003).

[6] S. J. Oldenburg, R. D. Averitt, S. L. Westcott, and N. J. Halas, Chem. Phys. Lett. **228**, 243 (1998).

[7] E. Prodan and P. Nordlander, Nano Lett. **3**, 543 (2003).

[8] E. Prodan, C. Radloff, N. Halas, and P. Nordlander, Science **302**, 419 (2003).

[9] K. Hasegawa, C. Rohde, and M. Deutsch, Opt. Lett. **31**, 1136 (2006).

[10] C. Rohde, K. Hasegawa, and M. Deutsch, Opt. Lett. **32**, 415 (2007).

[11] M. L. Brongersma and P. G. Kik, *Surface Plasmon Nanophotonics* (Springer, Dordrecht, 2007).

[12] D. Sarid, Phys. Rev. Lett. **47**, 1927 (1981).

[13] J. C. Weeber, M. U. González, A. L. Baudrion, and A. Dereux, Appl. Phys. Lett. **87**, 221101 (2005).

[14] B. Steinberger, A. Hohenau, H. Ditlbacher, A. L. Stepanov, A. Drezet, F. R. Aussenegg, A. Leitner, and J. R. Krenn, Appl. Phys. Lett. **88**, 094104 (2006).

[15] K. Tanaka and M. Tanaka, Appl. Phys. Lett. **82**, 1158 (2003).

[16] R. Zia, M. D. Selker, P. B. Catrysse, and M. L. Brongersma, J. Opt. Soc. Am. A **21**, 2442 (2004).

[17] A. W. Sanders, D. A. Routenberg, B. J. Wiley, Y. Xia, E. R. Dufresne, and M. A. Reed, Nano Lett. **6**, 1822 (2006).

[18] S. I. Bozhevolnyi, J. Erland, K. Leosson, P. M. W. Skovgaard, and J. M. Hvam, Phys. Rev. Lett. **86**, 3008 (2001).

[19] S. I. Bozhevolnyi, V. S. Volkov, K. Leosson, and A. Boltasseva, Appl. Phys. Lett. **79**, 1076 (2001).

[20] S. A. Maier, P. G. Kik, and H. A. Atwater, Appl. Phys. Lett. **81**, 1714 (2002).

[21] S. A. Maier, P. G. Kik, H. A. Atwater, S. Meltzer, E. Harel, B. E. Koel, and A. A. G. Requicha, Nat. Mater. **2**, 229 (2003).

[22] T. Yatsui, M. Kourogi, and M. Ohtsu, Appl. Phys. Lett. **79**, 4583 (2001).

[23] S. I. Bozhevolnyi and F. A. Pudonin, Phys. Rev. Lett. **78**, 2823 (1977).

[24] J. R. Krenn, H. Ditlbacher, G. Schider, A. Hohenau, A. Leitner, and F. R. Aussenegg, J. Microsc. **209**, 167 (2003).

[25] H. Ditlbacher, J. R. Krenn, G. Schider, A. Leitner, and F. R. Aussenegg, Appl. Phys. Lett. **81**, 1762 (2002).

[26] V. Coello, T. Søndergaard, and S. I. Bozhevolnyi, Opt. Commun. **240**, 345 (2004).

[27] S. I. Bozhevolnyi, V. S. Volkov, E. Devaux, J.-Y. Laluet, and T. W. Ebbesen, Nature **440**, 508 (2006).

[28] T. Nikolajsen, K. Leosson, and S. I. Bozhevolnyi, Appl. Phys. Lett. **85**, 5833 (2004).

[29] G. A. Plotz, H. J. Simon, and J. M. Tucciarone, J. Opt. Soc. Am. **69**, 419 (1979).

[30] D. J. Bergman and M. I. Stockman, Phys. Rev. Lett. **90**, 027402 (2003).

[31] M. P. Nezhad, K. Tetz, and Y. Fainman, Opt. Express **12**, 4072 (2004).

[32] J. Seidel, S. Grafström, and L. Eng, Phys. Rev. Lett. **94**, 177401 (2005).

[33] S. A. Maier, Opt. Commun. **258**, 295 (2006).

[34] J. Homola, S. S. Yee, and G. Gauglitz, Sens. Actuators B **54**, 3 (1999).

[35] S. Lal, S. Link, and N. J. Halas, Nat. Photonics **1**, 641 (2007).

[36] R. Karlsson and R. Ståhleberg, Anal. Biochem. **228**, 274 (1995).

[37] N. Nath and A. Chilkoti, Anal. Chem. **74**, 504 (2002).

[38] N. Nath and A. Chilkoti, Anal. Chem. **76**, 5370 (2004).

[39] A. J. Haes and R. P. V. Duyne, J. Am. Chem. Soc. **124**, 10596 (2002).

[40] A. J. Haes and R. P. V. Duyne, Anal. Bioanal. Chem. **379**, 920 (2004).

[41] R. C. Mucic, J. J. Storhoff, C. A. Mirkin, and R. L. Letsinger, J. Am. Chem. Soc. **120**, 12674 (1998).

[42] L. R. Hirsch, J. B. Jackson, A. Lee, N. J. Halas, and J. L. West, Anal. Chem. **75**, 2377 (2003).

[43] J. Jackson, S. Westcott, L. Hirsch, J. West, and N. Halas, Appl. Phys. Lett. **82**, 257 (2003).

[44] L. R. Hirsch, R. J. Stafford, J. A. Bankson, S. R. Sershen, B. Rivera, R. E. Price, J. D. Hazle, N. J. Halas, and J. L. West, Proc. Natl. Acad. Sci. USA **100**, 13549 (2003).

[45] C. Loo, A. Lin, L. Hirsch, M. H. Lee, J. Barton, N. Halas, J. West, and R. Drezek, Technol. Cancer Res. T. **3**, 33 (2004).

[46] V. G. Veselago, Sov. Phys. Usp. **10**, 509 (1968).

[47] J. B. Pendry, Phys. Rev. Lett. **85**, 3966 (2000).

[48] J. B. Pendry, Contemp. Phys. **45**, 191 (2004).

[49] R. A. Shelby, D. R. Smith, and S. Schultz, Science **292**, 77 (2001).

[50] V. M. Shalaev, W. Cai, U. K. Chettiar, H. K. Yuan, A. K. Sarychev, V. P. Drachev, and A. V. Kildishev, Opt. Lett. **30**, 3356 (2005).

[51] J. Zhou, T. Koschny, L. Zhang, G. Tuttle, and C. M. Soukoulis, Appl. Phys. Lett. **88**, 221103 (2006).

[52] A. N. Grigorenko, A. K. Geim, H. F. Gleeson, Y. Zhang, A. A. Firsov, I. Y. Khrushchev, and J. Petrovic, Nature **2005**, 335 (2005).

[53] G. Dolling, C. Enkrich, M. Wegener, J. F. Zhou, C. M. Soukoulis, and S. Linden, Opt. Lett. **30**, 3198 (2005).

[54] U. Leonhardt, Science **312**, 1777 (2006).

[55] J. B. Pendry, D. Schurig, and D. R. Smith, Science **312**, 1780 (2006).

[56] M. G. Silveirinha, A. Alù, and N. Engheta, Science **75**, 036603 (2007).

[57] W. Cai, U. K. Chettiar, A. V. Kildishev, and V. M. Shalaev, Nat. Photonics **1**, 224 (2007).

[58] K. Hasegawa, J. U. Nöckel, and M. Deutsch, Appl. Phys. Lett. **84**, 1835 (2004).

[59] K. Hasegawa, J. U. Nöckel, and M. Deutsch, Phys. Rev. A **75**, 063816 (2007).

[60] A. Chen, M. Deutsch, V. A. Podolskiy, and M. Deutsch, Opt. Lett. **32**, 1770 (2007).

[61] C. Rohde, K. Hasegawa, and M. Deutsch, Phys. Rev. Lett. **96**, 045503 (2006).

[62] D. Monroe, Phys. Rev. Focus **21**, story 5 (2008).

[63] T. I. Jeon and D. Grischkowsky, Appl. Phys. Lett. **88**, 061113 (2006).

[64] A. Degiron and D. R. Smith, Opt. Express **14**, 1611 (2006).

[65] P. Berini and J. Lu, Opt. Express **14**, 2365 (2006).

[66] I. P. Radko, T. Søndergaard, and S. I. Bozhevolnyi, Opt. Express **14**, 4107 (2006).

[67] G. Veronis and S. Fan, Appl. Phys. Lett. **87**, 131102 (2005).

[68] W. K. Kim, W. S. Yang, H. M. . Lee, H. Y. Lee, M. H. Lee, and W. J. Jung, Opt. Express **14**, 13043 (2006).

[69] A. Mekis, J. C. Chen, I. Kurland, S. Fan, P. R. Villeneuve, and J. D. Joannopoulos, Phys. Rev. Lett. **77**, 3787 (1996).

[70] F. Sols and M. Macucci, Phys. Rev. B **41**, 11887 (1990).

[71] J. B. Keller, J. Opt. Soc. Am. **52**, 116 (1962).

[72] H. A. Jamid and S. J. Al-Bader, IEEE Photon. Technol. Lett. **7**, 321 (1995).

[73] E. D. Palik, *Handbook of Optical Constants of Solids* (Academic Press, Orlando, 1985).

[74] G. X. Fan and Q. H. Liu, IEEE Trans. Antennas Propagat. **48**, 637 (2000).

[75] U. Schröter, S. Seider, S. Tode, and D. Heitmann, Ultramicroscopy **68**, 223 (1997).

[76] A. Yariv, Electron. Lett. **36**, 321 (2000).

[77] S. Fan, P. R. Villeneuve, J. D. Joannopoulos, M. J. Khan, C. Manolatou, and H. A. Haus, Phys. Rev. B **59**, 15882 (1999).

[78] Y. Xu, Y. Li, R. K. Lee, and A. Yariv, Phys. Rev. E **62**, 7389 (2000).

[79] J. C. M. Garnett, Philos. Trans. R. Soc. London **203**, 385 (1904).

[80] D. A. G. Bruggeman, Ann. Phys. (Leipzig) **24**, 636 (1935).

[81] R. W. Cohen, G. D. Cody, M. D. Coutts, and B. Abeles, Phys. Rev. B **8**, 3689 (1973).

[82] Y. Kantor and D. J. Bergman, J. Phys. C **15**, 2033 (1982).

[83] M. M. Wind, P. A. Bobbert, J. Vlieger, and D. Bedeaux, Physica A **157**, 269 (1989).

[84] Y. Yagil, P. Dadenne, C. Julien, and G. Deutscher, Phys. Rev. B **46**, 2503 (1992).

[85] M. M. Dvoynenko, A. V. Goncharenko, V. R. Romaniuk, and E. F. Venger, Physica B **299**, 88 (2001).

[86] P. G. Kard, Opt. Spectrosc. **10**, 193 (1963).

[87] R. J. Potton, Rep. Prog. Phys. **67**, 717 (2004).

[88] M. S. M. Emmons, J. Bouwman, A. Chen, and M. Deutsch, J. Colloid Interface Sci. **306**, 41 (2007).

[89] E. Altewischer, M. P. van Exter, and J. P. Woerdman, Opt. Lett. **28**, 1906 (2003).

[90] M. Sarrazin and J. P. Vigneron, Phys. Rev. B **70**, 193409 (2004).

[91] Y. V. Troitskiĭ, Opt. Spectrosc. **98**, 125 (2005).

[92] S. M. Peterson, Ph.D. dissertation (University of Oregon, 2007).

[93] L. J. van der Pauw, Philips Res. Rep. **13**, 1 (1958).

[94] P. Beckmann and A. Spizzochino, *The Scattering of Electromagnetic Waves from Rough Surfaces* (Pergamon, New York, 1963).

[95] C. Rohde, Ph.D. dissertation (University of Oregon, 2008).

[96] J. H. Lambert, *Photometria sive de mensura de gratibus luminis, colorum et umbrae* (Eberhard Klett, Augsberg, 1760).

[97] S. K. Nayar, K. Ikeuchi, and T. Kanade, IEEE Trans. Pattern Anal. Mach. Intell. **13**, 611 (1991).

[98] K. Torrance and E. Sparrow, J. Opt. Soc. Am. **57**, 1105 (1967).

[99] R. Ruppin, *Electromagnetic Surface Modes* (Wiley, New York, 1982).

[100] H. Shin, M. F. Yanik, S. Fan, R. Zia, and M. L. Brongersma, Appl. Phys. Lett. **82**, 4421 (2004).

[101] P. Gadenne, F. Brouers, V. Shalaev, and A. Sarychev, J. Opt. Soc. Am. B **15**, 68 (1998).

[102] E. Merzbacher, *Quantum Mechanics* (Wiley, New York, 1998).

[103] K. Velikov, G. Zegers, and A. van Blaaderen, Langmuir **19**, 1384 (2003).

[104] O. B. Toon and T. P. Ackerman, Appl. Opt. **20**, 3657 (1981).

[105] T. Kaiser and G. Schweiger, Comput. Phys. **7**, 682 (1993).

[106] W. Yang, Appl. Opt. **42**, 1710 (2003).

[107] H. Du, Appl. Opt. **43**, 1953 (2004).

[108] V. E. Cachorro and L. L. Salcedo, "New improvements for Mie scattering calculations," arXiv:physics/0103052v1, http://arxiv.org.

[109] Z. Jakšić, M. Maksimović, and M. Sarajilić, J. Opt. A: Pure Appl. Opt. **7**, 51 (2005).

[110] C. Rohde, K. Hasegawa, A. Chen, and M. Deutsch, Mater. Res. Soc. Symp. Proc. **846**, 364 (2005).

[111] S. Grésillon, L. Aigouy, A. C. Boccara, J. C. Rivoal, X. Quelin, C. Desmarest, P. Gadenne, V. A. Shubin, A. K. Sarychev, and V. M. Shalaev, Phys. Rev. Lett. **82**, 4520 (1999).

[112] S. Ducourtieux, V. A. Podolskiy, S. Grésillon, S. Buil, B. Berini, P. Gadenne, A. C. Boccara, J. C. Rivoal, W. A. Bragg, K. Banerjee, et al., Phys. Rev. B **64**, 165403 (2001).

[113] Y. Yagil, M. Yosefin, D. J. Bergman, G. Deutscher, and P. Gadenne, Phys. Rev. B **43**, 11342 (1991).

[114] V. M. Shalaev, *Nonlinear Optics of Random Media* (Springer, Berlin, 2000).

[115] B. J. Last and D. J. Thouless, Phys. Rev. Lett. **27**, 1717 (1971).

[116] B. P. Watson and P. L. Leath, Phys. Rev. B **9**, 4893 (1974).

[117] B. Abeles, H. L. Pinch, and J. I. Gittleman, Phys. Rev. Lett. **35**, 247 (1975).

[118] J. P. Straley, J. Phys. C **9**, 783 (1976).

[119] U. Kreibig and M. Vollmer, *Optical Properties of Metal Clusters* (Springer, Berlin, 1995).

[120] K. S. Yee, IEEE Trans. Antennas Propagat. **14**, 302 (1966).

[121] A. Taflove and S. C. Hagness, *Computational Electrodynamics: The Finite-Difference Time-Domain Method* (Artech House, Norwood, MA, 2005).

[122] D. F. Kelley and R. J. Luebbers, IEEE Trans. Antennas Propagat. **44**, 792 (1990).

[123] D. M. Sullivan, IEEE Trans. Antennas Propagat. **40**, 1223 (1992).

[124] T. Kashiwa and I. Fukai, Microwave Opt. Tech. Lett. **3**, 203 (1990).

[125] G. Mur, IEEE Trans. Electromagn. Compat. **23**, 377 (1981).

[126] J. P. Berenger, J. Comput. Phys. **114**, 185 (1994).

[127] Q. H. Liu, Microwave Opt. Tech. Lett. **14**, 134 (1997).

[128] G. Mie, Ann. Phys. **25**, 377 (1908).

[129] A. L. Aden and M. Kerker, J. Appl. Phys. **22**, 1242 (1951).

[130] R. Bhandari, Appl. Opt. **24**, 1960 (1985).

[131] W. Liang, Y. Xu, Y. Huang, A. Yariv, J. G. Fleming, and S. Y. Lin, Opt. Express **12**, 657 (2004).

[132] C. F. Bohren and D. R. Huffman, *Absorption and Scattering of Light by Small Particles* (Wiley, New York, 1983).